CHARACTERIZATION OF LARGE LPG POOL FIRES AND MUCUS CLEARANCE DYNAMICS IN UPPER AIRWAY USING CFD METHOD

By

HANG YI

Bachelor of Engineering in Safety Engineering
Northeastern University
Shenyang, China
2013

Master of Science in Safety Science and Engineering
Northeastern University
Shenyang, China
2015

Submitted to the Faculty of the
Graduate College of the
Oklahoma State University
in partial fulfillment of
the requirements for
the Degree of
DOCTOR OF PHILOSOPHY
December, 2020

CHARACTERIZATION OF LARGE LPG POOL FIRES AND MUCUS CLEARANCE DYNAMICS IN UPPER AIRWAY USING CFD METHOD

Dissertation Approved:

Dr.Yu Feng

Dissertation Advisor

Dr. Ashlee N. Ford Versypt

Dr. Seok-Jhin Kim

Dr. Haejun Park

Dr. Qingsheng Wang

ACKNOWLEDGEMENTS

First and foremost, I would like to express my sincere gratitude to my advisor and the committee chair, Dr. Yu Feng, who inspired me to pursue my Ph.D. and continuously encouraged me to push myself further than I ever thought possible. His guidance, assistance, thoughts, encouragement and attitude to scientific research have become the priceless source to inspire me throughout the study and will last forever in my lifetime. Thanks very much Dr. Feng not only for the instructions for the research work, but also sharing the experience and perspectives for daily life. I also would like to appreciate the guidance and assistance to committee members, Dr. Ashlee Ford Versypt, Dr. Haejun Park, Dr. Seok-Jhin Kim, and Dr. Qingsheng Wang. Thanks also go to all the members in Computational Biofluidics and Biomechanics Laboratory (CBBL), especially Jianan Zhao, Hamideh Hayati, Ted Sperry, Ahmad Haghnegahdar, and Max Kozak.

I would like again to thank my previous advisor, Dr. Wang, from the early period of Ph.D. program application, to the day to day instructions and discussions during the Ph.D. program. Also, thanks to all the members in Dr. Wang's group, including but not limited to Dr. Beibei Wang, Dr. Denglong Ma, Dr. Kang Cen, Dr. Yantong Wang, Dr. Xuepeng Jiang, Dr. Kaiwu Liang, Dr. Yanying Xu, Dr. Lulu Zhou, Dr. Hongpu Mi, Ruiqing Shen, Qingtong Liu, Xi Chen, and Shiyun Wu.

I feel indebted to Dr. Jingxian Liu in Northeastern University (CN), who was the advisor of my M.S. program, and encouraged me to work hard and study in deep continuously since he was the instructor of a B.S. program course in 2011.

I truly appreciated to the Director of Graduate Program in Chemical Engineering, Dr. Heather Fahlenkamp, Graduate Program Assistant, Beth Kelly, and Manager of Chinese Development, Dr. Vivian Wang, with their support and information to help me to catch up with the degree milestone.

I would like to thank the staffs at the High Performance Computing Center (HPCC), Jesse Schafer and Evan Linde, who provided me the assistance for the computing source using.

The last but not the least, I am eternally and indescribably grateful to my parents, my elder brother and my sister in law who have all stood behind me as my motivation, comfort, and cheerleading squad around the clock in the past 4 years. I love you to the moon and back.

Name: HANG YI

Date of Degree: DECEMBER, 2020

Title of Study: CHARACTERIZATION OF LARGE LPG POOL FIRES AND MUCUS CLEARANCE DYNAMICS IN UPPER AIRWAY USING CFD METHOD

Major Field: CHEMICAL ENGINEERING

Abstract: A large pool fire can be generated if there is a liquefied petroleum gas (LPG) leakage during transportation or at storage sites, while the underlying mechanisms of how the hazardous matter can be generated from the LPG pool fire and delivered dose into the human lung, and evaluation of the exposure risks are still ambiguous. Thus, it is necessary to systematically study the LPG pool fire rheology and the generation, transport, and deposition of the generated aerosolized toxicants from the pool fire to the human respiratory system. To partially address the above-mentioned concerns, this study has conducted novel research efforts to investigate the characteristics of large LPG pool fires and cough-driven mucus transport behaviors in upper lung airways, which can be employed to assess the health risks from LPG fires to the pulmonary system future work. Specifically, Chapter I reviewed the previous studies concerning the LPG pool fires and mucus movement behaviors in lung airways using experimental methods and numerical approaches, as well as presented the research objectives. Chapter II was to develop an experimentally validated CFD model to estimate the surface emissive power, and predict the incident radiation from large LPG pool fires to the surrounded objects and develop the reasonable minimum distances between the pool fire and objects using CFD simulations. Chapter III performed numerical simulations using an experimentally validated CFD model to simulate large LPG pool fires and predict the fire configuration characteristics, including flame height and flame tilt. The impacts of pool diameter and wind velocity on the fire configuration characteristics were investigated. Based on the CFD results and the parametric analysis, new correlations are proposed to provide more accurate estimations of flame height and tilt specifically for large LPG pool fires. Chapter IV has built an experimentally validated Volume of Fluid (VOF) model to conduct a quantitative analysis to investigate the effects of cough intensity and initial mucus thicknesses on the mucus transport and clearance in a mouth-to-trachea airway geometry. The VOF model developed in this work can be further refined and integrated with Discrete Phase Models (DPMs) to predict the mucus clearance effect on inhaled toxic particles from LPG pool fires explicitly. In addition, Chapter V summarized the essentials of the research work done and outlined the future work.

TABLE OF CONTENTS

Chapter Page

I. INTRODUCTION 1

1.1 Research Motivation 1
1.2 Literature Review 4
1.2.1 Heat Radiation from Large LPG Pool Fires 4
1.2.2 Configuration of Large LPG Pool Fires Using CFD Method 6
1.2.3 Mucus Rheology in Upper Lung Airways 6
1.3 Research Objectives and Novel Contributions 8
1.3.1 Research Objectives 8
1.3.2 Novel Contributions 8

II. PREDICTIONS OF HEAT RADIATION FROM LARGE LIQUEFIED PETROLEUM GAS POOL FIRES 10

2.1 Introduction 10
2.2 Research Objectives 13
2.3 Theory 13
2.3.1 Governing Equations 13
2.3.2 Surface Emissive Power (SEP) 16
2.3.3 Radiative Heat Flux 18
2.4 Numerical Method 21
2.4.1 Geometry and Mesh 21
2.4.2 Numerical Setup 23
2.5 Results and Discussion 24
2.5.1 Prediction of Surface Emissive Power (SEP) 24
2.5.2 Radiative Heat Flux 27
2.5.3 Safe Separation Distance 34
2.6 Summary 38

III. CONFIGURATION PREDICTIONS OF LARGE LIQUEFIED PETROLEUM GAS POOL FIRES USING A CFD METHOD 39

Chapter Page
3.1 Introduction....39
3.2 Research Objectives....41
3.3 Theory....41
3.3.1 Burning Rate Models....42
3.3.2 Flame Height Models....42
3.3.3 Flame Tilt Models....47
3.2.4 Governing Equations....49
3.4 Numerical Method....50
3.4.1 Geometry and Mesh....50
3.4.2 Numerical Setup....51
3.5 Results and Discussion....53
3.5.1 Comparisons of Predicted Flame Heights to Find the Best Burning Rate Model....53
3.5.2 Flame Height vs. Pool Diameter and Wind Velocity....55
3.5.3 Flame Tilt Angle vs. Pool Diameter and Wind Velocity....62
3.6 Summary....66

IV. LUNG DISEASE EFFECT ON THE COUGH-DRIVEN MUCUS MOVEMENT AND CLEARANCE IN AN IDEALIZED UPPER AIRWAY MODEL USING VOF....68

4.1 Introduction....68
4.2 Research Objectives....71
4.3 Theory....71
4.3.1 Governing Equations....73
4.3.2 Mucus Clearance Efficiency....75
4.4 Numerical Method....75
4.4.1 Geometry and Mesh....75
4.4.2 Boundary and Initial Conditions....78
4.4.3 Numerical Setup....78
4.5 Results and Discussion....79
4.5.1 VOF Model Validation....79
4.5.2 Newtonian vs. Non-Newtonian Mucus Viscosity Models....82
4.5.3 Effects of Mucus Thickness....95
4.5.4 Effects of Cough Strength....100
4.5.5 Mucus Rheology Driven by Transient Expiratory Airflows....101
4.6 Summary....102
4.7 Limitation of Current Study and Future Work....103

V. CONCLUSIONS AND FUTURE WORK....104

5.1 Conclusions....104
5.1.1 Heat Radiation from Large Liquefied Petroleum Gas Pool Fires....104

Chapter Page

5.1.2 Configurations of Large Liquefied Petroleum Gas Pool Fires 105
5.1.3 Lung Disease Effect on the Cough-Driven Mucus Movement and Clearance in an Idealized Upper Airway Model.....106
5.2 Novel Contributions.....106
5.3 Future Directions 107
5.3.1 Predict the Distributions of Generated Toxic Gases and Heat Flux by an LPG Pool Fire in an Indoor Environment.....109
5.3.2 Predictions of the Transport and Deposition of Toxic Gases, as well as the Heat Transfer in a Representative Human Respiratory System.....109

REFERENCES 110

APPENDICES 136

APPENDIX A: Overview of Numerical Models.....136
APPENDIX B: Mesh Independence Test for the 3D Straight Tube.....146
APPENDIX C: In-house UDFs for Cough Waveforms 149

LIST OF TABLES

Table Page

2.1 Thermal exposure criteria in standards and regulations 11

2.2 Boundary conditions of the CFD simulation for large LPG pool fires.....23

2.3 Safe separation distances between large LPG pool fires and targets estimated using CFD simulations. 37

3.1 Boundary conditions employed in CFD simulations for large LPG pool fires...52

3.2. Flame heights (m) for pool fires with different pool diameters (m) and wind velocities (m/s).....58

3.3. Flame tilt angles for pool fires with different pool diameters (m) and wind velocities (m/s).....62

4.1 Mesh details in the mesh independence tests for air-driven mucus clearance simulations using the VOF model. 78

4.2 Average volumetric flow rate $\bar{q}_m$(ml/s) in the selected time stations in a single cough.....93

4.3 Mucus clearance efficiency (%) at selected time stations during a single cough93

4.4 Average mucus velocityv_m(m/s) at each across planes C-C' and D-D' in selected time stations. 94

4.5 Mucus clearance efficiency (%) in non-Newtonian fluid simulations at Z-1 during a single cough 100

B. 1 Details of the meshes generated for the mesh independence test of the straight tube.....148

LIST OF FIGURES

Figure Page

1.1 The overall workflow of specific aims 4

2.1 Point source model (PSM) and solid flame model (SFM) to calculate incident radiation from LPG pool fires: (a) point source model; (b) solid flame model (regular cylindrical flame); (c) solid flame model (inclined cylindrical flame).....20

2.2 LPG pool fire geometry and the structured hexahedral mesh (D = 16.9 m).....22

2.3 Comparisons of VR in different meshes for mesh independence test. 22

2.4 Temperature (K) profiles of large LPG pool fires in different sizes and atmosphere conditions: (a) D = 12.9 m, u_W = 3 m/s, (b) D = 14.9 m, u_W = 2.5 m/s, (c) D = 16.9 m, u_W = 0. 25

2.5 Comparison of surface emissive power (kW/m^2) obtained by empirical models, proposed equation, and experiments for large LPG pool fires. 26

2.6 Incident radiation distributions at Y=0 of large LPG pool fires with different sizes and wind speeds: (a) D = 12.9 m, u_W = 3 m/s, (b) D = 14.9 m, u_W = 2.5 m/s, (c) D = 16.9 m, u_W = 0.....29

2.7 Iso-surfaces of incident radiation (kW/m^2) at different RIS in LPG pool fire (D =12.9 m): (a) R_{IS} = 20 m, (b) R_{IS} = 40 m, (c) R_{IS} = 55 m, (d) R_{IS} = 60 m, (e) R_{IS} = 80 m30

2.8 Iso-surfaces of incident radiation (kW/m^2) at different RIS for LPG pool fire (D =14.9 m): (a) R_{IS} = 20 m, (b) R_{IS} = 40 m, (c) R_{IS} = 55 m, (d) R_{IS} = 60 m, (e) R_{IS} = 80 m31

2.9 Iso-surfaces of incident radiation (kW/m^2) at different RIS for LPG pool fire (D =16.9 m): (a) R_{IS} = 20 m, (b) R_{IS} = 40 m, (c) R_{IS} = 55 m, (d) R_{IS} = 60 m, (e) R_{IS} = 80 m32

2.10 Comparison of incident radiation (kW/m^2) among empirical models, experimental data and CFD simulations in large LPG pool fires: D = 12.9 m, u_W = 3 m/s. 33

Figure Page

2.10 Comparison of incident radiation (kW/m^2) among empirical models, experimental data and CFD simulations in large LPG pool fires: D = 12.9 m, u_W = 3 m/s. 33

2.11 Comparison of incident radiation (kW/m^2) among empirical models, experimental data and CFD simulations in large LPG pool fires: D = 14.9 m, u_W = 2.5 m/s. 34

2.12 Comparison of incident radiation (kW/m^2) among empirical models, experimental data and CFD simulations in large LPG pool fires: D = 16.9 m, u_W = 0. 34

2.13 The maximum/average incident radiation predicted by CFD simulations for large LPG pool fires. 36

3.1 Definition of the flame height H and flame tilt angle θ. 47

3.2 Flow domain and the structured hexahedral final mesh for LPG pool fire simulations (D = 10.4 m and $\dot{m}$ = 8.406 kg/s).....50

3.3 Relationships between burning rates $\dot{m}$ and pool diameters (10.4 m ≤ D ≤ 16.9 m) with three different models in large LPG pool fires. 53

3.4 Predicted flame configurations of large LPG pool fires (D = 16.9 m, u_w = 0) colored by temperature (K) using three different burning rates: (a) $\dot{m}$ = 12.770 kg/s (Liu et al., 2009), (b) $\dot{m}$ = 22.196 kg/s (Johnson et al., 1980), (c) $\dot{m}$ = 24.986 kg/s (Zabetakis & Burgess, 1961). 54

3.5 Temperature (K) profiles of large LPG pool fires (D = 10.4 m) with different wind velocities: (a) u_w = 0, (b) u_w = 0.5 m/s, (c) u_w= 2.5 m/s, (d) u_w = 3 m/s. 56

3.6 Temperature (K) profiles of large LPG pool fires (D = 12.9 m) with different wind velocities: (a) u_w = 0, (b) u_w = 0.5 m/s, (c) u_w= 2.5 m/s, (d) u_w = 3 m/s. 56

3.7 Temperature (K) profiles of large LPG pool fires (D = 14.9 m) with different wind velocities: (a) u_w = 0, (b) u_w = 0.5 m/s, (c) u_w= 2.5 m/s, (d) u_w = 3 m/s. 57

3.8 Temperature (K) profiles of large LPG pool fires (D = 16.9 m) with different wind velocities: (a) u_w = 0, (b) u_w = 0.5 m/s, (c) u_w= 2.5 m/s, (d) u_w = 3 m/s. 57

3.9 Relationships between the nondimensionalized flame height H/D and nondimensionalized air velocity u^* ($0 \le u^* \le 1.46$) with D = 10.4 m. 59

3.10 Relationships between the nondimensionalized flame height H/D and nondimensionalized air velocity u^* ($0 < u^* \le 1.35$) with D = 12.9 m. 59

Figure Page

3.11 Relationships between the nondimensionalized flame height *H/D* and nondimensionalized air velocity u^* ($0 < u^* \leq 1.23$) with D = 14.9 m. 60

3.12 Relationships between the nondimensionalized flame height *H/D* and nondimensionalized air velocity u^* ($0 < u^* \leq 1.29$) with D = 16.9 m. 60

3.13 Relationships between nondimensionalized flame tilt tanθ and nondimensionalized wind velocity u^* ($0 \leq u^* \leq 1.46$) with D = 10.4 m. 63

3.14 Relationships between nondimensionalized flame tilt tanθ and nondimensionalized wind velocity u^* ($0 \leq u^* \leq 1.35$) with D = 12.9 m. 63

3.15 Relationships between nondimensionalized flame tilt tanθ and nondimensionalized wind velocity u^* ($0 \leq u^* \leq 1.23$) with D = 14.9 m. 64

3.16 Relationships between nondimensionalized flame tilt tanθ and nondimensionalized wind velocity u^* ($0 \leq u^* \leq 1.29$) with D = 16.9 m. 64

4.1 Newtonian and non-Newtonian mucus viscosities employed in this study……73

4.2 Schematic of the computational domain with the hybrid mesh details in the two mouth-to-trachea (MT) upper airway models with different mucus thicknesses σ: (a) Schematic of the MT upper airway geometry, (b) Mesh details of the MT upper airway geometry with σ = 1.0 mm, (c) Mesh details of the MT upper airway geometry with σ = 0.5 mm 76

4.3 Mesh independence tests for the two MT models: (a) σ=1.0 mm; (b) σ=0.5 mm77

4.4 Expiratory cough waveforms with different intensities at the trachea openings 79

4.5 Comparison of computational results for a straight tube with experimental data (Kim, Greene, et al., 1986): (a) Relationship between mucus thickness and airflow velocity, (b) Relationship between mucus velocity and airflow velocity, and (c) Relationship between mucus volume fraction and airflow velocity.. 82

4.6 Mucus clearance efficiency in the MT model with Newtonian mucus under different conditions: (a) CS-I and σ =1.0 mm, (b) CS-I and σ = 0.5 mm, (c) CS-II and σ=1.0 mm, (d) CS-II and σ = 0.5 mm 85

4.7 Mucus clearance efficiency in the MT model with non-Newtonian mucus under different conditions: (a) CS-I and σ =1.0 mm, (b) CS-I and σ = 0.5 mm, (c) CS-II and σ =1.0 mm, (d) CS-II and σ = 0.5 mm.. 86

Figure Page

4.8 Nondimensionalized velocity profiles and mucus volume fraction at the cross-section C-C' computed with different cough strengths and mucus properties at different time stations in a cough-wave: (a) t = 0.05 s, (b) t = 0.09 s, (c) t = 0.40 s. 87

4.9 Nondimensionalized velocity profiles V* and mucus volume fraction α_m at the cross-section D-D' computed with different cough strengths and mucus properties at different time stations in a cough-wave: (a) t = 0.05 s, (b) t = 0.09 s, (c) t = 0.40 s....88

4.10 Mucus distributions in the sagittal plant (Z = 0) with CS-I at t = 0.09 s with different mucus thicknesses and mucus rheological properties: (a) σ =1.0 mm with Newtonian fluid, (b) σ = 0.5 mm and Newtonian fluid, (c) σ =1.0 mm and non-Newtonian fluid, (d) σ = 0.5 mm and non-Newtonian fluid.....89

4.11 Velocity magnitudes in the sagittal plane (Z = 0) with CS-I at t = 0.09 s (cough-wave peak) under different mucus thicknesses and mucus rheological properties: (a) σ =1.0 mm with Newtonian fluid, (b) σ = 0.5 mm and Newtonian fluid, (c) σ = 1.0 mm and non-Newtonian fluid, (d) σ = 0.5 mm and non-Newtonian fluid 90

4.12 Velocity vectors in selected planes C-C' and D-D' with CS I at t=0.09s with different mucus properties: (a) σ =1.0 mm with Newtonian fluid, (b) σ =1.0 mm and non-Newtonian fluid, (c) σ = 0.5 mm and Newtonian fluid, (d) σ = 0.5 mm and non-Newtonian fluid 91

4.13 Velocity vectors in selected planes C-C' and D-D' with CS II at t = 0.09s with different mucus characteristics: (a) σ =1.0 mm with Newtonian fluid; (b) σ =1.0 mm and non-Newtonian fluid; (c) σ = 0.5 mm and Newtonian fluid; (d) σ = 0.5 mm and non-Newtonian fluid. 92

4.14 Mucus distributions in the sagittal plane (Z = 0) with CS-I at t = 0.40s under different mucus thicknesses and mucus rheological properties: (a) σ =1.0 mm with Newtonian fluid; (b) σ = 0.5 mm and Newtonian fluid; (c) σ =1.0 mm and non-Newtonian fluid; (d) σ = 0.5 mm and non-Newtonian fluid.....97

4.15 Velocity magnitudes in the sagittal plane (Z = 0) with CS-II at t = 0.40s (cough-wave peak) under different mucus thicknesses and mucus rheological properties: (a) σ =1.0 mm with Newtonian fluid; (b) σ = 0.5 mm and Newtonian mucus; (c) σ =1.0 mm and non-Newtonian mucus; (d) σ = 0.5 mm and non-Newtonian fluid. 98

4.16 Distributions of non-Newtonian mucus in different regions (t = 0.5126 s): (a) σ =1.0 mm and CS-I; (b) σ =1.0 mm and CS-II; (c) σ =0.5 mm and CS-I; (d) σ =0.5 mm and CS-II. 99

Figure Page

A. 1 Logical dependence of averaged scalars on mean mixture fraction, the mixture fraction variance, mean enthalpy, and the chemistry model.....137

A. 2 Relationship of mixture fractions in the non-premixed combustion system. .138

A. 3 Graphical scheme of probability density function. 141

B. 1 Schematic of the computational domain with the poly-hexcore mesh details in the straight tube.....147

B. 2 Mesh independence test in the straight tube.....148

CHAPTER I

INTRODUCTION

1.1 Research Motivation

To achieve the goal of clean cooking and heating by 2030, the demand for liquefied petroleum gas (LPG) as a low-pollution fuel is increasing rapidly (Kojima, 2011). Pool fire can be generated if there is an LPG leakage during transportation or at storage sites. Thus, to understand the underlying mechanisms of how the hazardous matter can be generated from the LPG pool fire and delivered dose into the human lung, and evaluate the exposure risks, it is necessary to systematically study the LPG pool fire rheology and the generation, transport, and deposition of the generated aerosolized toxicants from the pool fire to human respiratory system. Computational Fluid Dynamics (CFD) has the unique advantages to investigate the transport phenomena of LPG pool fire generated toxicants by providing high-resolution airflow field and toxicant concentration distributions in the indoor environment and human respiratory systems (Vasilopoulos, Mentzos, Sarris, & Tsoutsanis, 2018; Yuan, Zhou, & Smith, 2016). Such quantitative data are not able to be obtained noninvasively from experiments (Ma et al., 2009). Specifically, CFD simulations can help us to study the properties of large-scale LPG pool fires that have not been well investigated by experiments. Also, CFD simulations can be much helpful for investigating mucus movement rheology and toxic gas deposition behaviors in lung airways systematically, which are extremely difficult to carry out *in vivo*. Therefore, the CFD models validated

by some experiments *in vitro* can serve as a feasible approach to unveil the causal relationships between pool fire characteristics throughout the fire, mucus transport characteristics and deposition behaviors of toxic gases and heat flux in the respiratory systems associated with different exposure conditions.

This research was to develop an experimentally validated CFD model to study the behaviors of large LPG pool fire and its potential health risks to the ambient environment and personnel. The underlying mechanisms of large LPG pool fire and the transport dynamics of its aerosolized toxic products in human respiratory systems are still lacking systematic studies. As the key factors, the radiative heat flux and the toxic matter concentrations generated by large LPG fires can be significantly affected by multiple variables, i.e., burning rate (pool size), flame height, and wind velocity. After being inhaled, the delivered lung dose of toxic gas is highly dependent on the mucus movement and breathing patterns (Fahy & Dickey, 2010; Labiris & Dolovich, 2003). Using the experimentally validated CFD models, we can characterize different factors and represent the scenarios of large LPG pool fires, mucus transport behaviors, and toxic matters deposition in the lung airways by the first principles of physics and chemistry, which can be used to analyze transport phenomena and improve prognosis.

Concerning the potential risks induced by large LPG pool fires, the radiation and configuration of the fire must be investigated. A large-scale LPG pool fire with a diameter larger than 10 m (Welch Stephen, Carvel Richard, & Torero José, 2007), which is difficult to be studied experimentally, can lead to severe consequences and losses with the high emitted heat flux to its surroundings. Specifically, although experiments have been done to investigate the flame height and wind effect on the flame shape of LPG pool fires with the diameters of the pool fires less than 10 m (Droste & Schoen, 1988; Hiroshi & Koseki, 2001b; Johnson et al., 1980; Palazzi & Fabiano, 2012), large-scale LPG pool fires have not been well investigated by experiments due to the high costs,

measurement difficulties, and safety considerations (A. Trouvé, 2008; Vasanth, Tauseef, Abbasi, & Abbasi, 2013), and the correlations developed based on small pool fires may lead to significant errors when being applied to large-scale pool fires (A.G.A., 1974; Moorhouse, 1982; Steward, 1970b; P. H. Thomas, 1963; Welker & Sliepcevich, 1966b). Therefore, to partially address the abovementioned problems, this work aimed to develop and validate a CFD model to reveal the fundamental combustion mechanisms on the progression of large LPG pool fires.

The toxic products and high-temperature air from LPG pool fires pose pulmonary health risks to the residents and firefighters close to the fire. Specifically, exposure to toxic gases and particles generated by large LPG pool fires can lead to death in minutes or cause various lung diseases (Aurell et al., 2015; Aurell et al., 2017). Accurate information for the transport and deposition of such aerosols in the respiratory system is critically needed for precise health risk assessment. However, this mechanism of transport and deposition of the transient toxic particles is not well understood in the respiratory system, especially with the physiologically realistic mucus clearance. The effectiveness of mucus movement and clearance are highly related to the appropriate mucus rheological properties (Yeates, 1990). Although early research efforts exist on modeling mucus movement (Paz, Suarez, Parga, & Vence, 2017; Paz, Suárez, & Vence, 2017; Paz, Suarez, Vence, & Cabarcos, 2019; Rajendran & Banerjee, 2019), the mucus movement and clearance have not been modeled and studied between chronic obstructive pulmonary disease (COPD) and healthy lungs yet. Therefore, to better and more accurately assess the health risks from LPG pool fires to the human respiratory system, a more physiologically realistic environment needs to be developed with the consideration of mucus clearance and transport properties in the lung airways using a Volume of Fluid (VOF) model. Furthermore, to explore the clearance efficiency of inhaled foreign particles and toxic gases from large LPG pool fires, the experimentally validated VOF model can be integrated with the existing Discrete Phase Model (DPM) (Y. Feng et al., 2018; Pozzetti & Peters, 2018) to track inhaled foreign aerosols, which has been designed as part of future work.

Specifically, integrating the outcomes generated from Aims I and II, Aim III (see Figure 1.1) will numerically track delivery patterns of generated toxic matter in a representative human respiratory system inside a virtual human model (Zhao, Feng, Bezerra, Wang, & Sperry, 2019) (see Future Work in Figure 1.1). The work in this study is significant since it can not only provide quantitative evidence to enhance the fundamental understanding of the characteristics of large LPG pool fire and build a more realistic upper airways to investigate toxic particles transport behaviors the human respiratory system, but also provide more insights to governmental agencies and/or professional associations for better safety control during the rescue activities for firefighters. In addition, the developed models can be revised and extended to predict transport behaviors of fires and the related toxic products with other types of fuels.

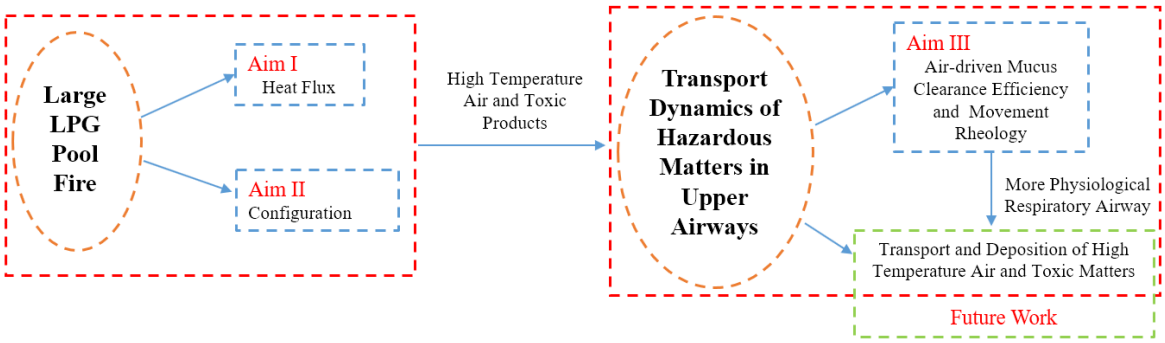

Figure 1.1 The overall workflow of specific aims.

1.2 Literature Review

1.2.1 Heat Radiation from Large LPG Pool Fires

The heat flux from LPG pool fire can increase the health risks and cause significant damages to individuals, process equipment, storage tanks, and appliances (Krishna S. Mudan, 1984; Pourdarvish, Khajehnajafi, & Cowles, 2010). To reduce such risks, safety standards have been made and executed regulating the minimum separation distances from LPG facilities to exposures and upper limits of thermal radiation to individuals or structures (McGrattan, Baum, & Hamins,

2000). However, discrepancies in the regulations need to be addressed and fine-tuned. For example, in the spacing requirements for LPG facility to its surroundings, the minimum space for LPG vaporizers to a container in NFPA 58 is 3 m (NFPA58, 2017) and while in NFPA 59 is 15 m (NFPA59, 2018). Nevertheless, the thermal exposure criteria are also varying from different standards and regulations (49CFR, 2018; API-Standard521, 2014; EN1473, 2016; NFPA, 2016). Therefore, a better understanding of the radiated heat flux from LPG pool fires can provide not only essential information to manage the risks throughout the processes of production, transportation, and utilization, but also the high-resolution quantitative evidence to regulatory agencies to revise current requirements precisely.

Although some experiments have been carried out to investigate the characteristics of hydrocarbon pool fires in the past several decades (V. Babrauskas, 1983; Babrauskas, 2002; Cowley & Johnson, 1992; Fu, 1974; May & McQueen, 1973; Muñoz, Arnaldos, Casal, & Planas, 2004), none of them paid much attention to large LPG pool fires due to expensive costs and security considerations for experiment testing. Currently, CFD methods become increasingly popular to be applied into investigating the properties of different fire scenarios (Attar, 2013; Hostikka, 2003; Joshi, Bikkina, & Wang, 2016; Rengel, Mata, Pastor, Casal, & Planas, 2018; Sinai & Owens, 1995; Sun, Guo, & Pareek, 2014, 2015; Vasanth, Tauseef, Abbasi, & Abbasi, 2015; W. Wang, T. He, W. Huang, R. Shen, & Q. Wang, 2018; Z. Wang, Wang, & Wang, 2016), and has been well-validated that it can be an effective and non-invasive manner to study pool fire properties (Attar, 2013; Hostikka, 2003; Rawat, 2002; Rengel et al., 2018; Sinai & Owens, 1995; Sun et al., 2014, 2015; Vasanth et al., 2015). Thus, integrating the limited experimental values (K. S. Mudan, 1984), CFD simulation can be an accessible approach to predict the radiative heat flux from large LPG pool fires.

1.2.2 Configuration of Large LPG Pool Fires Using CFD Method

Accurate predictions of the fire configuration play a significant role when applying the solid flame model (SFM) or point source model (PSM) to assess the risks of heat radiation from a fire. Experiments have been done to investigate the flame height and wind effect on the flame shape of LPG pool fires (Droste & Schoen, 1988; Hostikka, 2003; Johnson et al., 1980; Palazzi & Fabiano, 2012), while they only focused on small-scale fires with pool diameters less than 10 m, and large-scale LPG pool fires have not been well investigated by experiments due to the high costs, measurement difficulties, and safety concerns (A. Trouvé, 2008; Vasanth et al., 2013; Yi, Feng, & Wang, 2019). Nevertheless, there are many empirical or semi-empirical models and correlations developed based on experimental data for the flame height and tilt from small-scale pool fires (A.G.A., 1974; Moorhouse, 1982; Steward, 1970b; P. H. Thomas, 1963; Welker & Sliepcevich, 1966b). These models may lead to significant errors when being applied to large-scale pool fires. So far, there are no specific correlations to predict flame height and flame tilt for large LPG pool fires with a diameter larger than 10 m. Therefore, more reliable and accurate correlations for flame height and tilt should be developed to enhance the fundamental understanding of the large LPG pool fire configurations.

1.2.3 Mucus Rheology in Upper Lung Airways

Human pulmonary airways are covered with a layer of viscous mucus (Y. Y. Hu et al., 2015), which acts as a diffusional barrier to pathogens and airborne particulates, as well as a moisture barrier to prevent dehydration of the surface in respiratory tracts (Fahy & Dickey, 2010; Knowles & Boucher, 2002; Mitran, 2013; Rajendran & Banerjee, 2019; Silberberg, 1982; Spagnolie, 2015). Mucus is identified as a non-Newtonian fluid (Yeates, 1990), and presents the behaviors of viscoelasticity (Hill et al., 2014; Lai, Wang, Wirtz, & Hanes, 2009) and shear-thinning (Basser, McMahon, & Griffith, 1989; Quraishi, Jones, & Mason, 1998). In a healthy lung, the mucus thickness is about 2-4% (5-10 μm) of the airway diameter (Manolidis, Isabey, Louis, Grotberg, & Filoche, 2016; Samet

& Cheng, 1994) which is acceptable, and will not increase the burden on inspiration and exhalation (Zheng, 2011). Effective mucus clearance is a critical natural airway defense mechanism, and it can enhance the clearance efficiency of inhaled pathogens, toxic gases, and particles under appropriate conditions (Button & Boucher, 2008).

Mucociliary clearance and interaction with the airflow are two main mechanisms to remove the mucus away from pulmonary airways (Fahy & Dickey, 2010; Levy, Hill, Forest, & Grotberg, 2014; C. P. van der Schans, Postma, Koeter, & Rubin, 1999). While with lung diseases, i.e., COPD and asthma, mucus will be hyper-secreted, leading to ciliary motion impaired (Zheng, 2011). Nevertheless, the mucus with a high viscosity will decrease the effectiveness of mucus clearance, reduce gas exchange, and incur inflammation (Button & Boucher, 2008; Lai et al., 2009). Although several experiments have been carried out to investigate the mechanism of mucus clearance driven by airflow in the past several years (Camassa, Forest, Lee, Ogrosky, & Olander, 2012; C. S. Kim, Greene, Sankaran, & Sackner, 1986; C. S. Kim, Iglesias, & Sackner, 1987; C. S. Kim, Rodriguez, Eldridge, & Sackner, 1986; King, Brock, & Lundell, 1985), it is still impossible to investigate the behaviors of mucus clearance process with studies *in vivo*. Alternatively, the CFD method is increasingly popular and has been employed to investigate the mucus movement mechanism in the pulmonary system (Paz et al., 2019; Rajendran & Banerjee, 2019; Ren et al., 2020). Specifically, an investigation (Paz et al., 2019) has been conducted to study the mucus clearance from mouth to trachea using a transient VOF model, and discovered that an oscillating airflow can enhance the clearance by up to 5% than a steady airflow. Another study (Rajendran & Banerjee, 2019) also employed a VOF model to investigate mucus transport and distribution by steady expiration in an idealized airway geometry and reviled that the curved structure in the airways can lead to a local mucus redistribution reducing. However, a parametric study still needs to be conducted to investigate the parameters, i.e., Newtonian and non-Newtonian viscosities, mucus thicknesses, cilia

motion, thermal processes, and breath patterns, which may play a significant role during the process of mucus movement in lung airways.

1.3 Research Objectives and Novel Contributions

1.3.1 Research Objectives

Based on the literature review in Section 1.2 (i.e., 1.2.1, 1.2.2, and 1.2.3), the specific research objectives (see Figure 1.1) were planned as follows:

- Aim I was designed to estimate the surface emissive power (SEP), predict the incident radiation from large LPG pool fires to the surrounded objects and develop the reasonable minimum distances between the pool fire and objects using CFD simulations.
- In Aim II, the characteristics of burning rate, flame height, and flame tilt of large LPG pool fires have been well investigated and compared using empirical models, correlations, and CFD simulations. Subsequently, two new correlations for flame heights and one new correlation for flame tilts are proposed with better accuracy specifically for large-scale LPG pool fires.
- In Aim III, an experimentally validated VOF model has been developed to conduct a quantitative analysis to investigate the effects of cough intensity and initial mucus thicknesses on the mucus transport and clearance in a mouth-to-trachea airway geometry using an experimentally validated VOF based multiphase model. The VOF model developed in this work can be further refined and integrated with Discrete Phase Models (DPMs) to predict the mucus clearance effect on inhaled toxic particles/gases generated by LPG pool fires explicitly.

1.3.2 Novel Contributions

Of the stated research objectives, novel contributions are:

- An alternative manner rather than an experimental approach to investigate the mechanisms of large LPG pool fires.
- Proposed safe separation distances to satisfy the requirements of different codes using the developed CFD model.
- A new correlation for the surface emissive power in LPG (100% propane) pool fire (10 m $\leqslant$ D $\leqslant$ 20 m) with fewer relative errors than other empirical models.
- Two new correlations for the flame height and tilt angle for large LPG pool fires contributing more accurate predictions than any existing empirical models.
- A general mechanism of cough-driven mucus clearance and transport behaviors to assist other researchers and scientists to build a more physiologically realistic upper airway model which can predict the clearance and transport behaviors of the toxic matters and hot temperature air in a large LPG pool fire scenario.

CHAPTER II

PREDICTIONS OF HEAT RADIATION FROM LARGE LIQUEFIED PETROLEUM GAS POOL FIRES

2.1 Introduction

Liquefied petroleum gas (LPG) has been used widely in many applications, including utility, cooking, and heating appliances (Kojima, 2011). Potential risks need to be well controlled when using LPG. The risks include pool fires generated by the unintentional ignition of leaked LPG. The heat flux from the pool fire would increase personnel risks and cause significant damages to individuals, process equipment, storage tanks, and appliances (Khajehnajafi, Pourdarvish, & Cowles, 2010; Krishna S. Mudan, 1984). To reduce such risks, standards have been made and executed regulating the minimum separation distances from LPG facilities to sourrouded objectives and upper limits of thermal radiation to individuals or structures (McGrattan et al., 2000). However, there are discrepancies that need to be addressed and fine-tuned. For example, in the spacing requirements for LPG facility to its surroundings, the minimum space for LPG vaporizers to a container in NFPA 58 is 3 m (NFPA, 2014) and while in NFPA 59 is 15 m (NFPA, 2016). The thermal exposure criteria are also varying from different standards and regulations (49CFR, 2018; API-Standard521, 2014; EN1473, 2016; NFPA, 2016) shown in Table 2.1.

Table 2.1 Thermal exposure criteria in standards and regulations.

Thermal radiation flux (kW/m^2)	Conditions	Reference
5	No less than 10 individuals outside the plant boundary, or at least one person inside the building suffer second-degree skin burns on at least 10% of their bodies within 30 s of exposure to the fire.	NFPA 59A (NFPA, 2016)
32	Loss of strength of structural steel.	
9.46	Maximum heat flux at any location where urgent emergency action is required for individuals.	API 521 (API-Standard521, 2014)
6.31	Maximum heat flux in areas where emergency actions within 30 s are required for individuals without shielding but with proper clothing.	
4.73	Maximum heat flux in areas where emergency actions within 2 to 3 mins are required by individuals without shielding but with proper clothing.	
1.58	Maximum heat flux at any location where individuals with proper clothing can be continuously exposed.	
5	A property line can be built to ignite a design spill.	49 CFR (49CFR, 2018)
9	The closest point of the structure outside the individual's property line.	
30	A property line can be built upon for fire over an impounding area containing liquefied natural gas (LNG).	
32	The concrete outer surface of adjacent storage tanks.	EN 1473 (EN1473, 2016)
15	The outer mental surface of adjacent storage tanks.	
15	The outer surfaces of adjacent pressurized storage vessels and process facilities.	
8	Control rooms, maintenance workshops, laboratories, warehouses, etc.	
5	Administrative buildings.	
8	Remote area: an area only infrequently occupied by small numbers of persons.	
1.5	Critical area: This is either an unshielded area of critical importance where people without protective clothing can always be required, including during emergencies or urban area or a place difficult or dangerous to evacuate at a limited time.	
5	Other areas: Other areas typically include industrial areas not under the control of the operator/occupier of the liquefied natural gas LNG facilities.	

In the past decades, many experiments have been carried out to investigate the characteristics of hydrocarbon pool fires (V. Babrauskas, 1983; Babrauskas, 2002; Cowley & Johnson, 1992; Fu, 1974; May & McQueen, 1973; Muñoz et al., 2004), while none of them paid much attention to large LPG pool fires due to expensive costs and security considerations for experiment testing. Currently, CFD simulation method has become increasingly popular to be applied to investigating the properties of different fire scenarios (Joshi et al., 2016; W. Wang, T. F. He, W. Huang, R. Shen, & Q. Wang, 2018; Z. Wang et al., 2016) employed CFD methods to analyze the impacts of pool shape, bund and ambient turbulence on the fire plume shape in kerosene pool fires. Rawat et al. (Rawat, 2002) used the unsteady flamelet approach to investigate the chemical reaction mechanisms of soot formation on a methane pool fire with 1 m diameter. Hostikka et al. (Hostikka, 2003) used large-eddy simulation to simulate heat flux from methane pool fires ($0.1\ \text{m} \leq D \leq 1\ \text{m}$) and found good agreements with experimental measurements. Small-size pool fires ($D \leq 0.2$ m) for gasoline, kerosene, and tert-Butyl peroxybenzoate (TBPB) have been carried out to analyze the flame temperature and radiation of the corresponded pool fires (Attar, 2013). Sun et al. (Sun et al., 2014, 2015) used large eddy simulation to analyze the radiated heat flux from LNG pool fires to estimate the distance between LNG tanks and vaporizers. Vasanth et al. (Vasanth et al., 2015) found the exceptional agreement between experimental findings of pool fires situated at differing elevations and CFD simulations. Rengel et al. (Rengel et al., 2018) carried out a priori validation and found out that wind speeds and pool diameters are crucial factors influencing the accuracy of the predictions from both codes of Flame Acceleration Simulator Fire (FAS) and Fire Dynamics Simulation (FDS).

Therefore, a better understanding of the radiated heat flux from LPG pool fires can provide not only essential information to manage the risks throughout the processes of production, transportation, and utilization but also the high-resolution quantitative evidence to regulatory agencies to revise current requirements precisely. To address the abovementioned concerns, we

have conducted the novel research work of estimating the surface emissive power (SEP), predicting the incident radiation from large LPG pool fires (10 m $\leqslant D \leqslant$ 20 m) to the surrounded objects, and proposing the reasonable minimum distances between the pool fire and objects using CFD simulations. Simulation results were compared with data from empirical models, and the CFD method has been validated by experimental measurements (K. S. Mudan, 1984). ICEM CFD 19.2 (ANSYS Inc., Canonsburg, PA) was employed to generate the computational mesh, and ANSYS Fluent 19.2 (ANSYS Inc., Canonsburg, PA) has been used to accomplish the computing tasks. The work accomplished in this chapter has been published in a scientific journal (Yi et al., 2019).

2.2 Research Objectives

Investigating the characteristics of SEP and incident radiated heat flux from large LPG pool fires using a CFD method, several research objectives are listed as follows:

- Developing an experimentally validated CFD model to simulate large LPG pool fire.
- Predicting the SEP in a large LPG pool fire by integrating CFD simulations and numerical correlations.
- Evaluating radiative heat flux from large LPG pool fires with several different pool sizes and windy conditions.
- Fine-tuning the safety separation distances between the fire and surrounding objectives to satisfy corresponding standards and/or codes.

2.3 Theory

2.3.1 Governing Equations

In this study, the non-premixed combustion approach is employed for large LPG pool fire simulations. It is assumed that two separated streams, i.e., LPG vapor and air, enter the reaction zone in non-premixed but evenly distributed streams. With such an assumption, the mixture mass fractions f_i (Sivathanu & Faeth, 1990) need to satisfy:

$$f_{LPG} + f_{sec} + f_{OX} = 1 \tag{2.1}$$

where f_{LPG} is the mass fraction of LPG, f_{sec} is the mass fraction of the second stream, and f_{OX} is the mass fraction of air.

Conservations of mass, momentum, species balance, and energy, as well as key mechanisms of chemical species (Faghri & Sundén, 2008; Yi et al., 2019) for turbulent reacting flows, were employed, discretized, and solved. Specifically, the governing equations are listed as follows:

Continuity Equation

$$\frac{\partial}{\partial x_i}(\rho u_i \overline{f_\iota}) - \frac{\partial}{\partial x_i}\left(\left(\frac{k}{C_p} + \frac{\mu_t}{0.85}\right)\frac{\partial \overline{f_\iota}}{\partial x_i}\right) = 0 \tag{2.2}$$

$$\frac{\partial}{\partial x_i}(\rho u_i \overline{f_\iota'^2}) - \frac{\partial}{\partial x_i}\left(\left(\frac{k}{C_p} + \frac{\mu_t}{\sigma_t}\right)\frac{\partial \overline{f_\iota'^2}}{\partial x_i}\right) = 2.86\mu_t \cdot \left(\frac{\partial \overline{f_\iota}}{\partial x_i}\right)^2 - 2\rho\frac{\varepsilon}{k}\overline{f_\iota'^2} \tag{2.3}$$

$$f_\iota' = f_i - \overline{f_\iota} \tag{2.4}$$

$$f_{sec} = p_{sec}(1 - f_{LPG}) \tag{2.5}$$

Momentum Balance Equation

$$\frac{\partial \rho u_i u_j}{\partial x_j} = -\frac{\partial p}{\partial x_i} + \frac{\partial \tau_{ij}}{\partial x_j} + \rho g_i \tag{2.6}$$

$$\tau_{ij} = \mu\left(\frac{\partial u_i}{\partial x_j} + \frac{\partial u_j}{\partial x_i}\right) - \frac{2}{3}\mu\delta_{ij}\frac{\partial u_k}{\partial x_k} \tag{2.7}$$

Energy Balance Equation

$$\frac{\partial}{\partial x_j}(\rho u_j h) = \frac{\partial q_j}{\partial x_j} + \tau_{ij}\frac{\partial u_i}{\partial x_i} + S_Q \tag{2.8}$$

$$h = \sum_{i=1}^{n} h_i f_i \tag{2.9}$$

$$q_j = \lambda \frac{\partial T}{\partial x_j} + \rho \sum_{i=1}^{n} h_i \left(D_i \frac{\partial f_i}{\partial x_j} \right) \tag{2.10}$$

Chemical Species Transport Equation

$$\rho \frac{\partial}{\partial x_j} \left(u_j f_{LPG} \right) = \rho \frac{\partial}{\partial x_j} \left(D_i \frac{\partial f_{LPG}}{\partial x_j} \right) + M_{LPG} \dot{\omega}_{LPG} \tag{2.11}$$

$$\dot{\omega}_{LPG} = \frac{d[X_{LPG}]}{dt} = -k_G(T)[X_{LPG}]^n [X_{Ox}]^m \tag{2.12}$$

In Eqs. (2.1) to (2.12), ρ is the mixture density, $\overline{f_i}$ is the Favre mean mixture fraction, $\overline{f_i'^2}$ is the mixture fraction variance, p_{sec} is the normalized secondary mixture fraction, u_i is the velocity components in Cartesian coordinate, k is the thermal conductivity of mixture, C_p is the mixture specific heat, μ_t is the turbulent viscosity, p is static pressure, τ_{ij} is constitutive relation for a Newtonian fluid, g_i is the acceleration of gravity, h is the enthalpy, h_i is the enthalpy for species i, S_Q is the energy source term, q_j is the heat diffusion flux defined by Fourier's law, λ is the thermal conductivity, D_i is the mass diffusivity of species i, M_{LPG} is the molecular weight of LPG, $\dot{\omega}_{LPG}$ is the LPG consumption rate, X_{LPG} is the molar concentration of LPG, X_{Ox} is the molar concentration of the oxidizer, and k_G is the reaction rate constant, T is temperature, m is the reaction order for oxidizer, n is the reaction order for LPG.

Re-Normalization Group (RNG) k-ε Model

The Re-Normalization Group (RNG) k-ε model is used to accurately predict the strained flows for LPG pool fire simulation in this study. The RNG k-ε model is also a computationally efficient, robust, and accurate model that can be applied for a wide range of turbulence flow simulations with heat transfer. Compared with the standard k-ε turbulence model, the RNG k-ε model considers the swirl flow and the improvement of the analytical formula for turbulent Prandtl numbers. The transport equations for the RNG k-ε model (Perry, Green, & Maloney, 1984) are listed below:

$$\rho \frac{\partial}{\partial x_i}(ku_i) = \frac{\partial}{\partial x_j}\left(\alpha_k \mu_{eff} \frac{\partial k}{\partial x_j}\right) + G_k + G_b - \rho\varepsilon - Y_M + S_k \tag{2.13}$$

and

$$\rho \frac{\partial}{\partial x_i}(ku_i) = \frac{\partial}{\partial x_j}\left(\alpha_\varepsilon \mu_{eff} \frac{\partial \varepsilon}{\partial x_j}\right) + C_{1\varepsilon}\frac{\varepsilon}{k}(G_k + C_{3\varepsilon}G_b) - C_{2\varepsilon}\rho\frac{\varepsilon^2}{k} - R_\varepsilon - S_\varepsilon \tag{2.14}$$

where G_k is the generation of turbulence kinetic energy, G_b is the generation of turbulence kinetic energy due to buoyancy, Y_M is the contribution of the fluctuating dilatation in the compressible turbulence flow to the overall dissipation rate, α_ε is the inverse of the effective Prandtl number for ε, α_k is the inverse effective Prandtl number for k, as well as R_ε and S_ε are customized source terms.

2.3.2 Surface Emissive Power (SEP)

Surface emissive power, *E*, is defined as the heat flux due to heat radiation at the surface area of the flame. It can be computed with the Stefan-Boltzmann equation from an assumed grey radiator (Van den Bosch & Weterings, 1997) as follows:

$$E = \varepsilon\sigma\left(T_f^4 - T_a^4\right) \tag{2.15}$$

The emissivity ε for luminous and sooty flames, is often approximated by the equation (Drysdale, 2011)

$$\varepsilon = 1 - exp(-kL) \tag{2.16}$$

where L has a slight relationship with the flame geometry of LPG pool fires, is approximately equal to the fire radius *R*. In this work, the fire flame is assumed as a back body, and $\varepsilon = 1$.

In some circumstances, the flame temperature and emission/absorption coefficient data are not available. Another method (Van den Bosch & Weterings, 1997) was coming up that SEP is

appropriate to theoretical SEP, E_{theory}, determined by the heat of combustion with the surface area of the flame expressed by

$$E_{theory} = \frac{\chi_r \dot{Q}}{A} \tag{2.17}$$

and

$$\dot{Q} = \dot{m}\Delta H_C \tag{2.18}$$

where χ_r is related to C/H of fuel compounds (Koseki, 1989) and pool diameters (B. J. McCaffrey & Harkleroad, 1989).

Previous numerical studies (Delichatsios, 1993; Quintiere & Grove, 1998; Souil, Joulain, & Gengembre, 1984; J. C. Yang, Hamins, & Kashiwagi, 1994) presented that the radiative fraction of propane fire flames were ranging from 0.28 to 0.35; and the flame surface area *A* is determined the flame height *H* and fire diameter *D*, i.e.,

$$A = \frac{\pi D^2}{2} + \pi DH \tag{2.19}$$

In the single-zone solid model, the averaged SEP can be determined using the fraction of energy radiated from pool fires (Moorhouse, 1982; K. S. Mudan, 1984; Krishna S. Mudan, 1984; J. C. Yang et al., 1994) given by the following equation:

$$E = \frac{\chi_r \dot{m}'' \Delta H_C}{1 + 4H/D} \tag{2.20}$$

Using the initial fire design and evaluation method, Mudan (Krishna S. Mudan, 1984) proposed a correlation for SEP, which can be expressed by

$$E = 70\exp(-k_1 D) \tag{2.21}$$

where $k_1 = 0.00165$ m^{-1}.

Afterwards, Croce and Mudan (A. Croce & Mudan, 1986) obtained a uniform model for SEP of flames for smoky hydrocarbons as follows:

$$E = E_{max} \cdot exp(-k_1' D) + E_s\left(1 - exp(1 - k_1' D)\right) \tag{2.22}$$

where $E_{max} = 140$ kW/m^2, $E_s = 20$ kW/m^2, and $k_1' = 0.2$ m^{-1}.

In this chapter, the empirical models have been combined with results of CFD simulations to estimate the SEP in large LPG pool fires. Specifically, after comparing with the experimental measurements, a new correlation was developed to predict the SEP in large LPG pool fires (10 m $\leqslant D \leqslant$ 20 m) properly.

2.3.3 Radiative Heat Flux

The radiated heat flux generated by LPG pool fires consists of the contributions of conduction, convection, and radiation (Eq. (2.23)). The semi-quantitative equation to compute heat flux was obtained by Hottel (Hottel, 1959) as follows:

$$\dot{q}^{"} = \dot{q}^{"}_{conv} + \dot{q}^{"}_{cond} + \dot{q}^{"}_{rad} \tag{2.23}$$

In Eq. (2.23), the radiative heat flux plays a significant role in the heat flux from pool fires to objects, while other terms such as conductive and convective heat transfer sources are ignored in existing studies (Drysdale, 2011; Fay, 2006; Krishna S. Mudan, 1984).

To predict $\dot{q}^{"}_{rad}$ from pool fires, the widely accepted point source model (PSM) and the solid flame model (SFM) are often applied. Specifically, PSM is the most applicable configuration model to calculate the radiative heat flux at any distance from the pool fire source with the equation:

$$\dot{q}^{"}_{rad} = \frac{\chi_r \dot{Q}}{4\pi r^2} \tag{2.24}$$

Drysdale (Drysdale, 2011) correlated PSM with the information of the narrow-angle radiometer data for the radiative heat flux to the external target (see Figure 2.1 (a)) with the equation:

$$\dot{q}''_{rad} = \frac{\chi_r cos\beta \dot{Q}}{4\pi r'^2} \tag{2.25}$$

where β is the angle between the normal to the external objects and the line of slight between the object and point source, and r' is determined by r and H. Specifically,

$$r' = \sqrt{\frac{H^2}{4} + r^2} \tag{2.26}$$

SFM (Krishna S. Mudan, 1984) is another widely used model to describing radiative heat flux, $\dot{q}''_{rad}$, to outside targets (see Figures 2.1 (b) & (c)) around the pool fire expressed by

$$\dot{q}''_{rad} = EF\tau \tag{2.27}$$

where F is geometric view factor, and τ is atmospheric transmissivity.

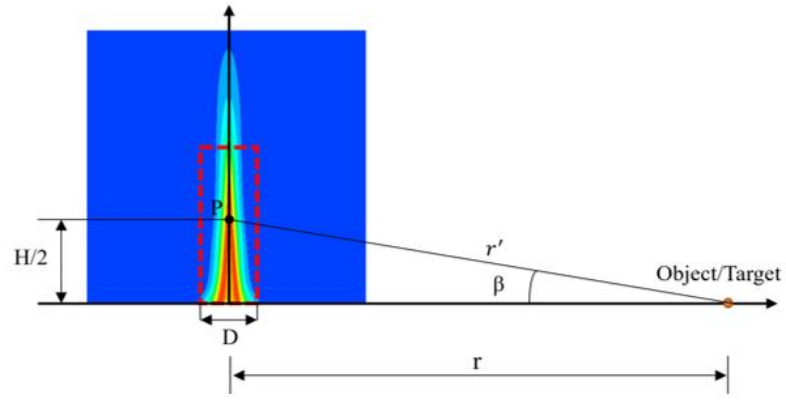

(a) Point source model

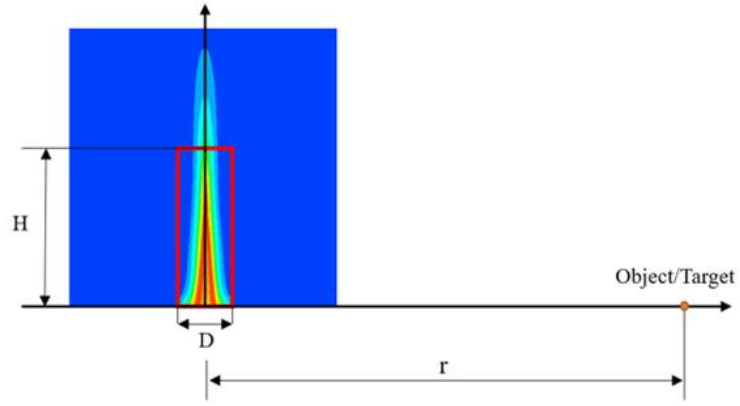

(b) Solid flame model (regular cylindrical flame)

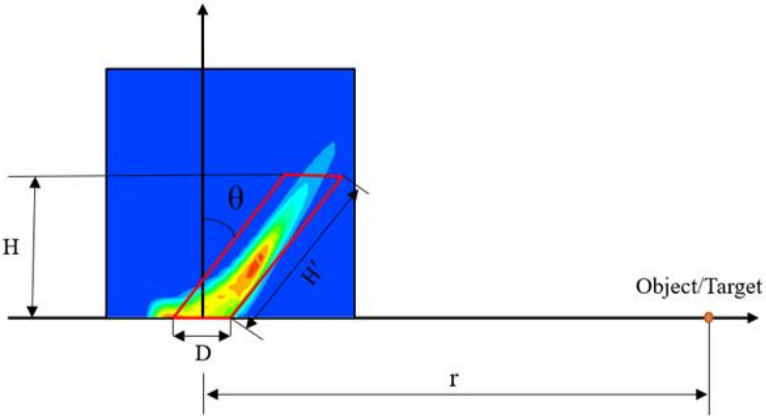

(c) Solid flame model (inclined cylindrical flame)

Figure 2.1 Point source model (PSM) and solid flame model (SFM) to calculate incident radiation from LPG pool fires: (a) point source model; (b) solid flame model (regular cylindrical flame); (c) solid flame model (inclined cylindrical flame).

2.4 Numerical Method

2.4.1 Geometry and Mesh

A 3-D computational domain for a large LPG pool fire at the center has been constructed, with a pool diameter of 16.9 m (see Figure 2.2). The O-Grid blocking strategy was employed the finite volume mesh generation of the cylindrical flame region using ICEM CFD 19.2 (ANSYS Inc., Canonsburg, PA), which is also shown in Figure 2.2. The total mesh cell numbers of the four meshes are 1,184,477 (Mesh 1), 2,885,631 (Mesh 2), 3,694,746 (Mesh 3) and 5,029,535 (Mesh 4). A mesh independence test was performed by refining the mesh until the average percentage of velocity difference V_R was less than 1% between mesh iterations. Specifically, V_R is employed (see Eq. (2.28)) to compare the velocity magnitudes at different locations in the Z-axis direction at the LPG mass flow rate of 44.37 kg/s (K. S. Mudan, 1984). On plane Z = 0, 50 locations have been selected which are randomly distributed in the flow domain. The velocity magnitudes at the locations have been acquired and compared. Specifically, V_R can be calculated by:

$$V_R = \frac{\sqrt{\sum_{m=1}^{50}\left(\frac{v_{m,n+1} - v_{m,n}}{v_{m,n+1}}\right)^2}}{50} \tag{2.28}$$

where n is the mesh index ($n = 1, 2, 3, 4$). Based on the mesh independence test results shown in Figure 2.3, Mesh 3 provides the optimum balance between computational efficiency and accuracy. Specifically, V_R reaches the minimum due to the lowest summation of truncation and round-off errors. Therefore, Mesh 3 was employed as the final mesh for this study.

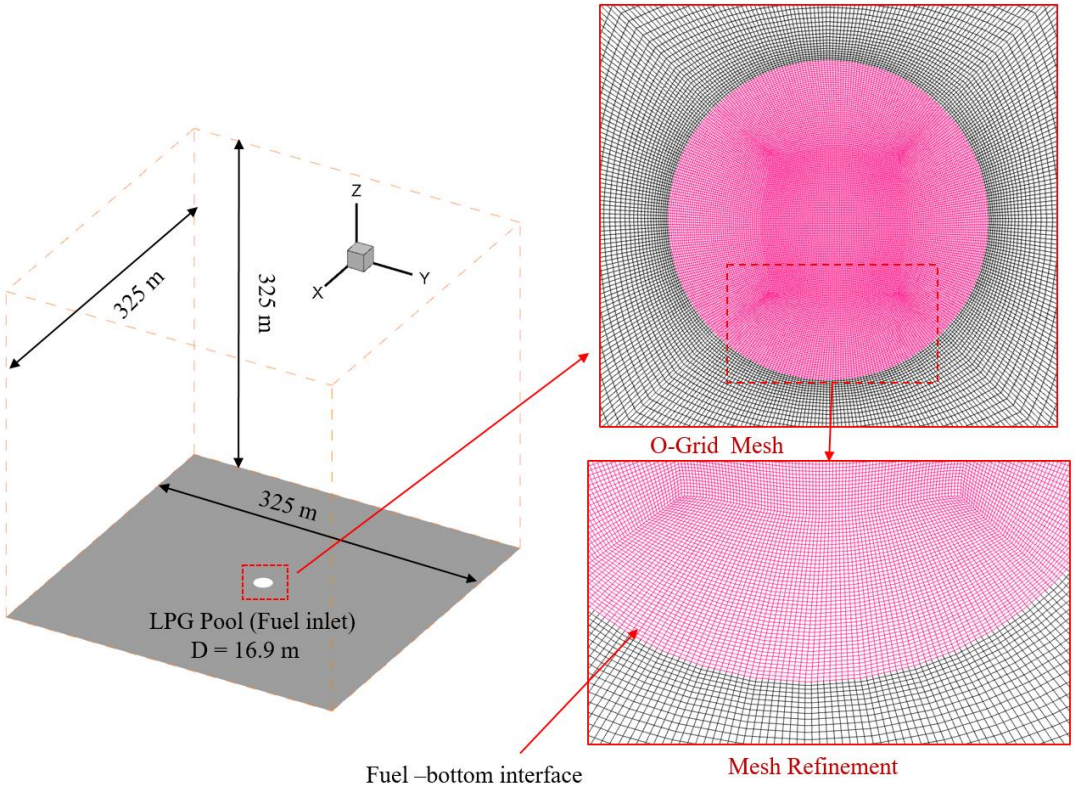

Figure 2.2 LPG pool fire geometry and the structured hexahedral mesh (D = 16.9 m).

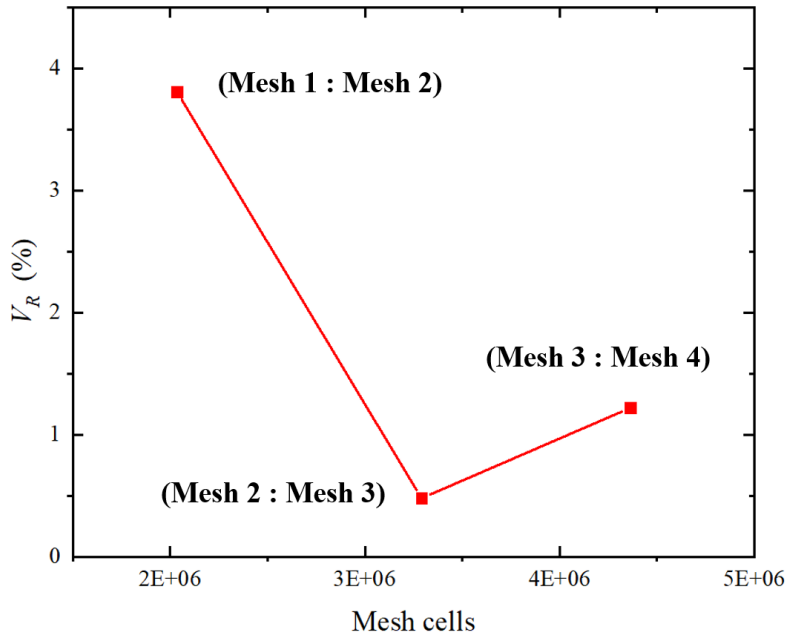

Figure 2.3 Comparisons of V_R in different meshes for mesh independence test.

2.4.2 Numerical Setup

The finite volume method (FVM) was used to discretize the computational domain and solve the governing equations in the CFD simulations. RNG k-ε model (See Appendix A.1) is used as for turbulence modeling, and the P-1 model (see Appendix A.2) (Y.-S. Cheng, Zhou, & Chen, 1999) is selected as the radiation model. Using the fuel stream rich flammability limit and boundary species in the species transport model, the non-premixed combustion method is employed to simulate LPG pool fire with the calculated Probability Density Function (PDF) table (see Appendix A.1). To investigate the pool size effect, the mesh has been scaled with factors of 0.882 and 0.763 for the pools with 12.9 m and 14.9 m in diameters, respectively. Boundary conditions were determined based on the experimental measurements (K. S. Mudan, 1984) and are listed in Table 2.2.

Table 2.2 Boundary conditions of the CFD simulation for large LPG pool fires.

Pool diameter (m)	Atmosphere temperature (K)	Mass burning rate (kg/s)	Wind velocity (m/s)
12.9	309	29.087	3
14.9	306	47.328	2.5
16.9	312	44.426	0

The numerical solution of the governing equations with appropriate boundary conditions was performed by using a user-enhanced, commercial finite-volume based program, i.e., ANSYS Fluent 19.2 (ANSYS Inc., Canonsburg, PA). All variables, including velocity components, pressure, shear rates, and species concentrations, were calculated and located at the centroids of the discretized mesh cells. Simulations were run on a local 64-bit Dell Precision Tower 7810 with 128GB of RAM and 3.40 GHz processors. Second-order upwind schemes were adopted to discretize the governing equations of mass, momentum, turbulent kinetic energy, turbulent dissipation rate, energy, mean mixture fraction, and mixture fraction variance. The coupled scheme was employed for pressure-velocity coupling, and the least squares cell-based scheme was applied to spatial discretization. To

evaluate the convergence, the residuals assigned are 1e-6 for energy and P1, and 1e-3 for the other governing equations.

2.5 Results and Discussion

2.5.1 Prediction of Surface Emissive Power (SEP)

To find the flame temperature T_f and flame height H which are used to calculate the SEP and radiated heat flux from large LPG pool fires by empirical models, the temperature profiles of the three LPG pool fires from CFD simulations are obtained which are shown in Figures 2.4 (a) to (c). (Haegglund & Persson, 1976) claimed that the distinguished temperature for fire flames from the black smoke body is 800 K. In this work, the LPG pool fire scenario is considered as steady state. Accordingly, steady-state CFD solver was employed for the numerical study. Therefore, the temperature is applied in this study to differ the flame zone to smoke zone. The average flame temperatures 1,492, 1,449 and 1,492 K in the large LPG pool fires with the corresponded diameters 12.9, 14.9 and 16.9 m have been used to calculate the SEP in Eq. (2.15). The flame heights in the three large LPG pool fires have been employed to Eq. (2.17), Eq. (2.20), Eq. (2.25), as well as Eq. (2.27). Therefore, with the data obtained from CFD simulations, the empirical models can be validated to estimate the SEP and radiative heat flux from large LPG pool fires.

Using the flame heights and temperatures obtained from Figure 2.4, the SEP for the large LPG pool fires have been obtained by the empirical models and have been compared with experimental data (K. S. Mudan, 1984) shown in Figure 2.5. It can be noticed from Figure 2.4 that only the results from Eq. (2.21) can have a better performance to predict SEP when compared with the experimental data. While other equations exist impressive errors to estimate SEP for large LPG pool fires. Equation (2.15) overestimates the SEP, which is more than two times over the experimental results, and for other equations, such as Eq. (2.17), Eq. (2.20), and Eq. (2.22), the results from these equations, are appropriate while they underestimate SEP from large LPG pool fires. The main

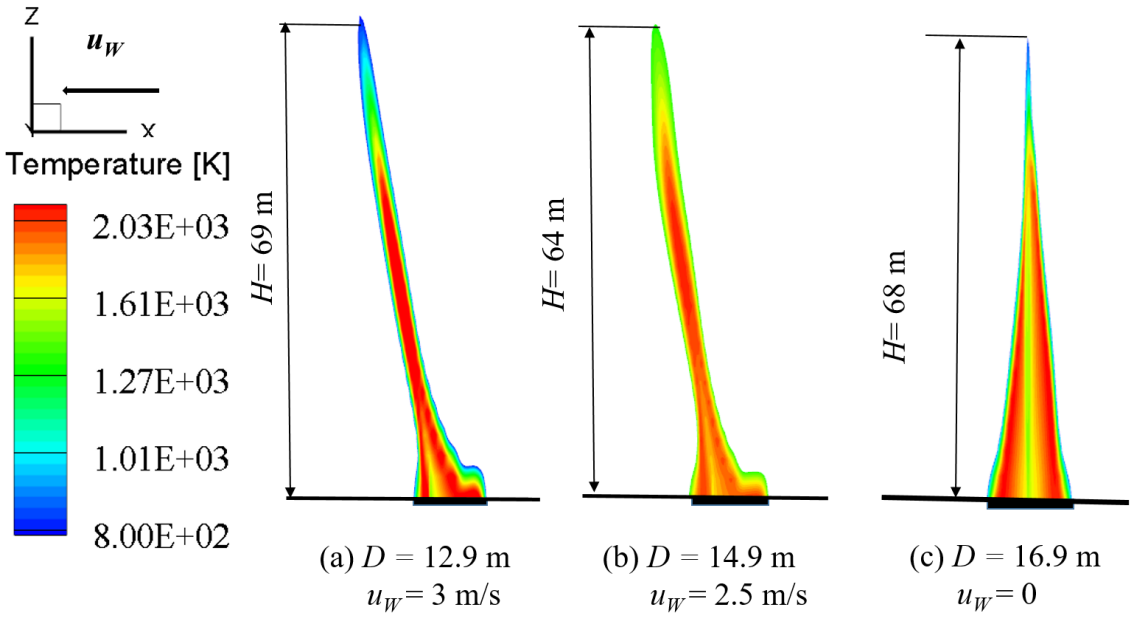

Figure 2.4 Temperature (K) profiles of large LPG pool fires in different sizes and atmosphere conditions: (a) D = 12.9 m, u_W= 3 m/s, (b) D = 14.9 m, u_W= 2.5 m/s, (c) D = 16.9 m, u_W= 0.

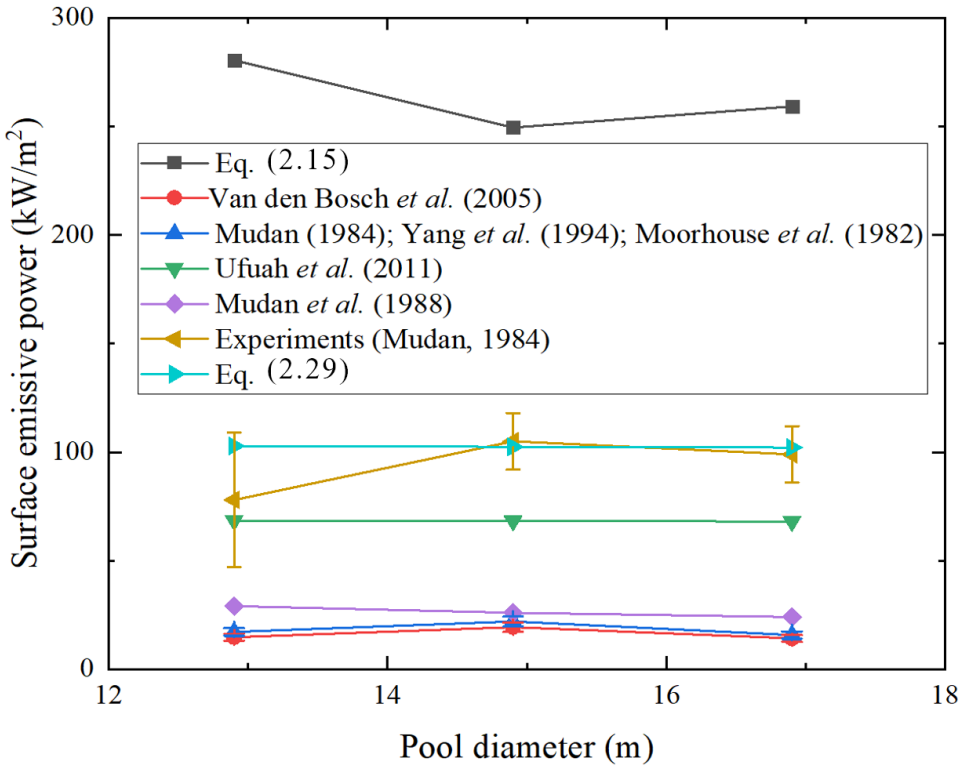

Figure 2.5 Comparison of surface emissive power (kW/m^2) obtained by empirical models, proposed equations, and experiments for large LPG pool fires.

factor for the large errors is due to the inaccuracy of extrapolation from small-scale experiments to large-scale fires when generating the empirical models. Another possible factor is because existing models were not explicitly developed for LPG pool fires. Nevertheless, the results obtained by Eq. (2.21) show that it has a similar trend with the experiment results to predict the SEP for large LPG pool fires. Therefore, to reduce the relative errors between Eq. (2.21) and experiment measurements (K. S. Mudan, 1984), a new equation has been proposed in this study as follows:

$$E = 105\exp(-k_1 D) \quad (10\ \text{m} \le D \le 20\ \text{m}) \tag{2.29}$$

where $k_1 = 0.00165\ \text{m}^{-1}$.

Comparisons of SEPs between numerical studies using Eq. (2.29) and benchmark experimental data are shown in Figure 2.5. The comparison shows that Eq. (2.29) provides more accurate predictions than other correlations and empirical models with less relative errors of the estimated SEP in large LPG pool fires with pool diameters employed in this study (see Table 2.3). It is worth mentioning that the composition of LPG in the United States is pure propane (Hahn, 2019), while the compositions are different in other countries. Therefore, Eq. (2.29) is limited to be used in large LPG pool fires with 100% propane. A more generalized SEP correlation for large LPG pool fires needs to be developed in the future.

2.5.2 Radiative Heat Flux

Figures 2.6 (a) to (c) show the distribution of incident radiation that is obtained by CFD simulations in large LPG pool fires with different diameters and wind speeds. The maximum incident radiation for these pool fires is 22.90 kW/m^2, 27.58 kW/m^2, and 30.87 kW/m^2, respectively. It can be observed from Figure 2.6 that the maximum incident radiation for the pool fire (D = 12.9 m) is smaller than another two pool fires. It might be due to the factor of the burning rate, which is only 29.087 kg/s and much less than the corresponding values of LPG pool fires with the diameters of 14.9 m and 16.9 m. Figure 2.6 also demonstrates that the wind has a significant impact on incident

radiation distribution. The incident radiation is tilted towards the wind direction, and the tilting angle increases with wind speed. The reason for the incident radiation leaning to air direction is because of the enhanced convection of evaporated components released from the LPG pool. Thus, the incident radiation distribution is determined by the shape of the fire flames (see Figure 2.4), which is formed by the distribution of evaporated LPG after its burning.

To obtain the incident radiation at different distances (R_{IS}) to the center of the LPG pool fire, iso-surfaces colored by the radiation magnitude have been visualized in Figure 2.7 to Figure 2.9. Specifically, the iso-surfaces are generated with R_{IS} = 20, 40, 50, 60, and 80 m for all three different large LPG pool fires. R_{IS} values were selected to facilitate the comparisons between the CFD simulation results and the experimental data (see Figures 2.10 to 2.12). Although no experimental data for incident radiation are currently available at R_{IS} = 20 m, simulation results at that distance were still acquired to study distribution conditions of the incident radiation close to the pool fire burning area. Figures 2.6, 2.7(a), 2.8(a), 2.9(a), 2.10, 2.11, and 2.12 integrally demonstrate that the average incident radiation at R_{IS} = 20 m are higher than 10 kW/m^2 in all three investigated pool fires, which can potentially lead to severe damages to the individuals in this area (Table 2.1) (API-Standard521, 2014). Further post-processing of the high-resolution incident radiation distributions can provide quantitative evidence and guide fire departments on how to protect our firefighters from heat radiation risks when approaching centers of large LPG pool fires.

It should also be noticed that the highest incident radiation magnitudes locate near the tops of iso-surfaces, with deviations due to different tilting effects driven by the wind. To understand specific radiation behaviors more systematically, the maximum and average incident radiations of each iso-surface have been obtained, and these results are compared with experimental results and data from empirical models (see Figures 2.10 to 2.12). From Figures 2.7 to 2.12, it can be found that the CFD model employed in this study provides the best accuracy in predicting the incident radiation of

large LPG pool fires, compared with existing empirical models. In Figure 2.10, it shows that SFM (Eq. (2.27)) has better performances to estimate incident radiation from large LPG pool fires than PSM (Eq. (2.15)), and the results from SFM present a similar trend with the maximum values of CFD simulations. Despite that the experimental data for the pool fire (D = 14.9 m) may have noticeable fluctuations when measuring incident radiations, the CFD simulation results show the great fitting with the experiments on radiation distribution from a distance between 20 m to 80 m in the pool fire (D = 14.9 m). Exceptions on good agreements between numerical and experimental data exist at R_{IS} = 40 m, which also can be observed in another two LPG pool fires. In Figures 2.10 to 2.12, it can be observed that the airflow condition has a significant impact on the heat radiation distribution from 45 m to 60 m to the pool fires with diameters 12.9 m and 14.9 m. High wind velocity might also influence the measurement accuracy of the thermocouples in the experiments, which is a possible reason for the deviations between CFD and experimental data with high ambient airflow velocities. Without the wind velocity effects, good agreements between experimental data and CFD results can be seen in Figures 2.10 to 2.12 in the static air condition with the pool diameter 16.9 m. Based on the good overall predictions of the CFD simulation results, the CFD model and the numerical results can be used to estimate the safe separation distances between large LPG pool fires and targets with reasonable accuracy.

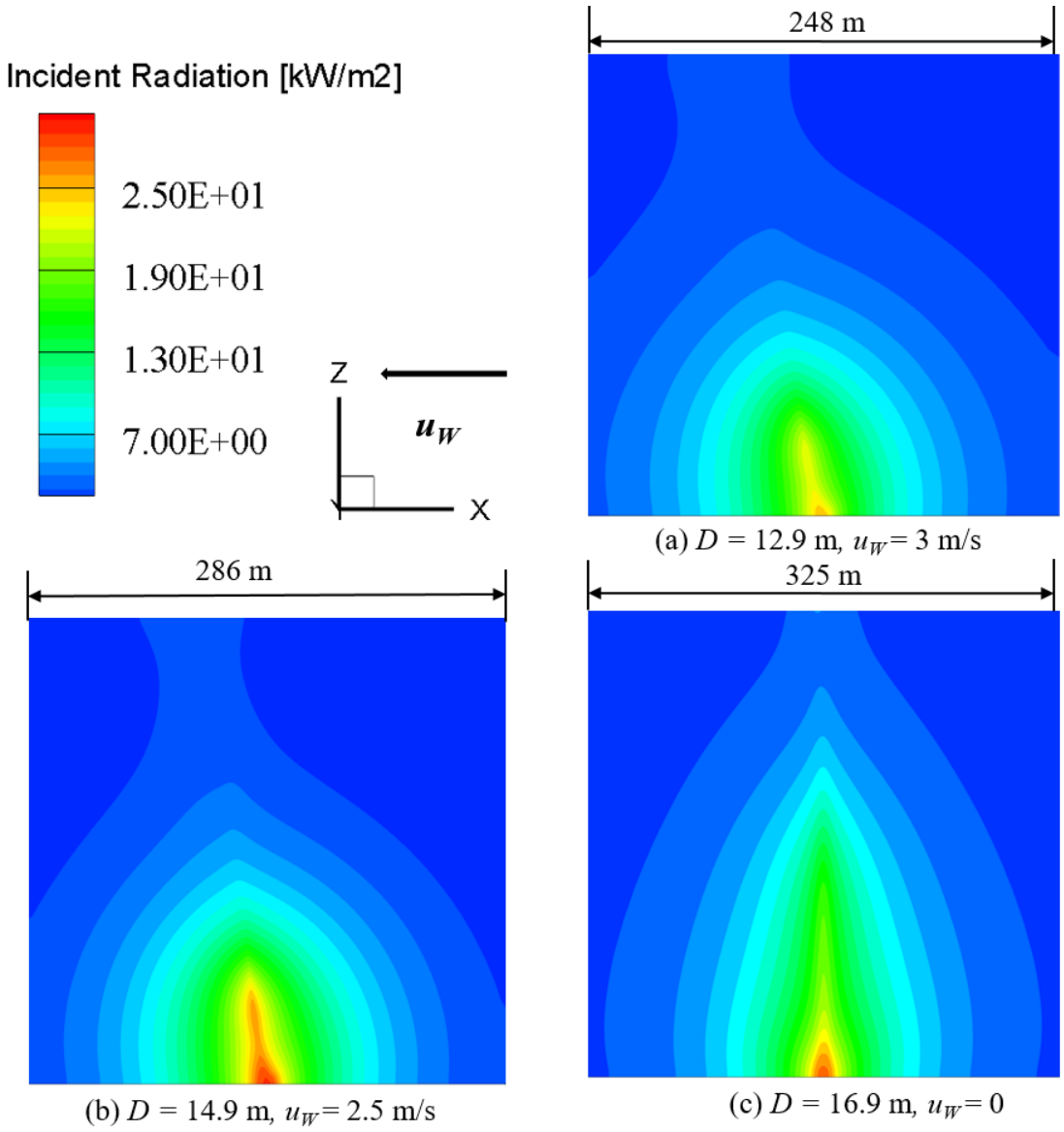

Figure 2.6 Incident radiation distributions at Y=0 of large LPG pool fires with different sizes and wind speeds: (a) D = 12.9 m, u_W = 3 m/s, (b) D = 14.9 m, u_W = 2.5 m/s, (c) D = 16.9 m, u_W = 0.

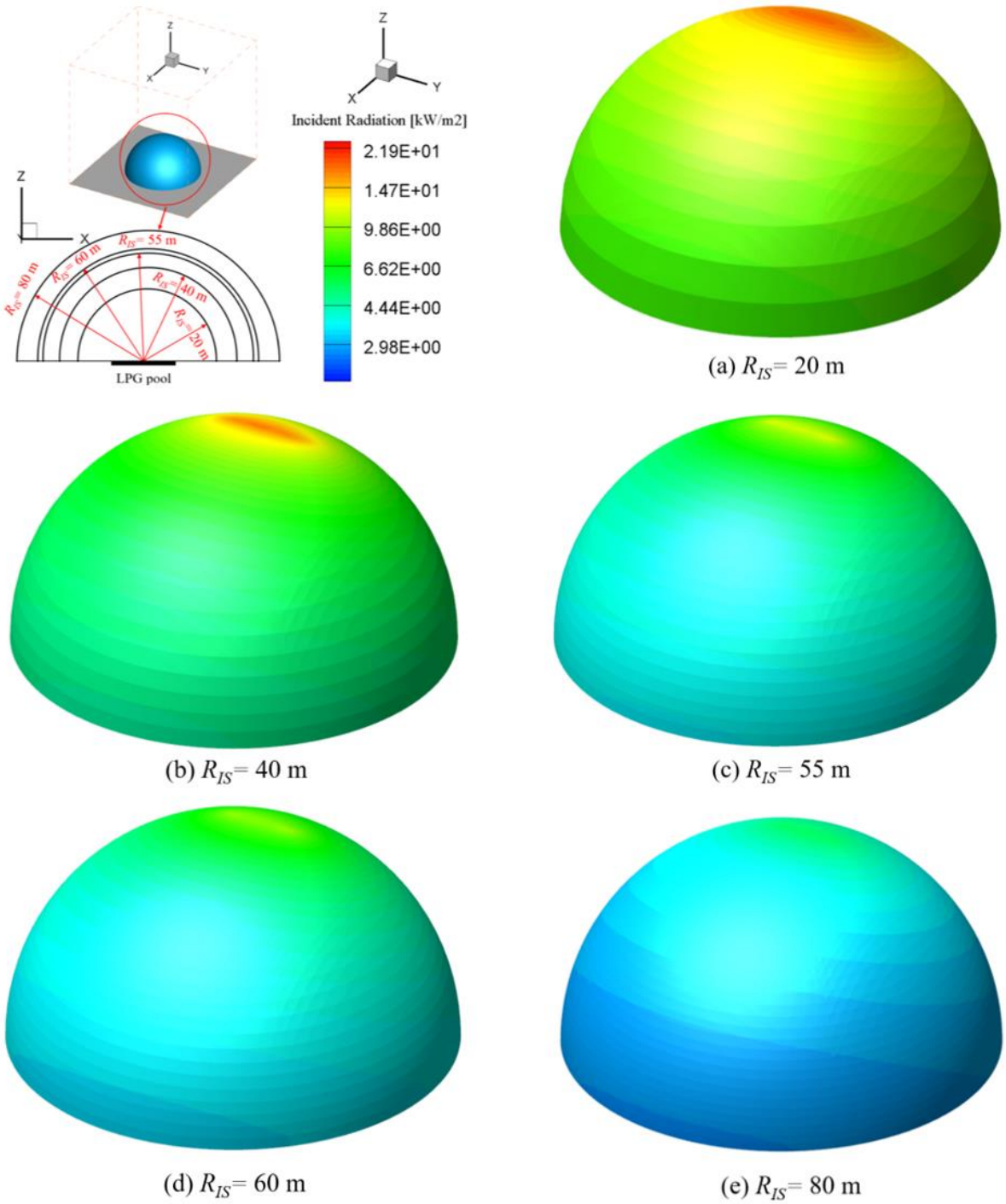

Figure 2.7 Iso-surfaces of incident radiation (kW/m^2) at different R_{IS} in LPG pool fire (D =12.9 m): (a) R_{IS} = 20 m, (b) R_{IS} = 40 m, (c) R_{IS} = 55 m, (d) R_{IS} = 60 m, (e) R_{IS} = 80 m.

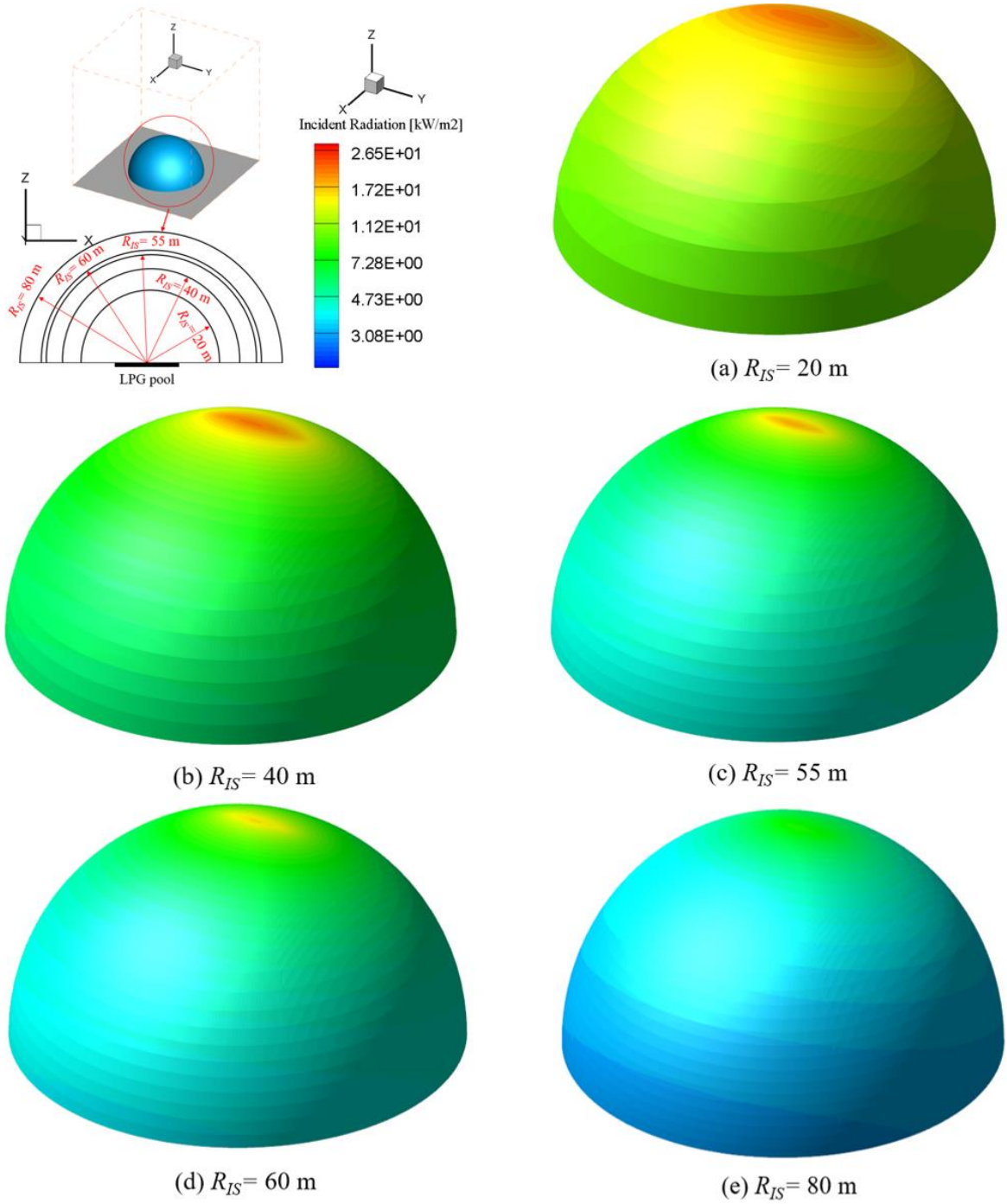

Figure 2.8 Iso-surfaces of incident radiation (kW/m^2) at different R_{IS} for LPG pool fire (D =14.9 m): (a) R_{IS} = 20 m, (b) R_{IS} = 40 m, (c) R_{IS} = 55 m, (d) R_{IS} = 60 m, (e) R_{IS} = 80 m.

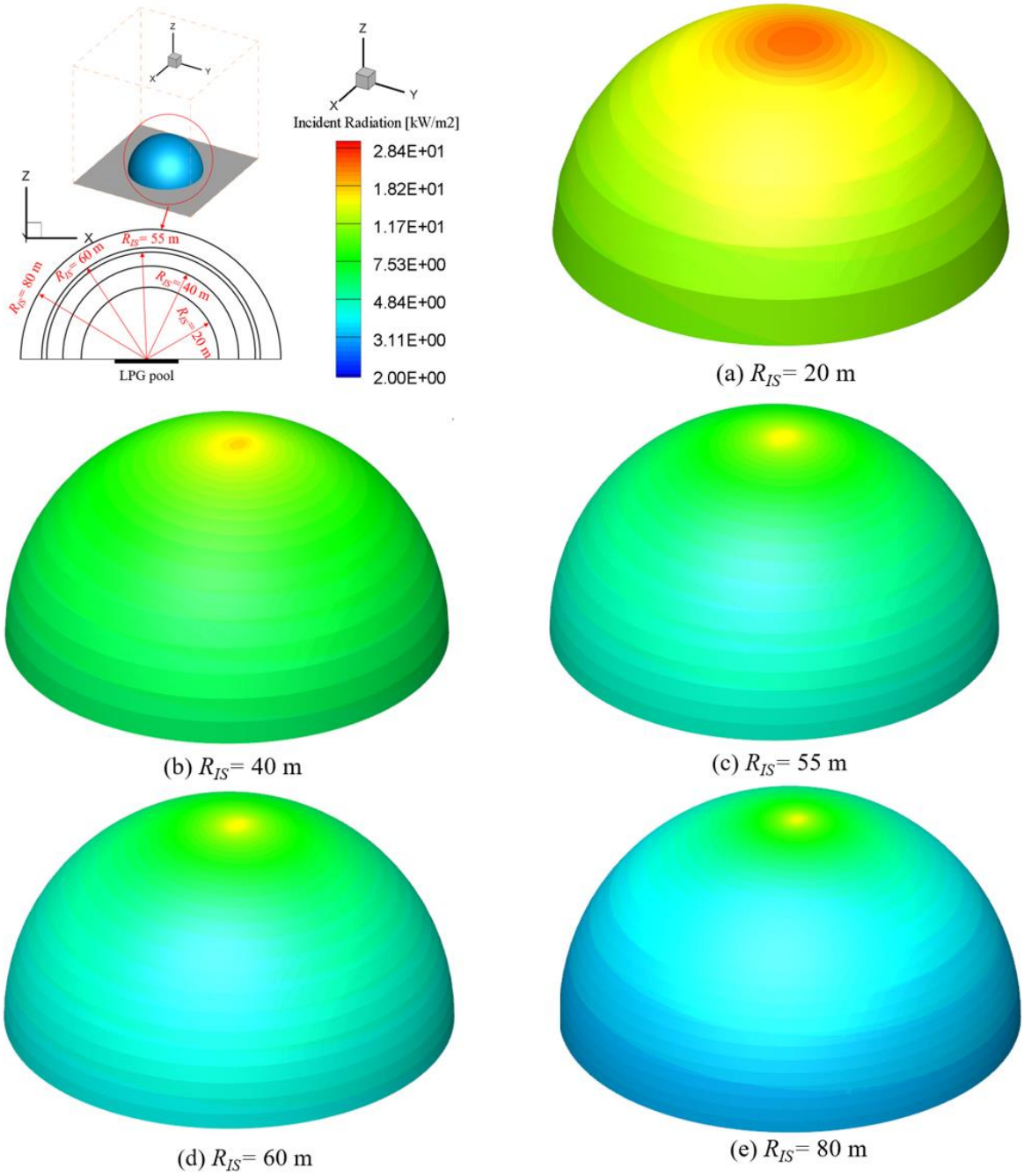

Figure 2.9 Iso-surfaces of incident radiation (kW/m^2) at different R_{IS} for LPG pool fire (D =16.9 m): (a) R_{IS} = 20 m, (b) R_{IS} = 40 m, (c) R_{IS} = 55 m, (d) R_{IS} = 60 m, (e) R_{IS} = 80 m.

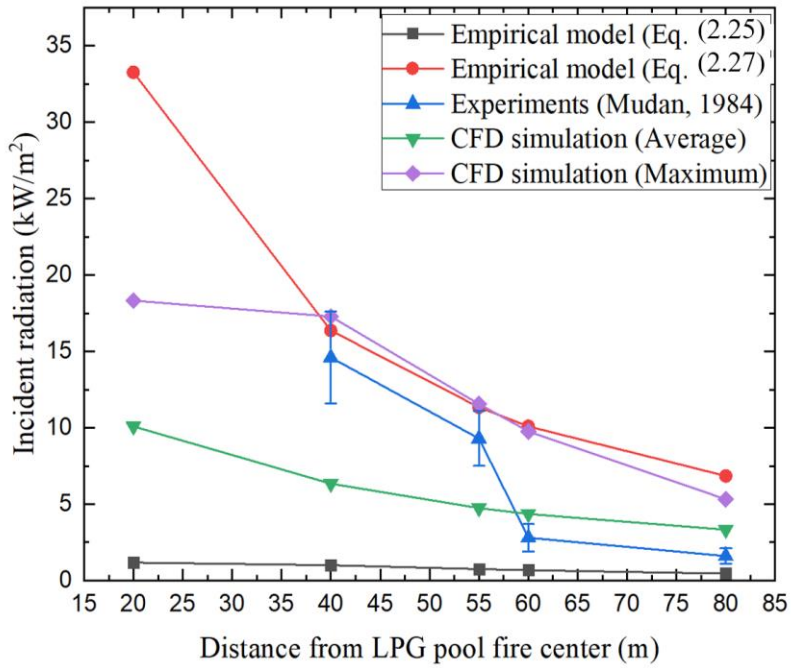

Figure 2.10 Comparison of incident radiation (kW/m^2) among empirical models, experimental data and CFD simulations in large LPG pool fires: D = 12.9 m, u_W = 3 m/s.

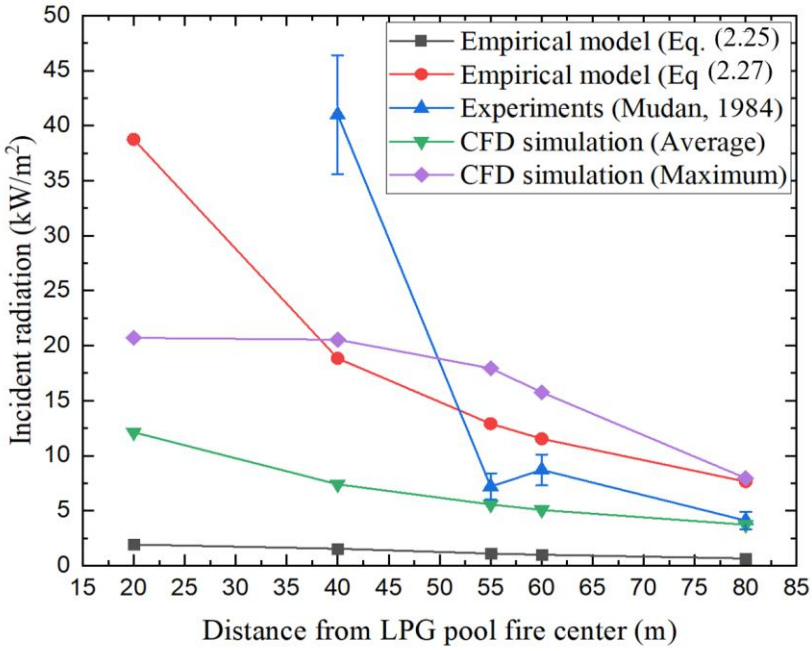

Figure 2.11 Comparison of incident radiation (kW/m^2) among empirical models, experimental data and CFD simulations in large LPG pool fires: D = 14.9 m, u_W = 2.5 m/s.

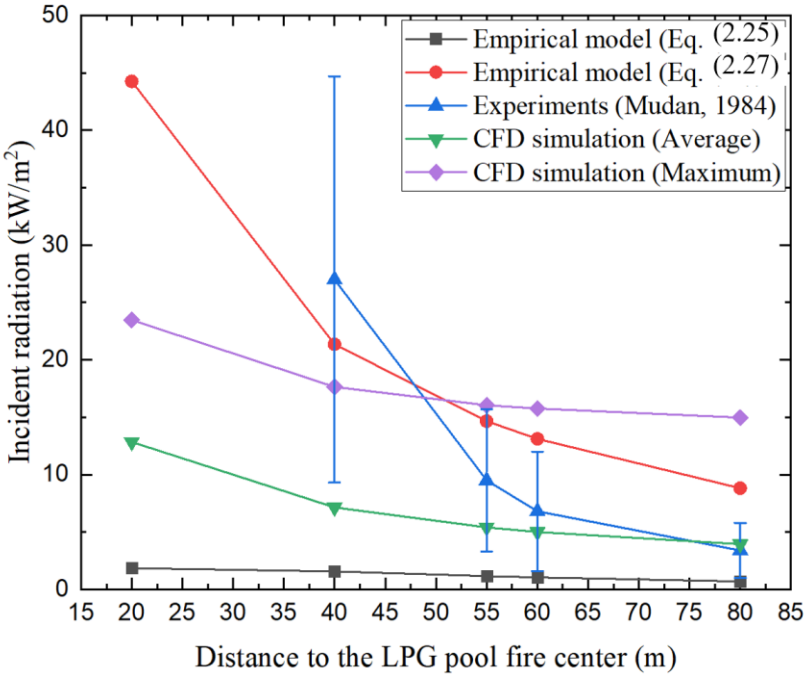

Figure 2.12 Comparison of incident radiation (kW/m^2) among empirical models, experimental data and CFD simulations in large LPG pool fires: D = 16.9 m, u_W = 0.

2.5.3 Safe Separation Distance

In Table 2.1, it shows that the maximum safe thermal exposure is 1.5 kW/m^2 to individuals in the unshielded area or urban area. While from Figures 2.6 to 2.12, it can be found that the minimum radiated heat flux is larger than 2 kW/m^2 in the simulated three LPG pool fires. Thus, the radiation from a longer distance (R_{IS} > 80 m) must be considered for appropriate safety distance estimation. Figures 2.10 to 2.12 show the maximum and average incident radiations from 20 m to 160 m for the three LPG pool fires. It can be observed that the maximum incident radiation for all pool fires is strongly influenced by the shape of fire flames (see Figures 2.4 and 2.5) because the wind speed can dominantly impact the flame morphologies. Average incident radiations share similar distributions from 20 m to 160 m around the pool fires. In contrast, the incident radiation distribution trends are different from the pool fire morphology when the ambient airflow field is static. The maximum incident radiation decreases slowly from 50 m to 100 m away from the center

of the pool fire with a diameter of 16.9 m, while the maximum radiated heat flux drops rapidly from 50 m to 100 m for the pool fires with the diameters of 12.9 m and 14.9 m which might be due to wind condition. Airflow conditions would have a significant impact on the fuel evaporation morphologies, which determine the shape of the fire flame. Moreover, the air velocity has a negligible effect on the distribution trend of the average incident radiation because the total energy generated by the pool fire is similar and determined by the fuel-burning rate.

Using the data and simulation results shown in Table 2.1 and Figure 2.13, the safe separation distances of LPG pool fires to the surrounded targets can be estimated. Large LPG pool fires tend to more likely happen in an outdoor environment rather than indoor area because only limited LPG is allowed to be utilized and stored in buildings and structures (NFPA, 2014), and the limited LPG is not available to form a large LPG pool. Indeed, the horizontal radiated heat flux draws more safety concerns than the vertical component due to the fact that individuals and facilities are often located on the ground around the pool fire accidents. Therefore, the average incident radiation was chosen as the more appropriate parameter to estimate safe separation distances than the maximum incident radiation, which is weighted more by the vertical radiation component.

Using the CFD simulation tool developed in this study, the estimated safe separation distances between LPG pool fires and targets for each code with corresponded pool fires are listed in Table 2.3. For the regulations and standards (49CFR, 2018; EN1473, 2016; NFPA, 2016), the upper limit of the thermal exposure is larger than 15 kW/m^2 for these objects, such as structures, concrete surface to adjacent storage tanks, mental surface to adjacent storage tanks, and outer surfaces of adjacent pressurized storage vessels. Thus, it is difficult to obtain the safe separation distances in these objects because the maximum predicted average radiation is only 12.85 kW/m^2. However, the safe separation distance can be less than 20.0 m, based on the fact that the maximum predicted average radiation is 12.85 kW/m^2 in the simulation results of this study. In contrast, the thermal

exposure limit is 1.5 kW/m^2 for the individuals wearing appropriate protections under continuous exposure conditions (49CFR, 2018) and the critical area (EN1473, 2016), such as an unshielded area of critical importance where people without protective clothing. Since the exposure limit (49CFR, 2018) is lower than the minimum average incident radiations predicted by the CFD simulation (2 kW/m^2), the safe separation distance determined by 49CFR (49CFR, 2018) and EN1473 (EN1473, 2016) should be farther than 120 m, 140 m, and 160 m for the LPG pool fires with the diameters of 12.9 m, 14.9 m, and 16.9 m, respectively. Generally, the specific safe separation distances for other codes can also be obtained using the CFD simulation data by following the similar analysis procedures mentioned above. Thus, the results from CFD simulation could provide valuable data for the code committees to evaluate the risks from large LPG pool fires.

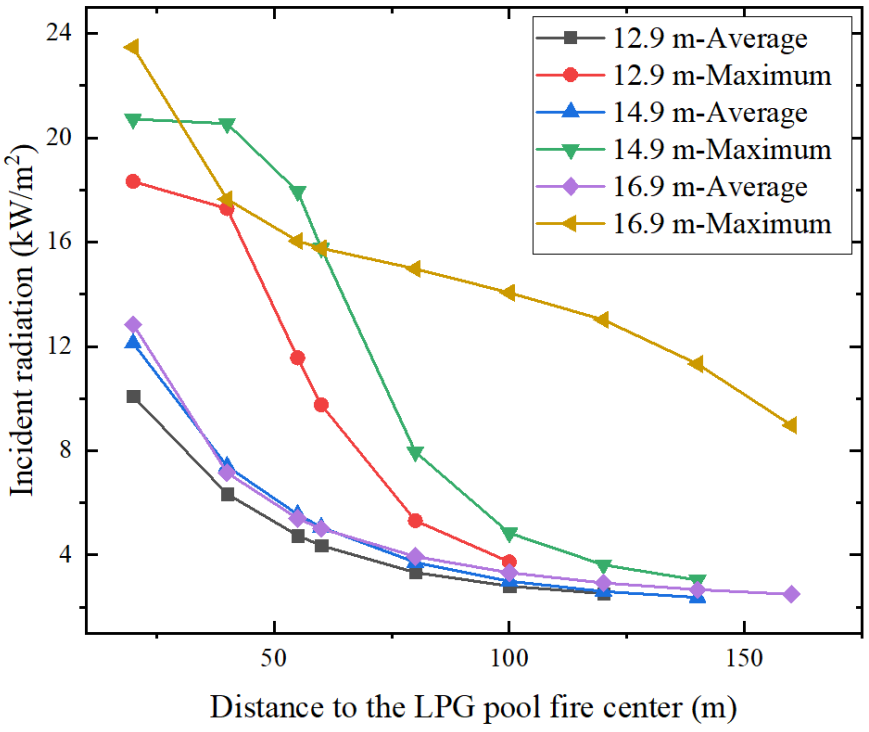

Figure 2.13 The maximum/average incident radiation predicted by CFD simulations for large LPG pool fires.

Table 2.3 Safe separation distances between large LPG pool fires and targets estimated using CFD simulations.

Standards/Regulations	Targets	Advised safe separation distance (m)		
		D = 12.9 m	*D* = 14.9 m	*D* = 16.9 m
NFPA 59A (NFPA, 2016)	Individuals	52.0	60.0	61.0
	Structures	< 20.0	< 20.0	< 20.0
API 521 (API-Standard521, 2014)	Individuals (Urgent emergency)	23.0	31.5	31.0
	Individuals (Action in 30s)	40.5	45.0	48.0
	Individuals (Action in 2 mins to 3 mins)	54.0	63.5	63.5
	Individuals (No action needed)	> 120.0	> 140.0	> 160.0
49 CFR (49CFR, 2018)	To ignite a design spill	52.0	60.0	60.0
	Individual's property	25.5	33.0	33.0
	An impounding area containing LNG	> 120.0	> 140.0	> 160.0
EN 1473 (EN1473, 2016)	Concrete surface to adjacent storage tanks	< 20.0	< 20.0	< 20.0
	Mental surface to adjacent storage tanks and outer surfaces of adjacent pressurized storage vessels	< 20.0	< 20.0	< 20.0
	Control rooms et al. and remote area	30.5	36.0	37.0
	Administrative buildings and other areas	52.0	60.0	61.0
	Critical area	> 120.0	> 140.0	> 160.0

2.6 Summary

In this study, a CFD model was developed to investigate the characteristics of large LPG pool fires by integrating the limited experimental tests. Simulation results were compared with existing experiments, and several conclusions can be obtained as follows:

- With the advantages of the P-1 radiation model and non-premixed combustion model, it is more reliable and accurate to describe the scenarios of large LPG pool fires than empirical correlations.
- Based on the empirical models and experimental data, a new correlation for SEP in LPG (100% propane) pool fire (10 m $\leq D \leq$ 20 m) has been proposed, which provides better prediction accuracies than existing models.
- CFD simulations show that the airflow conditions have less impact on maximum and average incident radiations to the surrounding individuals and structures, which are determined by the burning rate of LPG pool fires.
- The airflow condition can have significant impacts on the distribution of incident radiation in the same iso-surface, and it would tilt to wind direction because radiative heat flux distribution is determined by the flame configuration.
- Based on available results from CFD simulations, the safe separation distances have been suggested under the requirements of different codes.
- The incident radiation from CFD simulations can help us to have better understandings and estimations of the safe separation distances, which can address the concerns from related code committee members.

CHAPTER III

CONFIGURATION PREDICTIONS OF LARGE LIQUEFIED PETROLEUM GAS POOL FIRES USING A CFD METHOD

3.1 Introduction

The demand for liquefied petroleum gas (LPG) as a low-pollution fuel is increasing rapidly (Kojima, 2011) to achieve the goal of clean cooking and heating by 2030. Pool fire has the potential to occur if there is an LPG leakage during transportation or at storage sites. Thus, understanding the characteristics, i.e., the radiation and configuration of LPG pool fire, are necessary for the effective control of potential fire risks. Pool fire is defined as the combustion of material evaporating from a layer that is formed by a liquid fuel pool (Van den Bosch & Weterings, 1997). The liquid fuel spreads out horizontally and forms turbulent, non-premixed, and diffusive flame (Vela et al., 2009). A large-scale LPG pool fire, i.e., beyond the experimental scale available for study in laboratory or largest field tests, could lead to severe consequences and losses with high flame temperature and heat flux to its surroundings. Thus, studying the pool fire configurations is essential, which will provide direct evidence to predict the radiative heat flux accurately and evaluate the induced risks to the ambient environment (Yi et al., 2019). Experiments have been conducted to investigate the

flame height and wind effect on the configurations of LPG pool fires (Droste & Schoen, 1988; Hiroshi & Koseki, 2001a; Johnson et al., 1980; Palazzi & Fabiano, 2012). However, they focused on small-scale fires with pool diameters less than 10 m, and large-scale LPG pool fires have not been well investigated by experiments due to the high costs, measurement difficulties, and safety considerations (Arnaud Trouvé, 2008.; Vasanth et al., 2013). Nevertheless, there are many empirical or semi-empirical models, and correlations developed based on experimental data for the flame height and tilt of small-scale pool fires (A.G.A., 1974; Bariha, Srivastava Vimal, & Mishra Indra, 2017; Moorhouse, 1982; Sengupta, 2019; Steward, 1970a; P. H. Thomas, 1963; Welker & Sliepcevich, 1966a). These models may lead to significant errors when being applied to large-scale pool fires, which would have been discussed in the discussion section of this chapter. So far, there are no specific correlations for flame height and tilt in large LPG (100% propane) pool fires with diameters larger than 10 m. Thus, more reliable and accurate correlations for flame height and tilt should be developed to enhance the fundamental understanding of the large LPG pool fire configurations.

Since experimental investigations are complicated for large-scale LPG pool fires, computational fluid dynamics (CFD) models have been employed as an alternative time-saving and cost-effective tool based on first principles of physics and chemistry (Joshi et al., 2016; W. Wang et al., 2018; Z. Wang et al., 2016; Yi et al., 2019). The CFD capability to accurately simulate pool fires has been proved by previous studies. The early CFD effort to simulate fire dynamics was done by Galea (Galea, 1989), who used the field modeling approach to simulate enclosure fires. Sun et al. (Sun et al., 2014) used large eddy simulation (LES) to analyze the radiation from liquefied natural gas (LNG) pool fires and provided insight on determining the safe distance between LNG tanks and vaporizers. Vasanth et al. (Vasanth et al., 2015) showed good agreements between experimental measurements and CFD simulation results in flame temperature, radiation, and burning rates of multiple pool fires situated at differing elevations. Chow et al. (Chow, Dang, Gao, & Chow, 2017)

obtained flame height correlations, and thermal parameters in fire tornados using ANSYS Fluent (ANSYS Inc., Canonsburg, PA) validated via the comparison with experimental data. Therefore, it is feasible to employ CFD simulations to investigate the configuration properties of large LPG pool fires since it has been employed to investigate the heat radiation from large LPG pool fires successfully.

In this chapter, the characteristics of burning rate, flame height, and flame tilt of large LPG pool fires were investigated and compared using empirical models, correlations, and CFD simulations. Specifically, integrating the Re-Normalization Group (RNG) k-ε model, P-1 radiation model, and the non-premixed combustion (PDF) model, the CFD model was developed in ANSYS Fluent 2019 R2 (ANSYS Inc., Canonsburg, PA) to study the configuration of large LPG pool fires with pool diameters between 10 m and 20 m in static and windy conditions ($0 \leq u_w \leq 3$ m/s). The burning rates, flame heights, and tilts of large LPG pool fires using different methods are compared with the experimental data obtained by Mudan (K. S. Mudan, 1984). The work accomplished in Chapter III has been published in a peer-reviewed scientific journal (Yi, Feng, Park, & Wang, 2020).

3.2 Research Objectives

Employing the developed experimentally validated CFD model in Chapter I to predict the configuration of large LPG pool fires, several research objectives were listed as follows:

- Finding the best burning rate model for large LPG pool fire.
- Studying the effects of pool size and air velocity on the configuration prediction of large LPG pool fires.
- Developing more accurate correlations to calculate the flame height and flame tilt by integrating CFD simulations and previous correlations.

3.3 Theory

In large LPG pool fires, the radiative heat flux received by the surrounded objectives can be influenced by many variables, such as the pool size, the fire configuration (i.e., flame height and tilt), the duration of the fire, the distance to the ambient targets, and the characteristics of the targets exposed to the thermal radiation. The total radiative heat flux in a pool fire is determined by the burning rate, flame height, and flame tilt, which had significant impacts on radiation distributions when the point source model and solid flame model are used to estimate the heat flux to surrounded targets. Therefore, when predicting the radiation to ambient human and constructions around large LPG pool fires, the above-mentioned variables should be considered comprehensively. The details are discussed in the following.

3.3.1 Burning Rate Models

The burning rate varies mainly with the pool fire size and is also influenced by the ambient air velocity, i.e., the wind speed (Johnson et al., 1980). In general, the burning rate $\dot{m}$ of a pool fire can be expressed as:

$$\dot{m} = \frac{\pi \dot{m}'' D^2}{4} \tag{3.1}$$

and

$$\dot{m}'' = \rho_{LPG} v \tag{3.2}$$

where $\dot{m}$, $\dot{m}''$, and v are burning rates defined in mass, mass per unit area, and velocity, respectively (Drysdale, 2011).

Johnson et al. (Johnson et al., 1980) developed a correlation to describe the relationship between the burning rate v and pool diameter D based on the experimental data of small pool fires, which shows that the maximum burning rate v has been reached to 1.905×10^{-4} m/s when the pool size is larger than 0.508 m.

Blinov and Khudiakov (Blinov & Khudiakov, 1957) proposed that burning rates were determined dominantly by the heat flux from the fire plume to the liquid pool surface. Based on such a hypothesis, the following correlation was proposed by Hottel et al. (Hottel, 1959):

$$\dot{q}'' = k_1 \frac{T_F - T_B}{D} + k_2(T_F - T_B) + \sigma {T_F}^4 \cdot F(1 - e^{-k'D}) \tag{3.3}$$

It is worth mentioning that the first and second terms on the right-hand side of Eq. (3.3) represent conduction and convection, which can be neglected when the pool fire diameter is larger than 0.3 m (Drysdale, 2011; Zabetakis & Burgess, 1961). Being divided by the volumetric heat of vaporization $\rho_{LPG}\Delta H_v$ on both sides, Eq. (3.3) can be further simplified to

$$v = \frac{\sigma T_F^4 F}{\rho_{LPG}\Delta H_v}\,(1 - e^{-k'D}) \times 10^{-3} \tag{3.4}$$

To facilitate the calculation, the regression rate R (mm/min) was introduced by Blinov and Khudiakov (Blinov & Khudiakov, 1957). As a result, the LPG pool burning rate can be simplified and expressed as:

$$\dot{m}'' = \frac{\rho_{LPG} R}{60} \times 10^{-3} \tag{3.5}$$

and

$$R = R_\infty(1 - (\exp -k_1' D)) \tag{3.6}$$

Zabetakis and Burgess (Zabetakis & Burgess, 1961) recommended another equation to predict the burning rate per unit area $\dot{m}''$ of liquid pools when the pool diameter is greater than 0.2 m in the static air:

$$\dot{m}'' = \dot{m}''_\infty(1 - \exp(-k\beta D)) \tag{3.7}$$

For the liquid LPG (100% propane) used in Eq. (3.7) in this work, ρ_{LPG}, $\dot{m}''_{\infty}$, and $k\beta$ are considered as 585 kg/m^3, 0.099 kg/m·s, and 1.4 m^{-1} in this study, respectively (Vytenis Babrauskas, 1983).

In order to calculate the thermal radiation of pool fires directly, Liu et al. (Liu, Liang, & Huang, 2009) used a simplified equation to calculate the burning rate v:

$$v = \frac{(6.932 - 6.01^{\frac{-D}{1.31}})}{6} \times 10^{-4} \tag{3.8}$$

Since the regression rate *R* for LPG (100% propane) is still not available, and needs to be identified, the above-mentioned three models (Johnson et al., 1980; Liu et al., 2009; Zabetakis & Burgess, 1961) were employed to predict the burning rate of large LPG pool fires in this study, and all values have been converted to mass burning rate $\dot{m}$ shown in Figure 3.1 using Eq. (3.1) and Eq. (3.2).

3.3.2 Flame Height Models

The flame height is an important variable for the estimations of surface emissive power and radiation from large LPG pool fires to its surroundings when the point source model and solid flame model are employed. Many numerical models and correlations have been developed to predict the flame height for different hydrocarbon pool fires in the past decades, among which a dimensionless number H/D (Hurley et al., 2016) was often employed. The flame height model is usually proposed as a function of the Froude number Fr which is defined as (Drysdale, 2011):

$$Fr = \frac{U^2}{gD} \tag{3.9}$$

and

$$U = \frac{4\dot{Q}_C}{\pi \Delta H_C \rho_{LPG} D^2} \tag{3.10}$$

A dimensionless heat release rate, $\dot{Q}_C^*$, was introduced to classify fire types and flame height (B. McCaffrey, 1995; Zukoski, 1995) expressed by

$$\dot{Q}_C^* = \frac{\dot{Q}_C}{\rho_\infty c_p T_\infty \sqrt{gD} D^2} \tag{3.11}$$

Based on Eq. (3.11), Thomas (P. H. Thomas, 1963) further developed a correlation for the mean visible height of turbulent diffusion flames in still air:

$$H/D = 42\left(\frac{\dot{m}''}{\rho_a\sqrt{gD}}\right)^{0.61} \tag{3.12}$$

Steward (Steward, 1970a) developed a similar correlation with a dimensionless parameter of inverse volumetric expansion ratio due to combustion expressed by:

$$H/D = 14.73\left(\frac{\omega(r+\frac{\omega}{\rho'_{LPG}})}{(1-\omega)^5}\right)\left(\frac{\dot{m}''}{\rho_a\sqrt{gD}}\right)^{0.4} \tag{3.13}$$

and

$$\rho'_{LPG} = \frac{\rho_{LPG}\, g}{\rho_a} \tag{3.14}$$

ω is determined using the equation:

$$\omega = \frac{\varphi - \varphi_{st}}{\alpha(1-\varphi_{st})} \tag{3.15}$$

where α is considered as 8 for hydrocarbons (Tugnoli, Salzano, Di Benedetto, Russo, & Cozzani, 2013), φ is the mole fraction composition of the fuel-air mixture and φ_{st} is the stoichiometric mole fraction composition fraction for the fuel-air mixture.

Specifically, since the composition of LPG in the United States is pure propane (Hahn, 2019), the evaporated fuel cloud in this study can be considered as pure propane in the vapor phase. Therefore,

parameter values for pure propane were used. For example, ω is equal to $\frac{1}{9}$ (Mannan, 2012), and r is equal to 15.6. Using Eqs. (3.13) to (3.15), a new correlation which focuses on the flame height of LPG pool fires is proposed as follows:

$$H/D = 46.24\left(\frac{\dot{m}''}{\rho_a\sqrt{gD}}\right)^{0.4} \tag{3.16}$$

Based on previous correlations and experimental results (Heskestad, 1981; G. Heskestad, 1983), Heskestad (Gunnar Heskestad, 1983) has obtained the following correlation:

$$H/D = 15.6\left(\left(\frac{c_pT_\infty}{g\rho_\infty^2(\Delta H_c/r)^3}\right)\frac{\dot{Q}_c{}^2}{D^5}\right)^{1/5} - 1.02 \tag{3.17}$$

McCaffery (B. McCaffrey, 1995) further simplified Eq. (3.17) in terms of $\dot{Q}_C^*$. Specifically, when $0.12 < \dot{Q}_C^* < 1.2 \times 10^4$, Eq. (3.17) can be rewritten as:

$$H/D = 3.7\dot{Q}_C^{*\,2/5} - 1.02 \tag{3.18}$$

Besides, the presence of wind may also alter the visible length of flames when the wind velocity is large enough. The correlation developed by Thomas (P. H. Thomas, 1963) explicitly shows the wind effect on the wood crib flames:

$$H/D = 55\left(\dot{m}''/\rho_a\sqrt{gD}\right)^{0.67}(u^*)^{-0.21} \tag{3.19}$$

where u^* is the nondimensionalized wind velocity defined by

$$u^* = u_w/\left(\frac{g\dot{m}''D}{\rho_{LPG}\,g}\right)^{\frac{1}{3}} \tag{3.20}$$

Moorhouse (Moorhouse, 1982) conducted several large-scale experiments for LNG pool fires. The crosswind and downwind were analyzed to determine the exact flame length, and the correlated flame height expressed by

$$H/D = 6.2\left(\dot{m}''/\rho_a\sqrt{gD}\right)^{0.254}(u_{10}^*)^{-0.044} \quad (3.21)$$

In Eq. (3.19), u^* is treated to be equal to 1.0 when it is less than 1.0 (Krishna S. Mudan, 1984). Since Eq. (3.21) is used to estimate LNG pool fires under the windy condition, the correlations for large LPG pool fires can be refined based on Eq. (3.21) by using CFD simulations.

In this study, Eqs. (3.12), (3.13), (3.16), (3.17), and (3.18) were employed to predict the flame height in static ambient air for large LPG pool fires. Equations (3.19) and (3.21) are used to estimate flame heights with ambient winds. It should be noticed that Eq. (3.16) was originally developed in this study, specifically for LPG (100% propane) pool fires. In contrast, other correlations mentioned above are for other hydrocarbon fuels, which might lead to errors to predict flame heights of LPG pool fires.

3.3.3 Flame Tilt Models

The ambient airflow dynamics can have a significant impact on the flame in outdoor environments, which may affect the fire behaviors tremendously. The tilt angle, θ, is often used to describe the

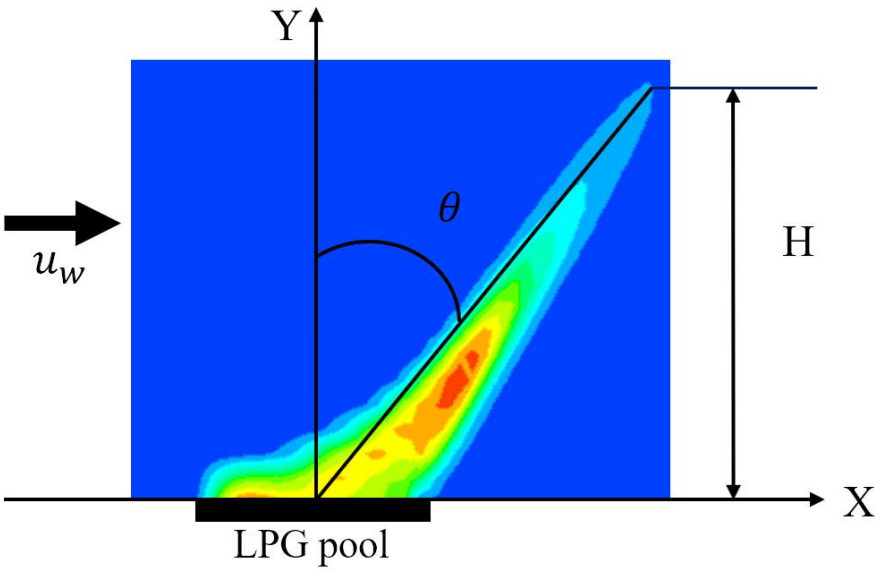

Figure 3.1 Definition of the flame height *H* and flame tilt angle θ.

effect of cross-winds on the flame (Oka, Sugawa, Imamura, & Matsubara, 2003), which is defined by the angle formed by the straight line between the center of the burner surface and the intersection of the flame axis (see Figure 3.1).

In order to have a better understanding of the wind effect on flame height in LPG pool fires, Oka et al. (Oka et al., 2003) proposed an equation for predicting the flame tilt angle ($20° \leq \theta \leq 80^{\circ}$) for rectangular shape pools as a function of multiple variables, i.e.,

$$tan\theta = \begin{cases} 2.73F_r^{0.4}Q_c^{*-0.55}\left(\frac{W}{r^*}\right)^{-0.5}, & (0.05 < Q_c^* \leq 0.38) \quad (3.22a) \\ 2.73F_r^{0.4}Q_c^{*-0.267}\left(\frac{W}{r^*}\right)^{-0.5}, & (0.38 < Q_c^* < 12.8) \quad (3.22b) \end{cases}$$

where W is the long side length of a rectangular pool, and r^* is the equivalent radius of the pool fire, which is defined by

$$r^* = \sqrt{A/\pi} \quad (3.23)$$

For LPG pool fires in circular shapes, Eqs. (3.22 (a) & (b)) (Oka et al., 2003) can be simplified as follows:

$$tan\theta = \begin{cases} 2.18F_r^{0.4}Q_c^{*-0.55}, & (0.05 < Q_c^* \leq 0.38) \quad (3.24a) \\ 2.18F_r^{0.4}Q_c^{*-0.267}, & (0.38 < Q_c^* < 12.8) \quad (3.24b) \end{cases}$$

Additionally, an empirical correlation characterizing the wind speed effect on pool fire flame has been proposed by Rew et al. (Rew, Hulbert, & Deaves, 1996):

$$\frac{tan\,\theta}{cos\,\theta} = 3.13F_r^{0.2155} \quad (3.25)$$

Comparing different models, including correlations mentioned by Mudan (Krishna S. Mudan, 1984) with experimental data of pool fires, Fay (Fay, 2006) developed the best correlation for wind tilt, which can be expressed as:

$$sin\,\theta = \frac{F_r^2}{F_r^2 + 0.19} \tag{3.26}$$

Welker and Sliepcevich (Welker & Sliepcevich, 1966a) proposed another correlation based on small-scale liquid pool fire experiments, which is shown as follows:

$$\frac{tan\theta}{cos\theta} = 3.3\left(\frac{Du_w}{\nu}\right)^{0.07}(F_r)^{0.8}\left(\frac{\rho_{LPG}g}{\rho_a}\right)^{-0.6} \tag{3.27}$$

Another correlation for flame tilt was derived (P. H. Thomas, 1963), based on the tests from wood cribs:

$$cos\theta = 0.7\left(\frac{u_w}{(g\dot{m}''/\rho_a)^{1/3}}\right)^{-0.49} \tag{3.28}$$

Moreover, A.G.A. (A.G.A., 1974) concluded a correlation using experimental data to determine the angle of tilt:

$$cos\theta = \begin{cases} 1, & (u^* < 1) \quad (3.29a) \\ \frac{1}{\sqrt{u^*}}, & (u^* \geq 1) \quad (3.29b) \end{cases}$$

A global correlation was developed by Tang et al. (Tang, Li, Zhu, Qiu, & Tao, 2015) to characterize the burning behaviors of acetone pool fire under crosswind ranging from 0 to 2.5 m/s shown as follows:

$$tan\theta = 4.16\left(\frac{\rho_a c_p(T_F - T_a){u_w}^5}{\dot{m}''D^2\Delta H_c}\left(\frac{T_a}{g(T_F - T_a)}\right)^2\right)^{0.2} \tag{3.30}$$

More recently, Hu et al. (L. Hu, Liu, de Ris, & Wu, 2013) used another correlation to describe the tilt angle for n-heptane and ethanol pool fires in terms of the ratio of the cross-flow air velocity and the uprising velocity of the buoyancy-induced flame:

$$tan\theta = 9.1\left(\frac{\rho_a c_p(T_F - T_a){u_w}^5}{\dot{m}''D^2\Delta H_c}\left(\frac{T_a}{g(T_F - T_a)}\right)^2\right)^{0.2} \tag{3.31}$$

3.2.4 Governing Equations

The conservation laws of mass, energy, momentum, as well as constitutive equations of chemical kinetics, RNG k-ε turbulence model, P-1 radiation model, and non-premixed combustion model consist of the closed equation system for the CFD simulations, which are described in detail in Chapter II and previous publications (Yi et al., 2019).

3.4 Numerical Method

3.4.1 Geometry and Mesh

A 3-D computational domain for a large LPG pool fire at the center was constructed, with a pool

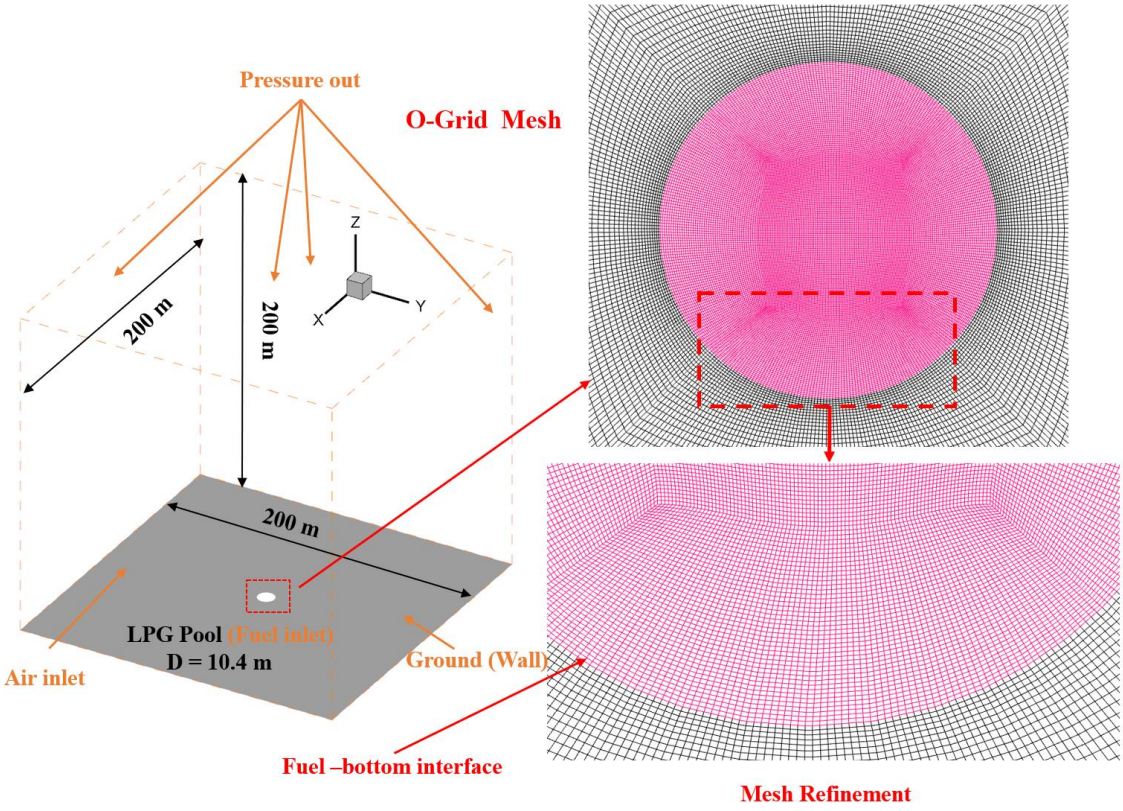

Figure 3.2 Flow domain and the structured hexahedral final mesh for LPG pool fire simulations (D = 10.4 m and $\dot{m}$ = 8.406 kg/s).

diameter of 10.4 m (see Figure 3.2). O-Grid meshes were generated for the cylindrical flame region using ICEM CFD 2019 R2 (ANSYS Inc., Canonsburg, PA). To optimize the balance between

computational accuracy and efficiency, a mesh independence test was performed among four meshes with different element sizes (see Chapter II) (Yi et al., 2019). The final structured hexahedral mesh contains 3,694,764 cells. To eliminate the pool-size effect, the meshes have been scaled with factors 1.240, 1.433, and 1.625 for the pools with 12.9 m, 14.9 m, and 16.9 m in diameters, respectively.

3.4.2 Numerical Setup

A total of 19 CFD simulation cases were performed to study the configuration characteristics of large LPG pool fires. Specifically, three cases were used to seek for the best burning rare model as a function of pool diameter for large LPG pool fires, and another sixteen cases investigated how flame height and tilt can be influenced by the pool diameter (10 m $\leq D \leq$ 20 m) and wind velocity ($0 \leq u_w \leq 3.0$ m/s). The distinguished temperature for flames from the black smoke zone was considered as 800 K (Hägglund & Persson, 1976; Yi et al., 2019). The LPG pool fire simulations are considered steady-state in this study. A user-customized, commercial volume-finite based computer program, i.e., ANSYS Fluent 2019 R2 (ANSYS Inc., Canonsburg, PA) was employed to perform numerical solutions of the given governing equations (see Section 3.4.1) (Yi et al., 2019) with appropriate boundary conditions (see Table 3.1). Boundary conditions were determined based on empirical models and experimental measurements (K. S. Mudan, 1984) shown in Table 3.1. Simulations were run on a local 64-bit Dell Precision Tower 7810 with 128GB of RAM and dual 3.40 GHz processors. Second-order upwind schemes were adopted to discretize the governing equations of mass, momentum, turbulent kinetic energy, turbulent dissipation rate, energy, mean mixture fraction, and mixture fraction variance. The coupled scheme was employed for pressure-velocity coupling, and the least-squares cell-based schemes were applied for spatial discretizations. 1.0E-6 was assigned as the convergence criteria for energy and P1, and 1.0E-3 for the rest equations.

Table 3.1 Boundary conditions employed in CFD simulations for large LPG pool fires

<table>
<tr><td rowspan="3"></td><td rowspan="3">Pool diameter (m)</td><td rowspan="3">Ambient temperature (K)</td><td rowspan="3">Average mass burning rate $\dot{m}$ (kg/s)</td><td colspan="6">Faces</td></tr>
<tr><td>X+</td><td>X-</td><td>Y+</td><td>Y-</td><td>Z+</td><td rowspan="2">Z-</td></tr>
<tr><td>Air velocity u_w (m/s)</td><td colspan="4">Pressure outlet</td></tr>
<tr><td rowspan="3">Finding the best burning rate</td><td rowspan="3">16.9</td><td rowspan="3">312</td><td>14.972</td><td rowspan="3">0</td><td rowspan="15" colspan="4">Gauge pressure = 0</td><td rowspan="15">Non-slip wall</td></tr>
<tr><td>22.196</td></tr>
<tr><td>24.986</td></tr>
<tr><td rowspan="12">Flame heights and tilts simulations</td><td rowspan="4">10.4</td><td rowspan="4">306</td><td rowspan="4">8.406</td><td>0</td></tr>
<tr><td>0.5</td></tr>
<tr><td>2.5</td></tr>
<tr><td>3</td></tr>
<tr><td rowspan="4">12.9</td><td rowspan="4">309</td><td rowspan="4">12.932</td><td>0</td></tr>
<tr><td>0.5</td></tr>
<tr><td>2.5</td></tr>
<tr><td>3</td></tr>
<tr><td rowspan="4">14.9</td><td rowspan="4">306</td><td rowspan="4">17.254</td><td>0</td></tr>
<tr><td>0.5</td></tr>
<tr><td>2.5</td></tr>
<tr><td>3</td></tr>
<tr><td rowspan="4">16.9</td><td rowspan="4">312</td><td rowspan="4">22.196</td><td>0</td></tr>
<tr><td>0.5</td></tr>
<tr><td>2.5</td></tr>
<tr><td>3</td></tr>
</table>

3.5 Results and Discussion

3.5.1 Comparisons of Predicted Flame Heights to Find the Best Burning Rate Model

Although the experimental data are well documented in a benchmark research report for LPG pool fires with different diameters (K. S. Mudan, 1984), the burning time of these pool fires in the experiments was not recorded precisely. Due to lack of the burning duration data in the experiments, it is impossible to estimate the average mass burning rate accurately with the only given information of total LPG burned mass. Since the burning rate is a key boundary condition for CFD simulations, which determines the accuracy of flame height and tilt angle predictions for large LPG pool fires, three widely used burning rate models were employed (see Section 3.3.1 and Figure 3.3) in CFD simulations. To find the most accurate burning rate model for large LPG pool fire simulations, comparisons of the predicted flame heights using different burning models has been done with the benchmark experimental measurements (K. S. Mudan, 1984) (see Figures. 3.4(a) to (c)).

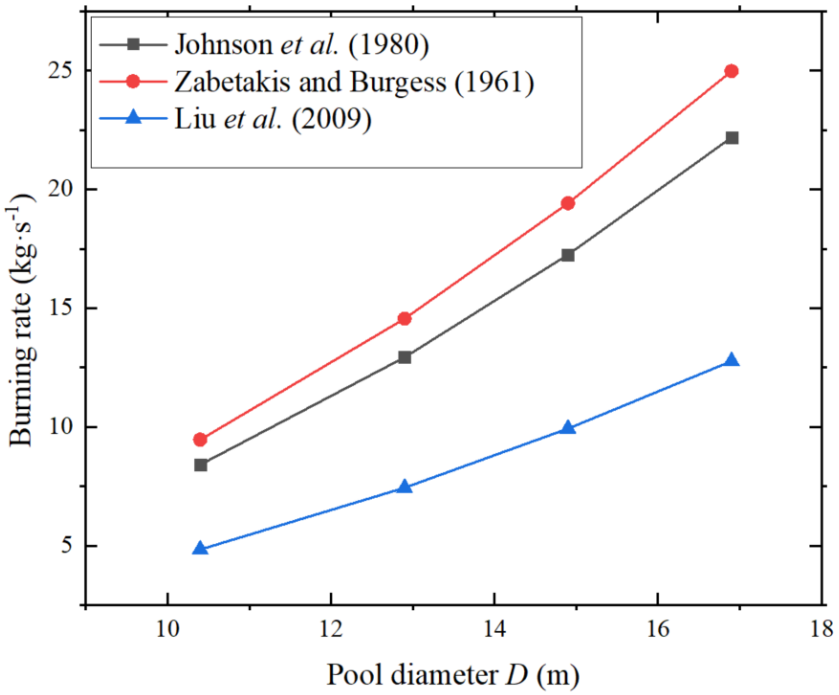

Figure 3.3 Relationships between burning rates $\dot{m}$ and pool diameters (10.4 m $\leq D \leq$ 16.9 m) with three different models in large LPG pool fires.

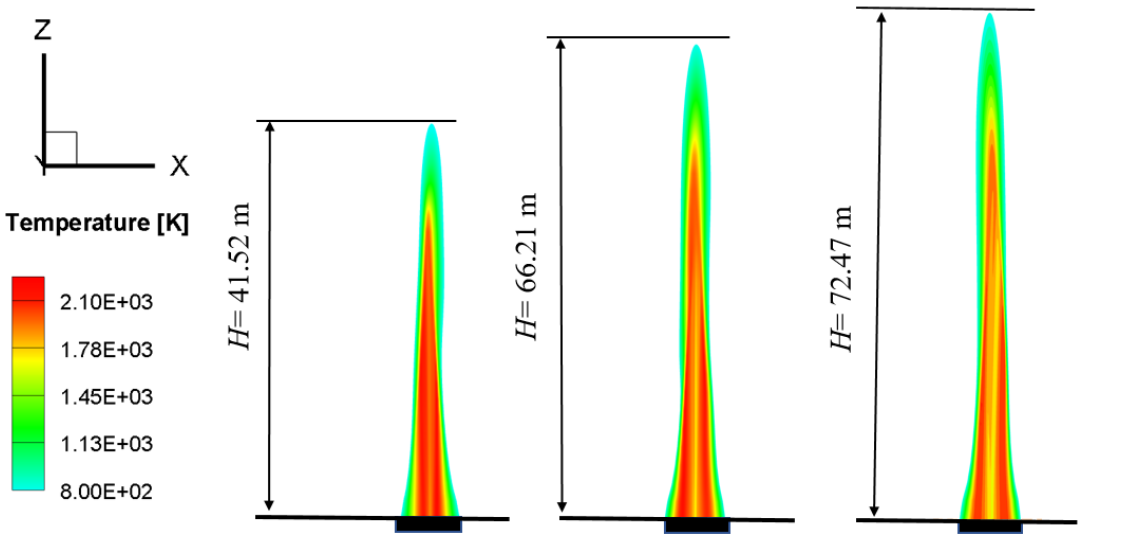

Figure 3.4 Predicted flame configurations of large LPG pool fires (D = 16.9 m, u_w = 0) colored by temperature (K) using three different burning rates: (a) $\dot{m}$ = 12.770 kg/s (Liu et al., 2009), (b) $\dot{m}$ = 22.196 kg/s (Johnson et al., 1980), (c) $\dot{m}$ = 24.986 kg/s (Zabetakis & Burgess, 1961).

Specifically, according to the previous study (Yi et al., 2019), flame height is majorly determined by the burning rates in static air for large LPG pool fires. Therefore, CFD simulations for the pool fire with D =16.9 m in static air were performed using the three burning rate models (see Figure 3.3). The configurations of the flames colored by temperature are shown in Figure 3.4. Figures 3.4 (a) to (c) show three different flame heights, i.e., 41.52 m, 66.21 m, and 72.47 m, corresponding to three burning rate models. Experimental measurements (K. S. Mudan, 1984) show that the flame height for the same large LPG pool fire with the diameter 16.9 m is 54 m. Thus, it can be found that the flame height predicted in Figure 3.4 (b) using Johnson's burning rate model (Johnson et al., 1980) provides the best match to experiments. The flame height with a burning rate of 12.770 kg/s is smaller than a regular LPG pool fire (K. S. Mudan, 1984), which implies that the burning rate in a regular LPG pool fire should be larger than 12.770 kg/s. The temperature profile is more likely a

jet fire rather than a pool fire when the burning rate is 24.986 kg/s because the flame height is 34 % higher than a normal LPG pool fire (K. S. Mudan, 1984; Krishna S. Mudan, 1984). Therefore, to reduce the relative errors between the CFD simulations and experiments, the burning rate model proposed by Johnson et al. (Johnson et al., 1980) was selected as the boundary conditions values in CFD simulations to predict the flame heights and tilts in large LPG pool fires. Moreover, the parametric analysis of between flame height and pool diameter (see Figures 3.5 to 3.12 and Table 3.2 in Section 3.5.2) also indicate that Johnson's burning rate model is more precise and reliable in flame height predictions in large LPG pool fires compared with experimental data.

3.5.2 Flame Height *vs.* Pool Diameter and Wind Velocity

According to the experimental report (K. S. Mudan, 1984), the flame heights were 54.9 m, 51.9 m and 54.4 m in the LPG pool fires with the corresponding diameters of 12.9 m, 14.9 m and 16.9 m under different wind velocities ($0 \leq u_w \leq 3$ m/s), respectively. To obtain the flame heights with different pool diameters and wind velocities, the flame heights covered by the temperature magnitude with corresponded pool sizes (10.4 m $\leq D \leq$ 16.9 m) under the air velocity from 0 to 3 m/s have been simulated using the CFD model and visualized in Figures 3.5 to 3.8. Table 3.2 also quantitatively summarized how the flame height varies with the change of pool diameter at different wind velocities. It can be found that the flame height increases gradually as the burning rate grows up under the same air condition. These phenomena can be explained that the larger burning rate would generate more LPG vapor by the vaporization heat from the fire plume, and eventually form higher flames during the combustion process. Figures 3.5 to 3.12 indicate that the flame height decreases with the increase in wind velocity, because higher wind velocity will enhance the vaporization of fuel gases and the tilt angle of the flame, resulting in the flame axis more leaned towards the horizontal direction.

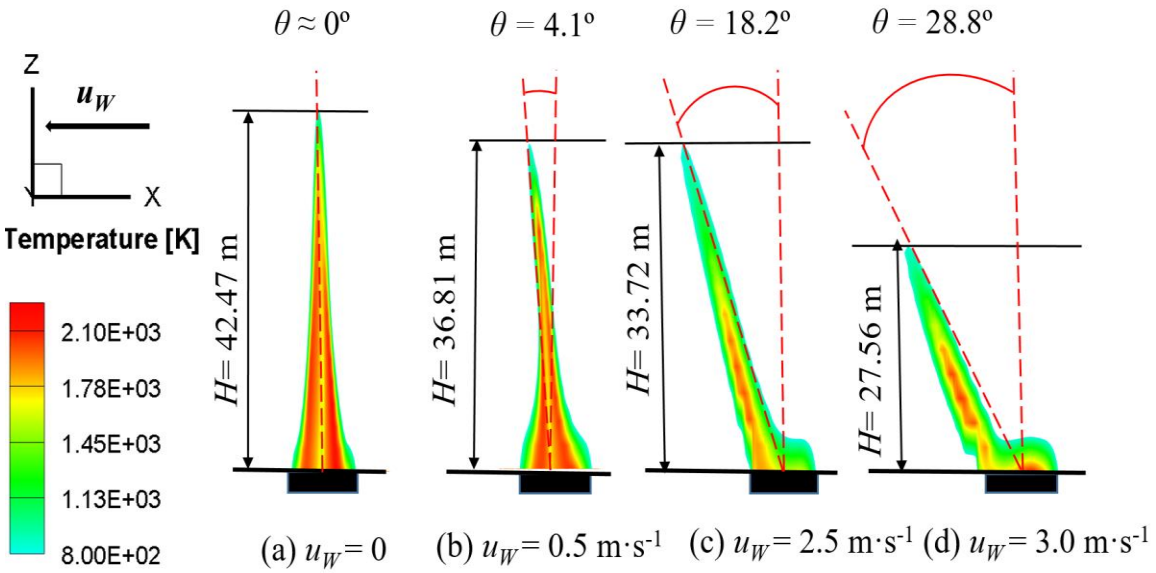

Figure 3.5 Temperature (K) profiles of large LPG pool fires (D = 10.4 m) with different wind velocities: (a) u_w = 0, (b) u_w = 0.5 m/s, (c) u_w= 2.5 m/s, (d) u_w = 3 m/s.

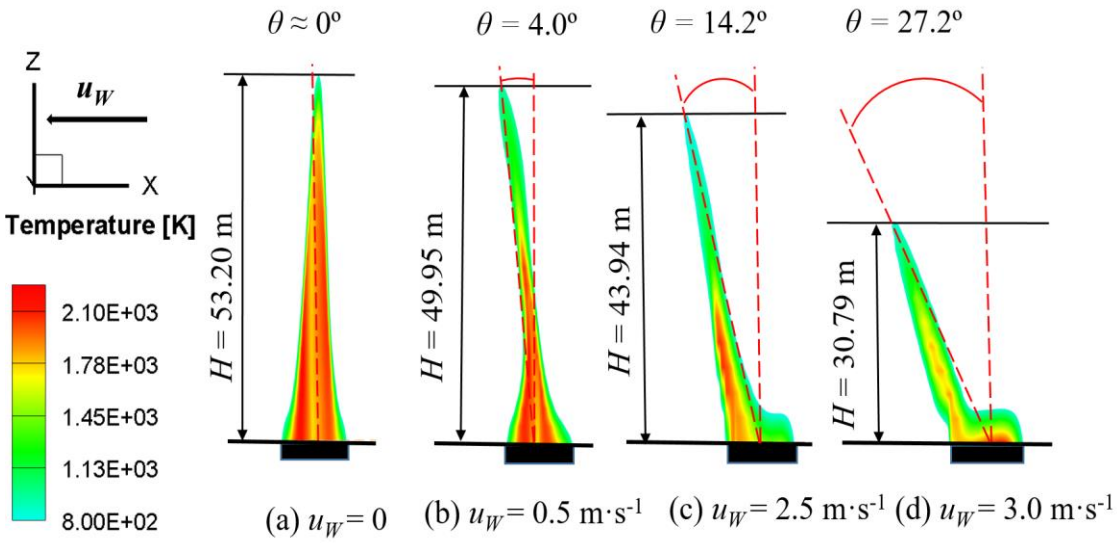

Figure 3.6 Temperature (K) profiles of large LPG pool fires (D = 12.9 m) with different wind velocities: (a) u_w = 0, (b) u_w = 0.5 m/s, (c) u_w= 2.5 m/s, (d) u_w = 3 m/s.

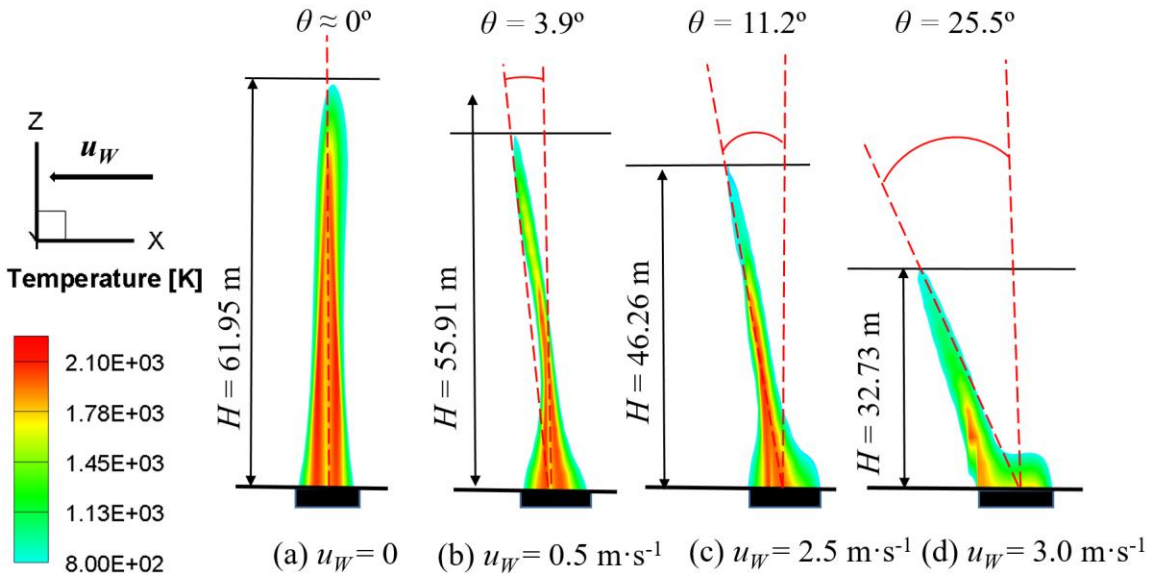

Figure 3.7 Temperature (K) profiles of large LPG pool fires (D = 14.9 m) with different wind velocities: (a) uw = 0, (b) uw = 0.5 m/s, (c) uw= 2.5 m/s, (d) uw = 3 m/s.

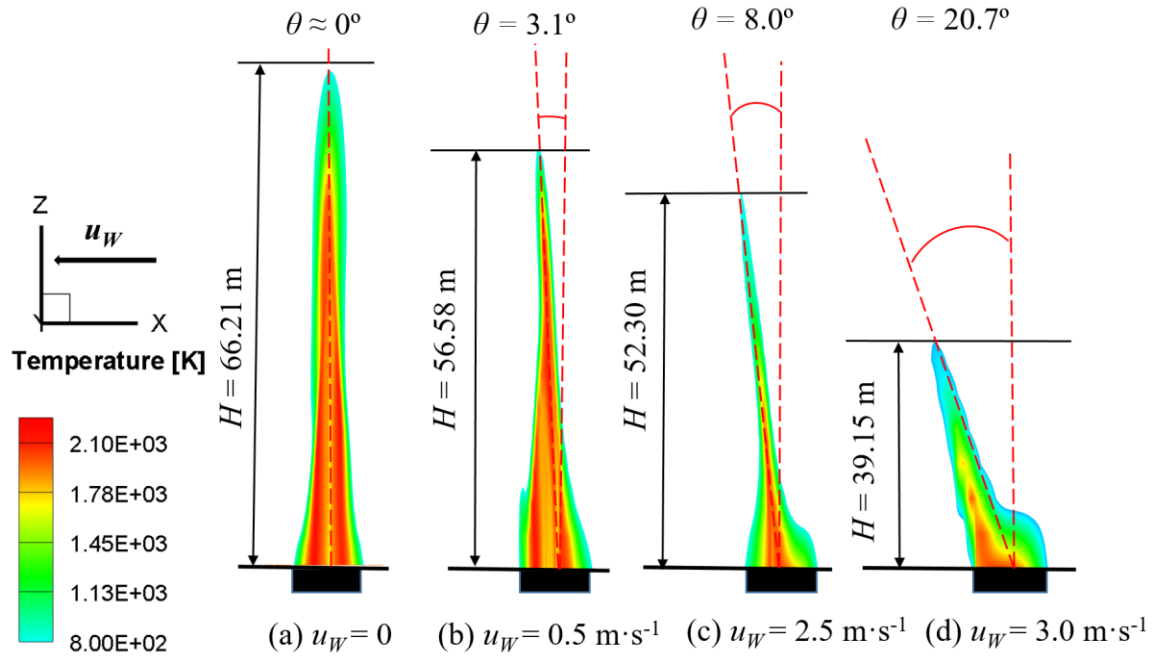

Figure 3.8 Temperature (K) profiles of large LPG pool fires (D = 16.9 m) with different wind velocities: (a) u_w = 0, (b) u_w = 0.5 m/s, (c) u_w= 2.5 m/s, (d) u_w = 3 m/s.

Table 3.2. Flame heights (m) for pool fires with different pool diameters (m) and wind velocities (m/s)

	D =10.4	D =12.9	D =14.9	D =16.9
u_w = 0.0	42.47	36.81	33.72	27.56
u_w = 0.5	53.20	49.95	43.94	30.79
u_w= 2.5	61.95	55.91	46.26	32.73
u_w = 3.0	66.21	56.58	52.30	39.15

The comparisons of flame heights using empirical models, correlations, the only available experimental data (K. S. Mudan, 1984), and the CFD simulations in this study are shown in Figures. 9 to 3.12. Equations (3.12), (3.16), (3.17), and (3.18) have been used to estimate the flame height in the still air, which are shown in Figures 3.9 to 3.12. Compared with the flame heights predicted via the experimentally optimized and validated CFD model (see Section 3.5.1) as well as the experimental data, Eqs. (3.12), (3.17) and (3.18) underestimate the flame heights with noticeable errors. The deviations are due to the fact that Eqs. (3.12), (3.17) and (3.18) were developed specifically for small pool fires or other hydrocarbon pool fires, which are not appropriate to be employed to predict the large LPG pool fires. In contrast, Eq. (3.16) can predict the flame height of large LPG pool fires in the still air with much smaller deviations (see Figures 3.9 to 3.12), which suggests that specific correlations should be developed for corresponded specific hydrocarbon fuels if more accurate values need to be obtained, because different hydrocarbon fuels have corresponded combustion parameter values, i.e., stoichiometric composition mole fraction φ_{st} and inverse volumetric expansion ratio due to combustion ω. These parameters have significant impacts on flame height prediction using Eq. (3.16) for LPG pool fires.

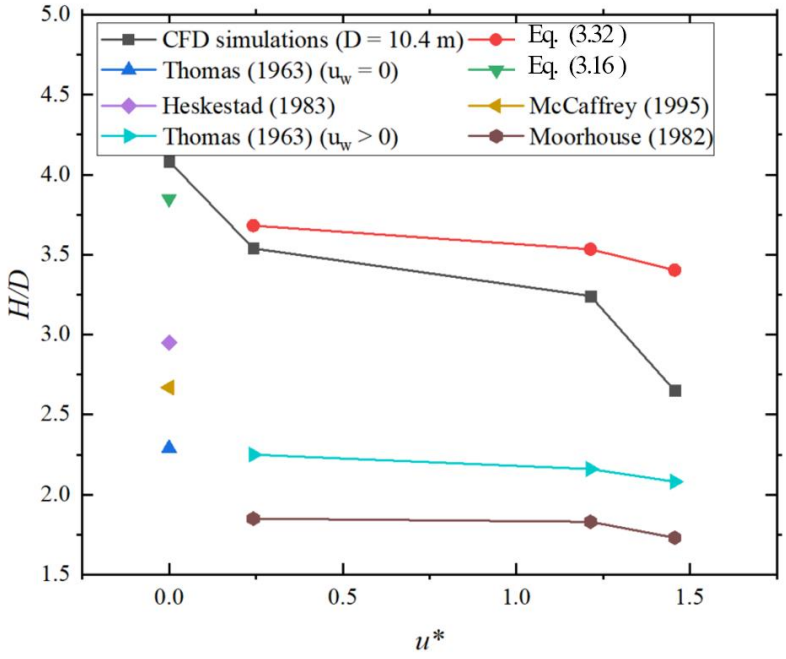

Figure 3.9 Relationships between the nondimensionalized flame height H/D and nondimensionalized air velocity u^* ($0 \le u^* \le 1.46$) with D = 10.4 m.

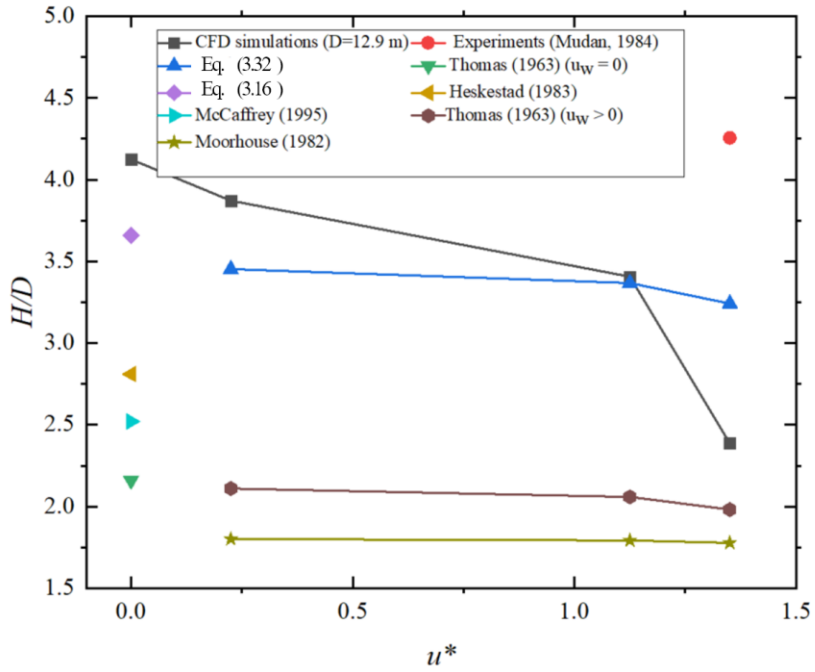

Figure 3.10 Relationships between the nondimensionalized flame height H/D and nondimensionalized air velocity u^* ($0 < u^* \le 1.35$) with D = 12.9 m.

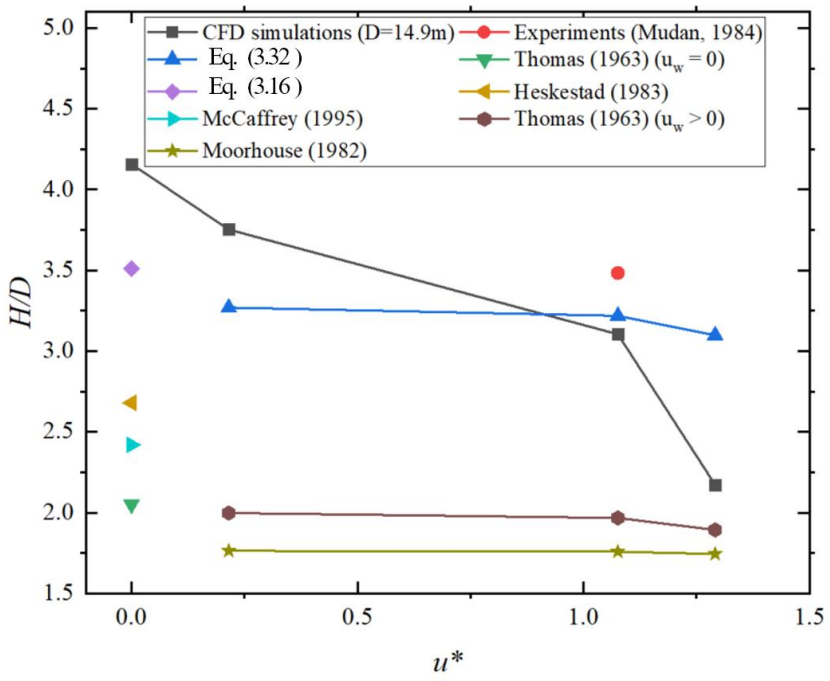

Figure 3.11 Relationships between the nondimensionalized flame height H/D and nondimensionalized air velocity u^* ($0 < u^* \leq 1.23$) with D = 14.9 m.

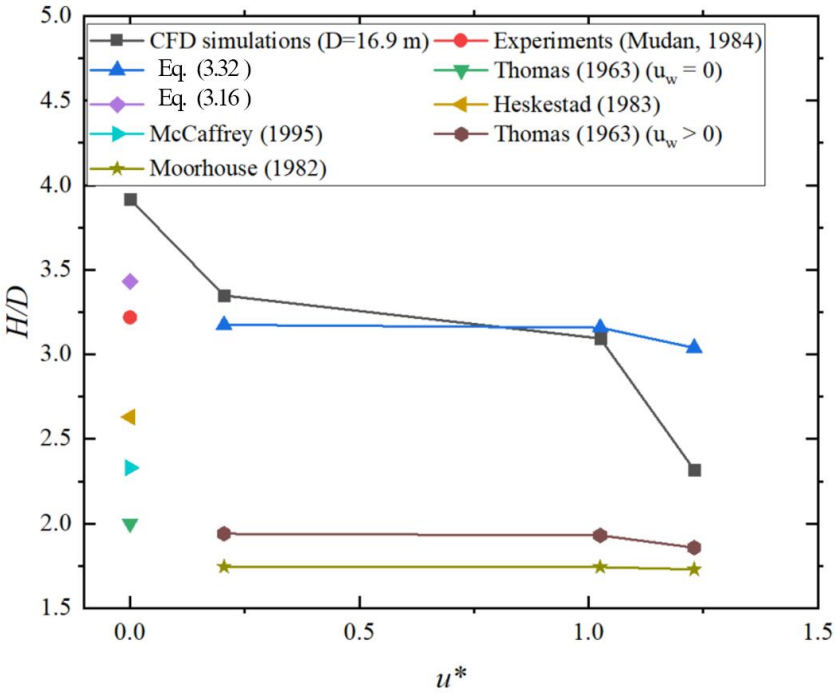

Figure 3.12 Relationships between the nondimensionalized flame height H/D and nondimensionalized air velocity u^* ($0 < u^* \leq 1.29$) with D = 16.9 m.

Furthermore, the wind velocity plays a significant role in the flame height, which can be observed from Figures 3.8 to 3.12. Flame heights comparisons between the CFD simulations, experiments, and empirical models (see Eqs. (3.19) and (3.21)) have also been made for large LPG pool fires with different ambient wind velocities (see Figures 3.9 to 3.12). It can be found that the flame height decreases as the wind velocity increases, which is due to the enhanced convection effect on vaporized fuel towards the horizontal direction compared with the vertical direction (also see Figures 3.5 to 3.8). It is worth mentioning that the experimental data for the pool fire with D = 12.9 m and u^* = 1.35 (u_w = 3 m/s) (see Figure 3.10) does not agree well with the CFD simulation results and other empirical models, which may be induced by the experimental measurement errors. Additionally, CFD simulations (see the slopes in Figures 3.9 to 3.12) show that the flame height decreases faster when u_w is between 2.5 m·s^{-1} and 3.0 m·s^{-1} than the cases when u_w is between 0 to 2.5 m/s. Such trends may due to that the air velocity larger than 2.5 m/s in the horizontal direction has a tremendous impact on the movement behavior of vaporized fuel gases in the vertical direction. while further investigation is needed in the near future. Based on the CFD simulation results shown in Figures 3.9 to 3.12, a new correlation is proposed to facilitate the estimation of flame heights for large LPG pool fires in engineering applications. Specifically for the LPG in the U.S., i.e., 100% propane (Hahn, 2019), the form of the new correlation is developed based on an existing paper (P. H. Thomas, 1963), which is given as follows:

$$H/D = 90\left(\dot{m}''/\rho_a\sqrt{gD}\right)^{0.67}(u^*)^{-0.21}, \quad (0 < u_w \leq 2.5\ m/s, 10\ m\ \leq D\ \leq 20\ m) \tag{3.32}$$

where u^* is a non-dimensional air velocity which is defined by Eq. (3.20). Equation (3.32) provides more precise predictions for flame heights in the air velocity ($0 < u_w \leq 2.5$ m/s) compared with empirical correlations shown in Figures 9 (a) to (d). It is worth mentioning Eq. (3.32) is only available for pure propane. For other LPG compositions, Eq. (32) need to be further revised.

3.5.3 Flame Tilt Angle *vs.* Pool Diameter and Wind Velocity

Figures 3.5 to 3.8 show the flame tilt behaviors that are obtained by CFD simulations for large LPG pool fires with different diameters (10.4 m $\leq D \leq$ 16.9 m) and wind velocity ($0 \leq u_w \leq 3$ m/s). In addition, Table 2.3 quantitatively summarizes how the flame tilt angle varies with the change of pool diameter at different wind velocity. It can be observed from Figures 3.5 to 3.8 that the wind velocity also has a significant effect on the flame tilt angle due to the enhanced horizontal convection of the evaporated fuel. Indeed, the fire plume will lean downwind, and higher wind velocity will lead to a larger tilt angle at the same burning rate. Also, higher wind velocity will cause a more significant impact on the fire shape which is highly consistent with the high-concentration region of the evaporated LPG. Among all CFD simulation results, the maximum tilt angle appears at the pool fire with D = 10.4 m and u_w = 3.0 m/s. It indicates that pool fire with a larger diameter will be less sensitive to the wind velocity. Indeed, larger pool diameter of the LPG pool fire indicates a higher burning rate $\dot{m}$ (see Figure 3.3), so that the wind velocity effect will become relatively less important on evaporated fuel plume.

Table 3.3. Flame tilt angles for pool fires with different pool diameters (m) and wind velocities (m/s)

	D = 10.4	D = 12.9	D = 14.9	D = 16.9
u_w = 0.0	0°	0°	0°	0°
u_w = 0.5	4.1°	4.0°	3.9°	3.1°
u_w= 2.5	18.2°	14.2°	11.2°	8.0°
u_w = 3.0	28.8°	27.2°	25.5°	20.7°

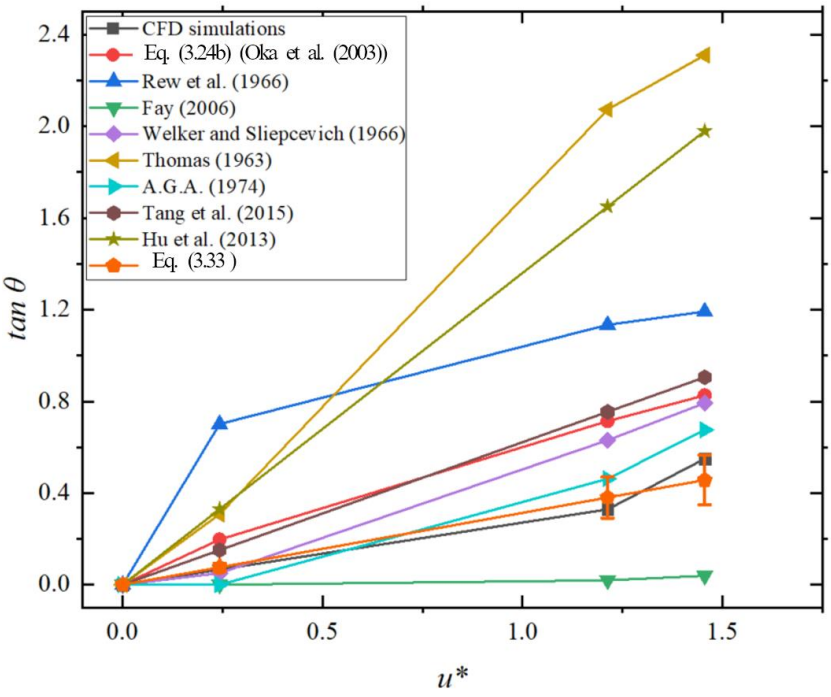

Figure 3.13 Relationships between nondimensionalized flame tilt $\tan\theta$ and nondimensionalized wind velocity u^* ($0 \le u^* \le 1.46$) with D = 10.4 m.

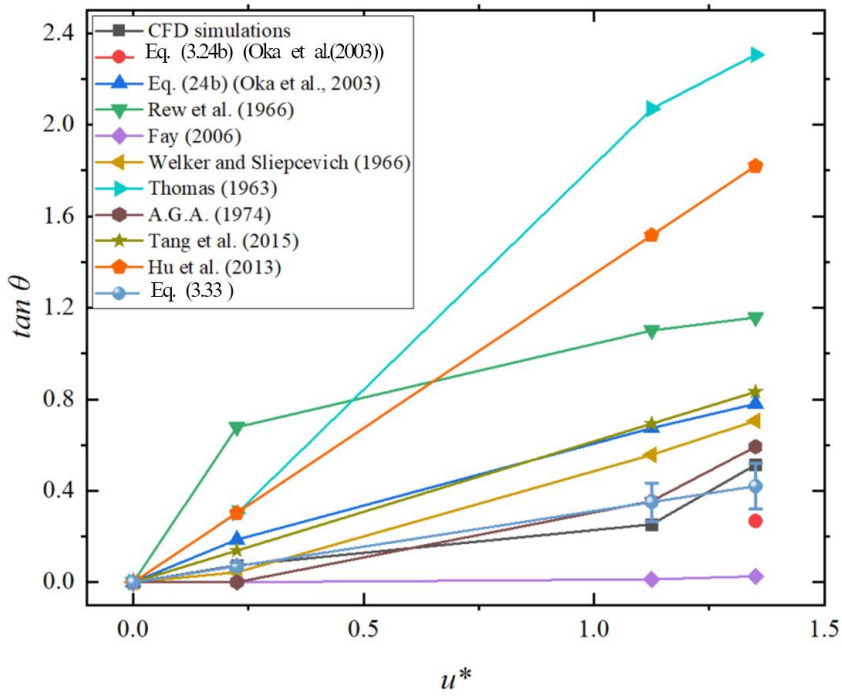

Figure 3.14 Relationships between nondimensionalized flame tilt $\tan\theta$ and nondimensionalized wind velocity u^* ($0 \le u^* \le 1.35$) with D = 12.9 m.

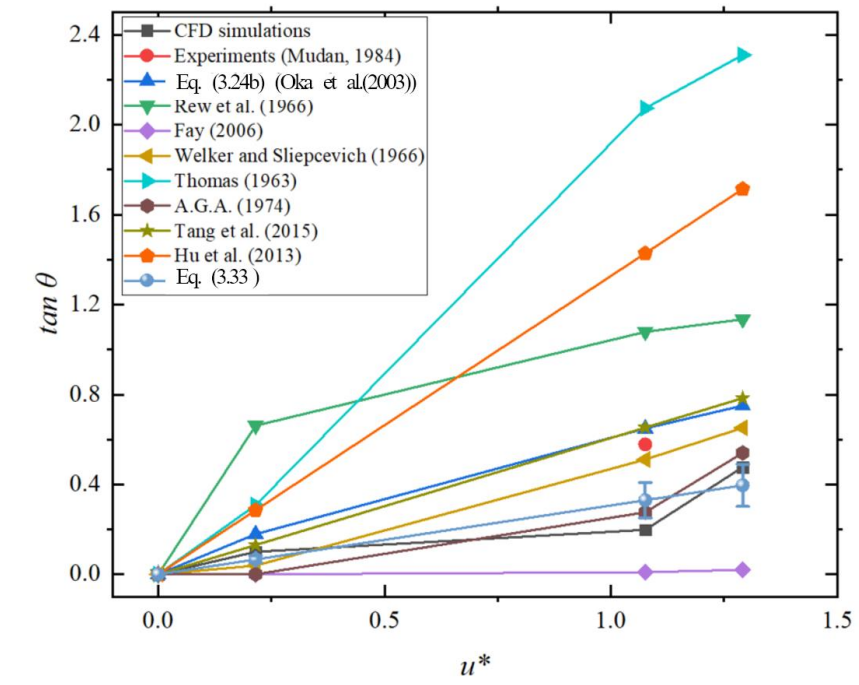

Figure 3.15 Relationships between nondimensionalized flame tilt $\tan\theta$ and nondimensionalized wind velocity u^* $(0 \le u^* \le 1.23)$ with D = 14.9 m.

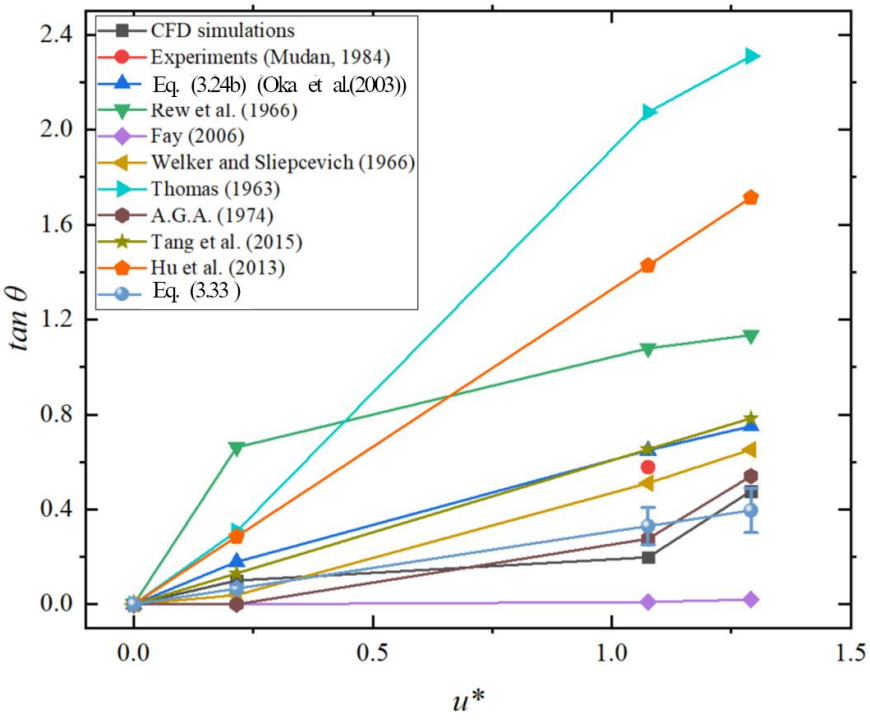

Figure 3.16 Relationships between nondimensionalized flame tilt $\tan\theta$ and nondimensionalized wind velocity u^* $(0 \le u^* \le 1.29)$ with D = 16.9 m.

To obtain the effects of wind velocity on flame tilt angle for large LPG pool fires, the results from CFD simulations, empirical models, correlations, and experiments (K. S. Mudan, 1984) have been analyzed and compared in Figures. 3.13 to 3.16. The observation from Figures. 3.13 to 3.16 also shows that the tilt angle increases with the increase of wind velocity. Compared with the CFD results, Eqs. (3.25), (3.28), and (3.31) overestimate the wind effects on the tilt angle of large LPG pool fires with diameters from 10.4 to 16.9 m. It is also interesting to find that Eq. (3.25) predicts a trend that the slope is smaller in the air velocity (0.5 m/s $\leq u_w \leq$ 2.5 m/s) than the corresponding value with the air wind from 0 to 0.5 m/s (see Figures. 3.13 to 3.16), which is different from other empirical correlations and CFD simulations. The reason for this phenomenon needs further study. In contrast, Eq. (3.26) underestimates the wind effects on the tilt angle when comparing with other models and correlations. Therefore, the Froude number *Fr* and other parameters in Eq. (3.26) need to be correlated further when it is employed to investigate air effects on large LPG pool fires. In Figures. 3.13 to 3.16, CFD simulations show that the flame tilt angle increases increase in wind velocity from 0 to 3 m/s and matches experimental results better than other empirical correlations. Subsequently, Eq. (3.27) shows best agreements with CFD simulations with the air velocity u^* from 0 to 0.5, and Eq. (3.29 (b)) matches the CFD simulations best when wind velocity u^* higher than 0.5 among all empirical correlations. Furthermore, according the correlations developed by Tang et al. (Tang et al., 2015) for acetone pool fires and Hu et al. (L. Hu et al., 2013) for the n-heptane and ethanol pool fires, an available correlation for flame tilt angle in large LPG pool fires (10 m $\leq D \leq$ 20 m) was proposed in a similar way based on results from the empirical correlations and simulations expressed by:

$$tan\theta = (2.1 \pm 0.4)\left(\frac{\rho_a c_p (T_F - T_a){u_w}^5}{\dot{m}'' D^2 \Delta H_c}\left(\frac{T_a}{g(T_F - T_a)}\right)^2\right)^{0.2}, (10\ \text{m} \leq D \leq 20\ \text{m}, 0 \leq u_w \leq 3\ \text{m/s}) \quad (3.33)$$

Figures. 3.13 to 3.16 show that the new proposed correlation Eq. (3.33) provides better predictions of flame tilt angles compared with CFD results than other empirical models for large LPG pool fires with the diameters (10 m $\leqslant D \leqslant$ 20 m).

3.6 Summary

In this chapter, numerical simulations were performed using an experimentally validated CFD model to simulate large LPG (100% propane) pool fires and predict the fire configuration characteristics, including flame height and flame tilt. The impacts of pool diameter and wind velocity on the fire configuration characteristics were investigated. Based on the CFD results and the parametric analysis, new correlations are proposed to provide more accurate estimations of flame height and tilt specifically for large LPG pool fires. Quantitative conclusions are listed as follows:

- The selection of the burning rate model can significantly influence the accuracy of flame height predictions using the CFD model. Johnson's burning rate model is the best model among the three burning rate models employed in this study.
- Higher horizontal wind velocity will lead to a stronger convection effect in the horizontal direction. As a result, it will reduce the flame height and increase the flame tilt angle.
- The configuration of LPG pool fires with larger diameters will be less sensitive to the ambient wind velocity.
- The new correlations proposed in this study provide more accurate predictions of the flame height and tilt angle than any existing empirical models. The two correlations will facilitate engineers and scientists when estimating the flame configurations for large LPG pool fires with pool diameters between 10 m and 20 m, and ambient wind velocity between 0 and 3 m/s.

In summary, addressing the deficiencies of experiments, the CFD model has been employed to provide high-resolution data to investigate how large LPG pool fire configurations can be influenced by pool diameter and wind velocity. With the enhanced fundamental understandings and the new proposed correlations of flame height and tilt, the numerical study and parametric analysis of the current chapter can be further employed to facilitate the precise risk assessment for large LPG pool fires in a time-saving and cost-effective manner.

CHAPTER IV

LUNG DISEASE EFFECT ON THE COUGH-DRIVEN MUCUS MOVEMENT AND CLEARANCE IN AN IDEALIZED UPPER AIRWAY MODEL USING VOF

4.1 Introduction

The inner surface of airways is covered by airway mucus (Y. Y. Hu et al., 2015), which serves as a highly effective defender to trap inhaled toxicants (i.e., toxic particles and gases produced from large LPG pool fires) and clear them out of the human respiratory systems driven by cilia beating motion and cough (Fahy & Dickey, 2010; Levy et al., 2014; C. P. van der Schans et al., 1999). Mucus is identified as a non-Newtonian fluid (Yeates, 1990), and presents viscoelastic behaviors (Hill et al., 2014; Lai et al., 2009) and shear-thinning characteristics (Basser et al., 1989; Quraishi et al., 1998). It has been observed that shear stress between air and mucus is proportional to the square of airflow rate in the lung airways (G. B. Wallis, 1969). In a healthy lung, the mucus thickness is between 2 and 50 μm in the trachea, and approximately 7 μm in the conducting airways (Karamaoun, Sobac, Mauroy, Van Muylem, & Haut, 2018; Leal, Smyth, & Ghosh, 2017; Bruce K Rubin, 2002; Sanders, Rudolph, Braeckmans, De Smedt, & Demeester, 2009; D. J. Smith, E. A. Gaffney, & J. R. Blake, 2008; Zheng, 2011). However, with chronic obstructive

pulmonary disease (COPD), mucus will be hyper-secreted, leading to impaired clearance efficiency to the inhaled particles and pathogens (Zheng, 2011). Specifically, the hypersecretion results in increased mucus viscosity and thicknesses, which can potentially block the airway, reduce the gas exchange efficiency, and increase the resistance of mucus to be cleared by coughs (Basser et al., 1989; Button & Boucher, 2008; Emmanouil, 2019; Groth, Macri, & Foster, 1997; Lai et al., 2009; Ren et al., 2020; Richardson, 2003; Salvaggio, 1994; Samet & Cheng, 1994; R. J. Thomas, 2013; Tran, 2007; Turner & Bothamley, 2014; Cees P van der Schans, 2007; J. Yang, Kim, Park, McDowell, & Kim, 2020; Zanin, Baviskar, Webster, & Webby, 2016). The mucus viscosity in the diseased lung can range from 0.01 to 100 $Pa \cdot s$ with shear-thinning characteristics (Dulfano, Adler, & Philippoff, 1971; Jeanneret-Grosjean, King, Michoud, Liote, & Amyot, 1988; C. S. Kim, Rodriguez, et al., 1986; Lai et al., 2009; Puchelle, Zahm, & Duvivier, 1983; Bruce K. Rubin, Ramirez, & Ohar, 1996; Bruce K. Rubin, Ramirez, Zayas, Finegan, & King, 1990; Shah et al., 1996; Zayas, Man, & King, 1990).

Research efforts have been made to study the mucus movement and clearance using both experiments and computational studies. Qualitative studies have identified that airflow rates, mucus layer thickness, and viscosity are the essential factors affecting mucus clearance in the pulmonary airways (C. S. Kim, Rodriguez, et al., 1986; G. B. Wallis, 1969; Graham B. Wallis & Dodson, 1973). It has been proved that high expiratory airflow rates can overcome the viscous resistance and gravity, and clear the mucus out more effectively (C. S. Kim, Greene, et al., 1986; C. S. Kim et al., 1987; C. S. Kim, Rodriguez, et al., 1986; Paz et al., 2019; Rajendran & Banerjee, 2019). Although experiments have been carried out to investigate the mechanism of mucus clearance driven by airflow in straight tubes to approximate the trachea (R. Camassa et al., 2012; C. S. Kim, Greene, et al., 1986; C. S. Kim et al., 1987; C. S. Kim, Rodriguez, et al., 1986; King et al., 1985), it is still challenging to perform such investigations in physiologically realistic airway replicas due

to the geometric complexity. To address the gap in the research mentioned above in geometries with realistic airway anatomy, the Volume of Fluid (VOF) methods and Eulerian Wall Film model has been employed to track both air and mucus phases (Paz et al., 2019; Rajendran & Banerjee, 2019; Ren et al., 2020). Specifically, Paz et al. (2019) employed a transient 3D VOF model to study the mucus movement and clearance in both a straight tube and a subject-specific trachea model. They found that an oscillating airflow would enhance clearance by up to 5 % than a steady-state airflow in the straight tube and the trachea. Simplifying mucus as a Newtonian fluid, Rajendran and Banerjee (2019) employed a VOF model and simulated steady-state expiration of air-mucus two-phase flow in an idealized bifurcating geometry representing generation 0 (G0) to generation 2 (G2). They discovered that the Dean's flow in the bifurcations could lead to non-uniform mucus thickness distributions. Other than using the VOF method, Ren et al. (2020) employed the Eulerian Wall Film model and found that mechanical ventilation techniques can significantly improve the mucus clearance efficiency than spontaneous coughing.

However, there are still many key questions that have not been answered, i.e., (1) Will simplifying the mucus as a Newtonian fluid significantly impact the mucus movement and clearance predictions than using the realistic non-Newtonian fluid properties? (2) How do COPD-induced variations in mucus thickness and viscosity influence the cough-driven mucus movement and clearance efficiency? To partially answer the abovementioned questions, this study employed an experimentally validated 3D VOF model to predict the cough-driven mucus transport and clearance in an idealized upper airway model from mouth to trachea. To investigate the impacts of mucus viscosity, mucus thickness, and cough intensity on mucus transport and clearance, both Newtonian and non-Newtonian viscosity models were used. Specifically, two different mucus thicknesses, i.e., 1.0 mm and 0.5 mm, were employed, which represent different severities of the COPD conditions. Furthermore, two cough waveforms with different average flow rates were used, and the resultant

mucus movements and clearances were compared. The work fulfilled in current chapter has been submitted in a scientific journal and under the review processing.

4.2 Research Objectives

Investigating lung disease effect on the cough-driven mucus movement and clearance in an idealized upper airway model using a VOF model, several research objectives are listed as follows:

- Developing an experimentally validated VOF model to predict the mucus clearance and movement behaviors in an idealized upper airway.
- Comparing the accuracy in mucus transport and clearance efficiencies with the simulations between Newtonian fluid and non-Newtonian fluid.
- Quantitatively studying the cough intensity effects on mucus clearance and movement behaviors in an idealized upper airway.
- Quantitatively investigating the COPD level effects on mucus clearance and movement behaviors in an idealized upper airway.

4.3 Theory

The Volume of Fluid (VOF) model (Hirt & Nichols, 1981) can be employed to track the interface of two immiscible fluids, and it has dominant advantages to trace the interface behaviors and capture the changes of surface tension on the interface between mucus flow and airflow (Ishii & Hibiki, 2011). In this study, air and mucus are considered as the primary phase and the secondary phase, respectively. Air and mucus are assumed to be non-interpenetrating. To track both phases, the mucus volume fraction is defined as:

$$\alpha_m = \frac{V_m}{V} \tag{4.1}$$

where α_m is the mucus volume fraction, V_m is the mucus volume in a certain mesh cell, and V is the mesh cell volume. The air volume fraction is obtained based on the following constraint:

$$\alpha_a = 1 - \alpha_m \tag{4.2}$$

Accordingly, the air-mucus mixture properties can be determined by:

$$\rho = \alpha_m \rho_m + \alpha_a \rho_a \tag{4.3}$$

$$\mu = \alpha_m \rho \mu_m + \alpha_a \mu_a \tag{4.4}$$

where ρ and μ are the mixture density and viscosity in this chapter.

It is worth mentioning that existing studies assume mucus is a Newtonian fluid (Paz, Suarez, et al., 2017; Paz, Suárez, et al., 2017; Paz et al., 2019; Rajendran & Banerjee, 2019). However, since mucus is non-Newtonian and shear-thinning liquid (C. S. Kim, Greene, et al., 1986; C. S. Kim et al., 1987; C. S. Kim, Rodriguez, et al., 1986), it is unknown whether the Newtonian simplification will induce significant differences in the predictions of mucus transport and clearance. Therefore, to address the abovementioned gap, this study employed both Newtonian and non-Newtonian mucus viscosity models, and compared the differences in the CFD simulation results. Specifically, in this study, mucus viscosity 7.9 $Pa \cdot s$ was employed for the Newtonian fluid simulations (C. S. Kim, Greene, et al., 1986). Besides, a non-Newtonian power-law model was also employed in this study to represent realistic shear-thinning behaviors. (Cone, 2009; Fahy & Dickey, 2010; Lai et al., 2009; Ren et al., 2020; Sanchez, Hume, Chatelin, & Poncet, 2018). Specifically, the non-Newtonian μ_m can be defined as

$$\mu_m = \begin{cases} \mu_{mMin} \ (\gamma \geq \gamma_{Max}) & \text{(4.5a)} \\ a\gamma^b \ (\gamma_{Min} < \gamma < \gamma_{Max}) & \text{(4.5b)} \\ \mu_{mMax} \ (\gamma \leq \gamma_{Min}) & \text{(4.5c)} \end{cases}$$

In Eqs. (4.5 (a-c)), a is the consistency index (CI), which is the average mucus viscosity, and b is the power-law index, which is equal to -0.85 in this study (Ren et al., 2020). In addition, γ_{Min} and γ_{Max} are minimum and maximum shear rates, respectively. The mucus viscosities, i.e., 1.0 to 14.8 $Pa \cdot s$ with corresponded minimum and maximum shear rates representing lung diseases

conditions, employed to study the non-Newtonian fluid affecting mucus transport behaviors (see Figure 4.1) (C. S. Kim, Greene, et al., 1986; Lai et al., 2009).

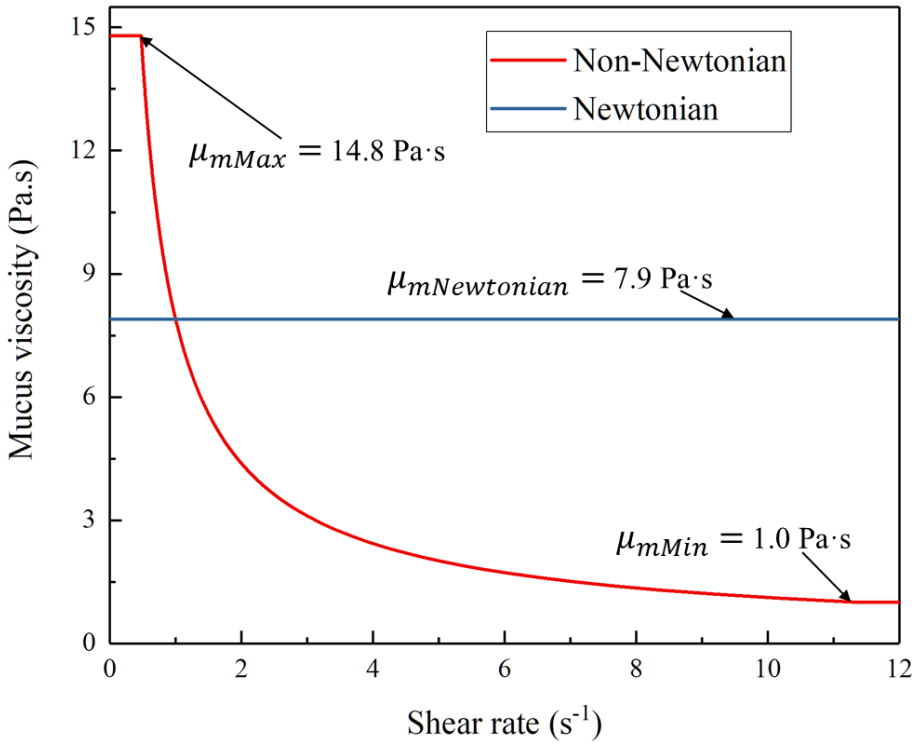

Figure 4.1 Newtonian and non-Newtonian mucus viscosities employed in this study.

4.3.1 Governing Equations

Continuity Equation

The continuity equation for the mucus can be given as

$$\rho_m\left(\frac{\partial}{\partial t}\alpha_m + \nabla\cdot(\alpha_m\vec{v}_m)\right) = \dot{m}_{am} - \dot{m}_{ma} \tag{4.6}$$

where $\vec{v}_m$ is mucus velocity vector, $\dot{m}_{am}$ is the mass transfer from the air phase to the mucus phase, and $\dot{m}_{ma}$ is the mass flow rate transferring from the mucus phase to the air phase. The air volume fraction α_a can be determined using Eq. (4.2).

Momentum Equation

The momentum equation for the air-mucus mixture will be solved and given by

$$\frac{\partial}{\partial t}(\rho\vec{v}) + \nabla \cdot (\rho\vec{v}\vec{v}) = -\nabla p + \nabla \cdot \left(\mu(\nabla\vec{v} + \nabla\vec{v}^T)\right) + \rho\vec{g} + \vec{F}_{CSF} \tag{4.7}$$

where $\vec{v}$ is velocity vector, $\vec{g}$ is gravity vector, and p is pressure. The mixture density ρ and viscosity μ can be determined by Eqs. (4.3) and (4.4). $\vec{F}_{CSF}$ is the surface tension force between air and mucus, which can be calculated via:

$$\vec{F}_{CSF} = 2\beta\frac{\rho\kappa\vec{n}}{\rho_m + \rho_a} \tag{4.8}$$

where β is the surface tension coefficient, which is equal to 0.032 N/m (Clements, Brown, & Johnson, 1958; Hamed & Fiegel, 2014). Specifically, Eq. (4.8) is based on the continuum surface force (CSF) method (Brackbill, Kothe, & Zemach, 1992), in which the surface curvature κ can be defined as

$$\kappa = \nabla \cdot \hat{n} \tag{4.9}$$

$$\vec{n} = \nabla\alpha \tag{4.10}$$

$$\hat{n} = \frac{\vec{n}}{|\vec{n}|} \tag{4.11}$$

where κ is surface curvature, $\hat{n}$ is the divergence of the unit normal, α is volume fraction, and $\vec{n}$ is the volume fraction gradient.

Wall adhesion is also enabled in the VOF model in conjunction with the CSF model. Rather than imposing this boundary condition at the wall itself, the contact angle θ_w is used to adjust the surface normal in computational cells near the wall, and the surface normal at the computational cell next to the wall (Brackbill et al., 1992) can be expressed by

$$\hat{n} = \hat{n}_w cos\theta_w + \hat{t}_w sin\theta_w \quad (4.12)$$

where $\hat{n}_w$ and $\hat{t}_w$ are unit normal and tangential vectors to the wall, respectively.

4.3.2 Mucus Clearance Efficiency

To calculate the mucus clearance efficiency η_{ce}, the definition in a previous study is employed (Paz et al., 2019), i.e.,

$$\eta_{ce} = \frac{\Delta V_m}{V_{m,ini}} \times 100\% \quad (4.13)$$

where $V_{m,ini}$ is the initial total mucus volume in the computational domain, and ΔV_m is the mucus volume change along the cough-wave.

4.4 Numerical Method

4.4.1 Geometry and Mesh

To unveil the underlying fluid dynamics of disease-specific air-mucus flows with different mucus thicknesses, σ, two idealized mouth-to-trachea (MT) models (see Figures 4.2 (a)-(c)) were created based the upper airway model used in existing experimental and numerical studies (Y.-S. Cheng et al., 1999; Y. Feng, Kleinstreuer, Castro, & Rostami, 2016). Different mucus thicknesses represent different COPD severities ($\sigma = 1.0\ \ mm$ and $\sigma = 0.5\ \ mm$), i.e., GOLD I and GOLD II, respectively (Fahy & Dickey, 2010; C. S. Kim, Rodriguez, et al., 1986; Paz et al., 2019). To comprehensively analyze the regional mucus transport behaviors under various cough and disease conditions, the MT model is divided into three different zones, i.e., Zone 1 (Z-1), Zone 2 (Z-2), and Zone 3 (Z-3) (see Figure 4.2 (a)). Specifically, Z-1 covers the trachea region with, Z-2 represents the region from the glottis to the soft palate, and Z-3 contains the region from the soft palate to the mouth opening.

For the computational mesh, poly-hexcore meshes were generated using ANSYS Fluent Meshing (ANSYS Inc., Canonsburg, PA). Mesh details for the two MT models are shown in Table 4.1 and

Figures 4.2 (b) and (c). Grid sensitivity was investigated by the comparisons of nondimensionalized velocity profiles V^*at the selected lines, i.e., A-A' and B-B', with an inhalation airflow rate 27.5 ml/s at the mouth opening (see Figures 4.3 (a) and (b)) (Y. Feng et al., 2016). Using different meshes (see Table 4.2), the comparisons between the nondimensionalized velocity magnitude V^* along lines A-A' and B-B' are shown in Figures 4.3 (a) and (b).

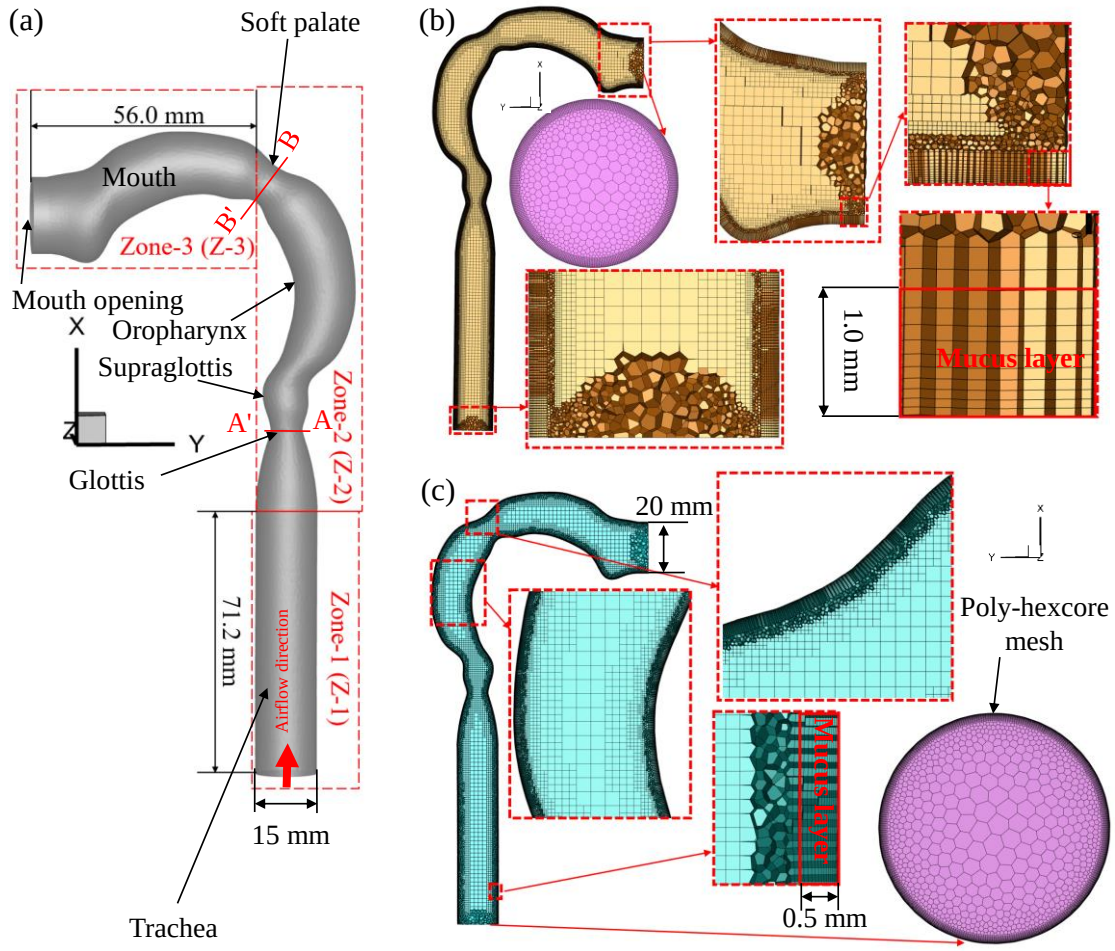

Figure 4.2 Schematic of the computational domain with the hybrid mesh details in the two mouth-to-trachea (MT) upper airway models with different mucus thicknesses σ: (a) Schematic of the MT upper airway geometry; (b) Mesh details of the MT upper airway geometry with σ = 1.0 *mm*; (c) Mesh details of the MT upper airway geometry with σ = 0.5 *mm*.

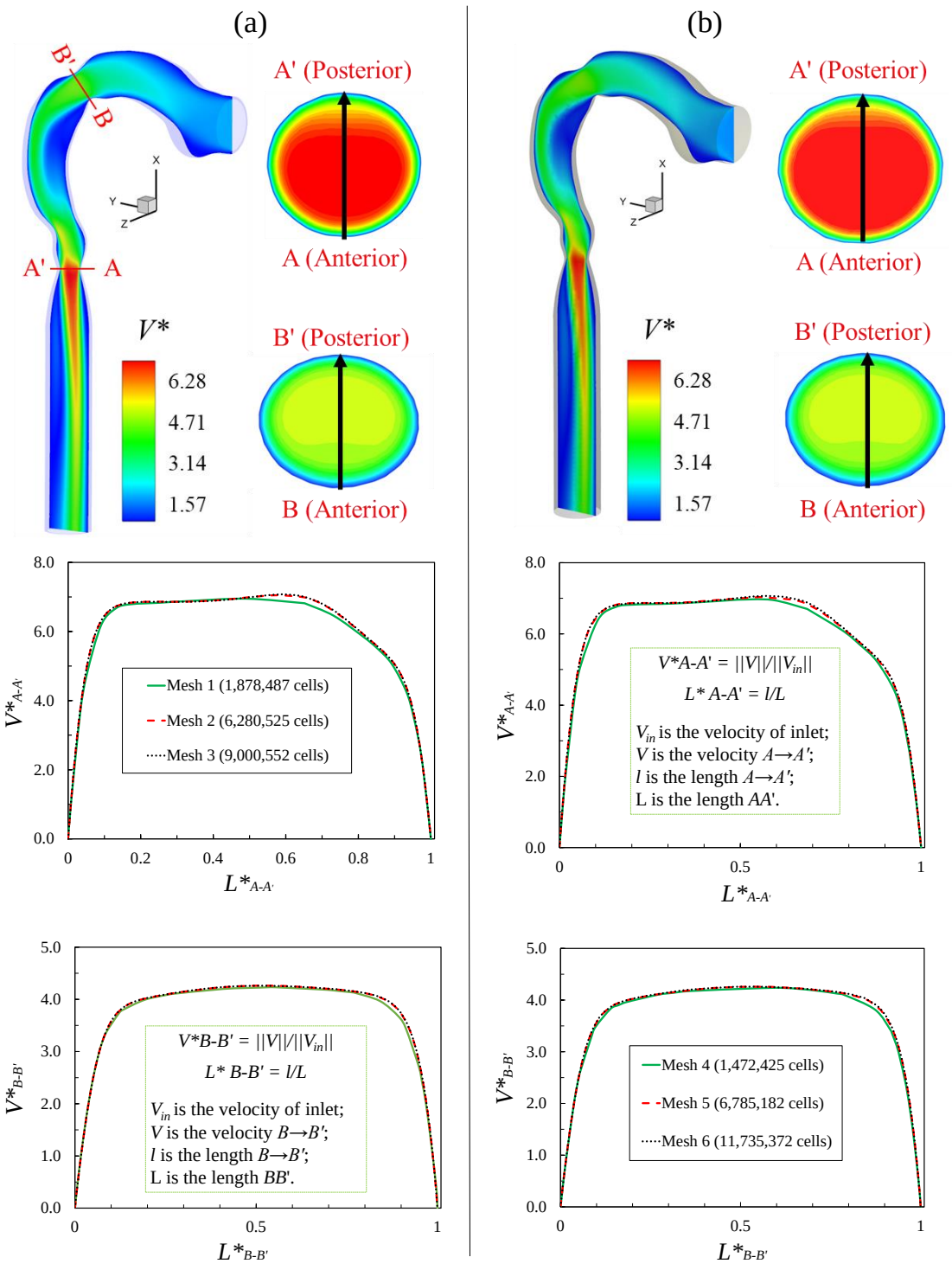

Figure 4.3 Mesh independence tests for the two MT models: (a) $\sigma = 1.0\ mm$; (b) $\sigma = 0.5\ mm$.

It can be observed that Mesh 1 and Mesh 4 are too coarse to obtain accurate results. The variations of simulated velocity profiles are within 1.0 % between Mesh 2 and Mesh 3, and between Mesh 5 and Mesh 6 (see Figures 4.3 (a) and (b)). Thus, Mesh 2 and Mesh 5 are selected as the final meshes for both MT models with the optimal balance between computational efficiency and accuracy.

Table 4.1 Mesh details in the mesh independence tests for air-driven mucus clearance simulations using the VOF model.

Geometry	Mesh	Prism layers	Minimum-size (mm)	Volume-maximum skewness	Volume elements
Upper airway ($\sigma = 1.0$ mm)	Mesh 1	12	0.083	0.61	1,878,487
	Mesh 2 (Final)	12	0.05	0.61	6,280,525
	Mesh 3	20	0.05	0.71	9,000,552
Upper airway ($\sigma = 0.5$ mm)	Mesh 4	12	0.083	0.60	1,472,425
	Mesh 5 (Final)	15	0.02	0.43	6,785,182
	Mesh 6	30	0.02	0.60	11,735,372

4.4.2 Boundary and Initial Conditions

Inlet Boundary Conditions with Transient Cough-wave

Two transient cough waveforms were applied as the inlet boundary conditions at the trachea opening (see Figure 4.4), representing the expiratory conditions. Specifically, to study cough strength effects on mucus movement and clearance in the upper airway, two different transient cough waveforms were employed with different averaged flow rates (see Figure 4.4). As shown in Figure 4.4, the waveform of CS-I is based on the tests from 25 subjects (J. K. Gupta, Lin, & Chen, 2009; Leiner, Abramowitz, Small, & Stenby, 1966; Mahajan, Singh, Murty, & Aitkenhead, 1994), and it has been employed in existing research efforts (Dudalski et al., 2020; Y. Feng, Marchal, Sperry, & Yi, 2020; Jitendra K. Gupta, Lin, & Chen, 2011; L. Yang, Li, Yan, & Tu, 2017). The

other waveform CS-II was generated by artificially amplify the waveform of CS-I twice to investigate the cough strength effect on mucus movement and clearance.

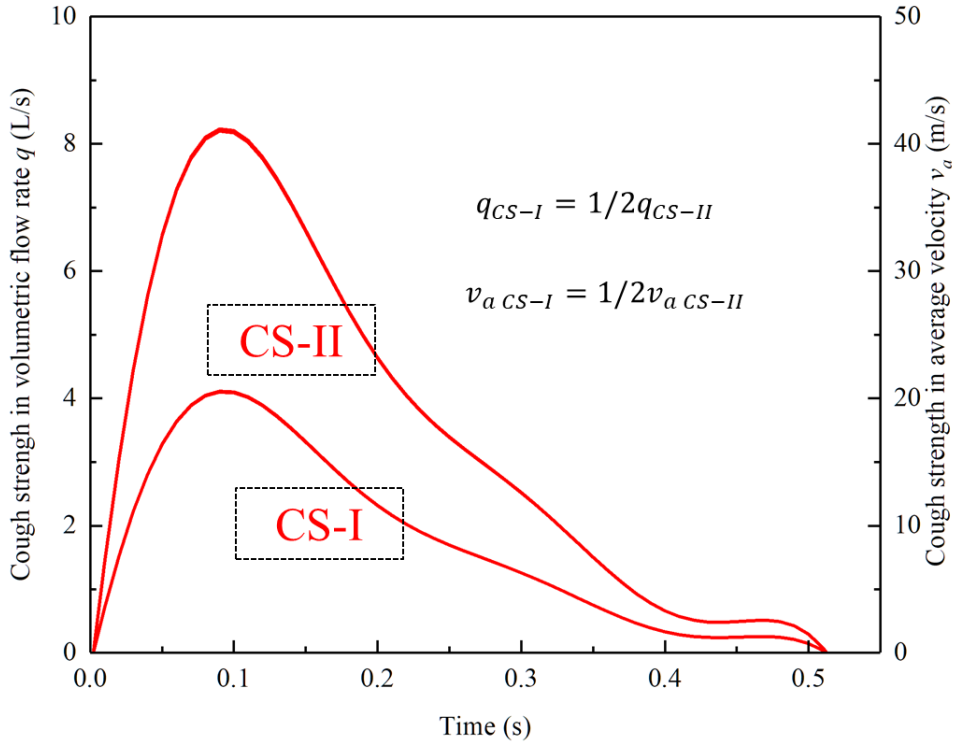

Figure 4.4 Expiratory cough waveforms with different intensities at the trachea openings.

Airway Wall and Outlet Boundary Conditions

The airway walls are assumed to be stationary and non-slip. The gauge pressure at the mouth opening is considered to be equal to the atmospheric pressure. Additionally, From-Neighboring-Cell was selected as the backflow direction specification method to guarantee the mucus-air movement behaviors adjacent to pressure conditions in the mouth (Dincer, 2018).

Initialization for Mucus Regions

To represent the existence of mucus layer at the inner wall of the airways, two mucus thicknesses σ = 0.5 mm and = 1.0 mm were used to represent two different COPD severities, i.e., GOLD I

and GOLD II (Fahy & Dickey, 2010; C. S. Kim, Rodriguez, et al., 1986; Paz et al., 2019), based on the fact that COPD stages in this work were classified by the high-secreted mucus volume lined to the airway wall, leading to constricted airway lumen and airflow obstructions (Ramos, Krahnke, & Kim, 2014). Additionally, the volume fraction, α_m, in the near-wall region with specific σ was initialized to be equal to 1.0.

4.4.3 Numerical Setup

The VOF simulations were performed using ANSYS Fluent 2020 R1 (ANSYS Inc., Canonsburg, PA). Simulations in the straight tube for model validations were performed on a local Dell Precision T7910 workstation (Intel®Xeon® Processor E5-2683 v4 with dual processors, 32 cores, and 256 GB RAM), which took approximately 48 hours to finish the simulation with the physical time duration 5.0 s. Simulations in the idealized upper airway model were executed on the supercomputer "Pete" at the High Performance Computing Center (HPCC) at Oklahoma State University (OSU) (Intel®Xeon® Processor Gold 6130 CPU with dual processors, 32 cores, 64 threads, and 96 GB RAM). In the simulations with the Newtonian fluid (7.9 $Pa \cdot s$), each case took about 120 hours to compute one cough-wave duration 0.5126 s, while it spent about 168 hours calculating one case with the non-Newtonian fluid (1.0 to 14.8 $Pa \cdot s$). The Pressure-Implicit with Splitting of Operators (PISO) algorithm was employed for the pressure-velocity coupling, and the least-squares cell-based scheme was applied to calculate the cell gradient. The Pressure Staggering Option (PRESTO!) scheme, the compressive method, and the first-order upwind scheme was used for the spatial discretization of pressure, volume fraction, and specific dissipation rate, respectively. In addition, the second-order upwind scheme was applied for the discretization of momentum and turbulent kinetic energy. Convergence is defined for continuity, momentum, and supplementary equations, when residuals are lower than 1.0e-3.

4.5 Results and Discussion

4.5.1 VOF Model Validation

To validate the VOF model, i.e., mucus thickness, mucus transport velocity and mucus volume fraction were compared with the experimental data (C. S. Kim, Greene, et al., 1986) under different boundary conditions in the 3D straight tube (see Appendix B for the geometry and mesh details). In the simulations for model validation., the mucus feeding rate $q_m = 1$ ml/min, and the airflow rate $q_a = 19.5$ ml/min. The steady state was considered achieved when the mucus feed rate into the straight tube becomes equal to the mucus outflow rate. Dependent variables employed in the validation (see Figure 4.5) are defined as follows. The mean mucus layer transport velocity $\bar{v}_m$ is defined as

$$\bar{v}_m = \frac{4q_m}{\pi D^2}\left(1 - \left(1 - \frac{2\sigma}{D}\right)^2\right)^{-1} \tag{4.14}$$

where q_m is the mucus feeding rate, D is the straight tube diameter. Eq. (4.14) can be simplified with the function of mucus volume fraction α_m and as below

$$\bar{v}_m = \frac{4q_m}{\pi D^2 \alpha_m} \tag{4.15}$$

$$\sigma = \frac{D}{2}(1 - (1 - \alpha_m)^{-1}) \tag{4.16}$$

As shown in Figures 5 (a) to (c), except for the relative error between simulations and experiments (C. S. Kim, Greene, et al., 1986), which approximately 8% in mucus transport velocity $\bar{v}_m$, the relative errors in mean mucus layer thickness σ and mucus volume fraction α_m are less than 5% between simulations and experiments. With the good agreement compared with the experimental data, the VOF model is validated to predict mucus movement behaviors in this study.

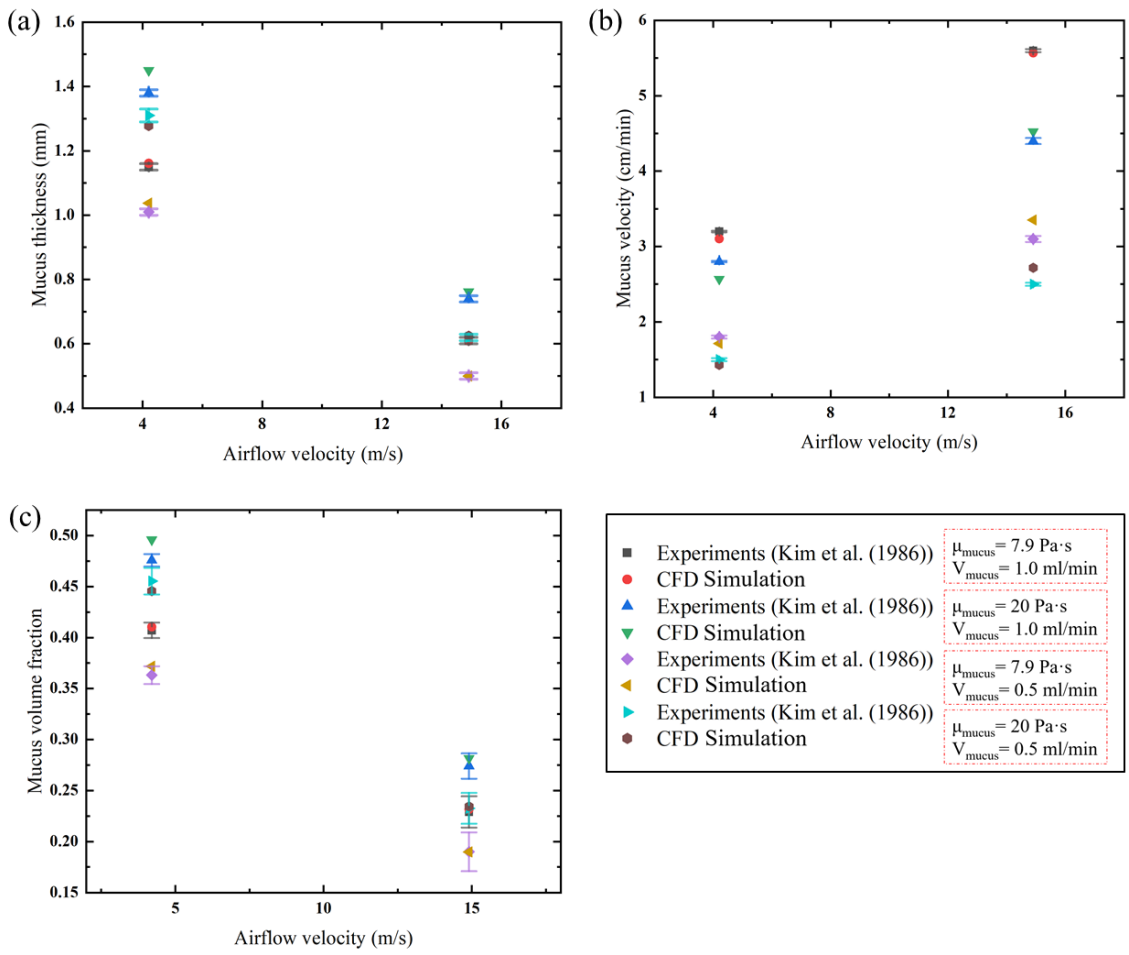

Figure 4.5 Comparison of computational results for a straight tube with experimental data (Kim, Greene, et al., 1986): (a) Relationship between mucus thickness and airflow velocity; (b) Relationship between mucus velocity and airflow velocity; and (c) Relationship between mucus volume fraction and airflow velocity.

4.5.2 Newtonian vs. Non-Newtonian Mucus Viscosity Models

To investigate whether using Newtonian fluid to model mucus will induce large differences in mucus transport and clearance, the CFD results are compared between using Newtonian fluid and non-Newtonian fluid models. Specifically, Figures 4.6 & 4.7 manifest significant differences between the Newtonian fluid (7.9 $Pa \cdot s$) and non-Newtonian fluid (1.0 to 14.9 $Pa \cdot s$) in calculations of the mucus clearance efficiency η_{ce} in the different zones of the MT model. It shows

that the non-Newtonian fluid simulations provide higher mucus clearance efficiency than the Newtonian fluid simulations with the same cough strengths and mucus thicknesses. Such an observation is consistent with the perspectives from previous studies that pseudoplastic non-Newtonian fluids with the shear-thinning behavior can transport more efficiently than Newtonian fluids (Roberto Camassa et al., 2012; Chatelin, Anne-Archard, Murris-Espin, Thiriet, & Poncet, 2017; Mauroy, Fausser, Pelca, Merckx, & Flaud, 2011; Picchi, Poesio, Ullmann, & Brauner, 2017). It can also be proved directly not only from the comparisons of mucus clearance efficiency (see Figures 4.6 & 4.7), but also from results based on the average mucus volumetric flow rate $\bar{q}_m$ in a cough-wave at selected time stations in the MT models (see Table 4.2). In the non-Newtonian fluid simulations, it shows that the clearance efficiency η_{ce} or volumetric flow rate $\bar{q}_m$ is about 3.41 (with CS-II and $\sigma = 1.0\ mm$) to 7.80 (with CS-I and $\sigma = 0.5\ mm$) times higher than the values with the Newtonian fluid (see Tables 4.2 & 4.3). Similarly, regional clearance efficiencies in Z-1, Z-2, Z-3, and Z-1+Z-2 (see Figures. 4.1, 4.6, and 4.7) demonstrate that mucus can be transported faster by the cough-driven airflow using the non-Newtonian power-law model, which exhibits a proportional increase in shear rate as a function of shear stress (Żołek-Tryznowska, 2016).

These phenomena can be explained based on comparisons from the velocity profiles and vectors, and mucus distributions in the MT model (see Figures 4.8 to 4.15). Velocity magnitude V^* and mucus volume fraction α_m near the mucus-air interfaces at cross-sections C-C' in near the mouth opening and D-D' in the oropharynx are enlarged and shown in the highlighted regions (I, II, III, IV, V, and VI) in Figures 4.8 & 4.9.

Using the iso-surfaces $\alpha_m = 0.01$, the air-mucus interfaces are visualized in Figures. 4.10, 4.12, 4.13, and 4.14. Accordingly, the velocities in the mucus phase with $0.01 \leq \alpha_m \leq 1$ were employed to calculate the average mucus movement velocity $\bar{v}_m$. $\bar{v}_m$ at different sides of the cross-sections C-C' and D-D' are listed in Table 4.4. As shown by the comparisons between non-Newtonian fluid and Newtonian fluid (CS-I and $\sigma = 1.0\ mm$) at the locations near C and C' sides (I and II in Figures

4.8 (a)) at $t = 0.05\ s$, $\bar{v}_m$ in the non-Newtonian fluid simulations are approximately 0.1106 and 1.2277 m/s, while $\bar{v}_m$ in the Newtonian fluid simulations are much lower, i.e., 0.0029 and 0.1739 m/s at corresponding sides. The abovementioned comparison indicates that the mucus near the air-mucus interface can be cleared more than 3 times faster than the Newtonian fluid at this time location (see Figures 4.8 (a) and Table 4.4). Using Newtonian fluid property may underpredict the mucus clearance efficiency with significant errors. The velocity vectors shown in Figures. 12 & 13 indicate that the changes in mucus distributions can lead to different secondary flow patterns. Specifically, stronger secondary flows are more likely developed in the non-Newtonian fluid with shear-thinning behavior (D'Avino, 2015). Similarly, the comparable results of average mucus movement velocity $\bar{v}_m$ at the locations close to both D and D' sides have been obtained under corresponding cough strength and mucus thickness between non-Newtonian fluid and Newtonian fluid at time stations, i.e., $t = 0.05\ s$ and $= 0.09\ s$, shown in Figures 4.9 (a) & (b) and Table 4.4. Moreover, non-Newtonian mucus velocity is lower than the simulation results with the Newtonian mucus simplifications (see Table 4.4) under stronger cough strength (CS-II) at $t = 0.40\ s$. This is due to the more dominant viscous dissipation effect of the airway wall boundaries with the thinner mucus layer in non-Newtonian simulations (see Figures. 4.8(c) & 4.9(c)) (Antonov & Bondarev, 1968).

Nevertheless, significant differences between the simulations using idealized Newtonian fluid and realistic non-Newtonian fluid viscosities were observed in mucus clearance efficiency and distributions in the upper airways. To avoid possible errors induced by the Newtonian fluid simplification, it is highly recommended to employ non-Newtonian fluid models rather than the idealized Newtonian fluid viscosity model (see Eqs. (4.5 (a)-(c))) when modeling mucus movement behaviors in the lung airway models. Since it has been confirmed in this section that the non-Newtonian fluid simulation are more realistic and accurate, only non-Newtonian fluid simulation results are discussed in the following sections for parametric analyses.

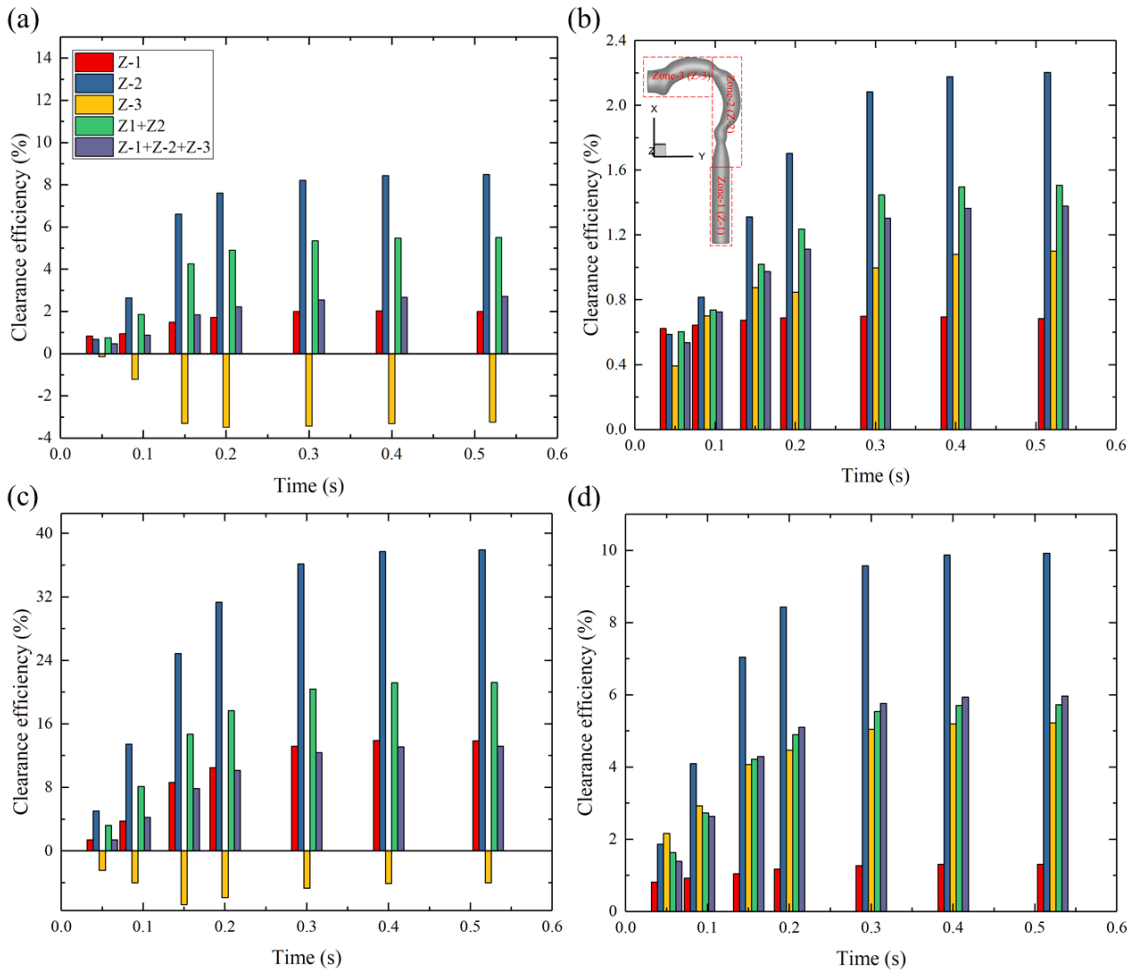

Figure 4.6 Mucus clearance efficiency in the MT model with Newtonian mucus under different conditions: (a) CS-I and $\sigma = 1.0\ mm$; (b) CS-I and $\sigma = 0.5\ mm$; (c) CS-II and $\sigma = 1.0\ mm$; (d) CS-II and $\sigma = 0.5\ mm$.

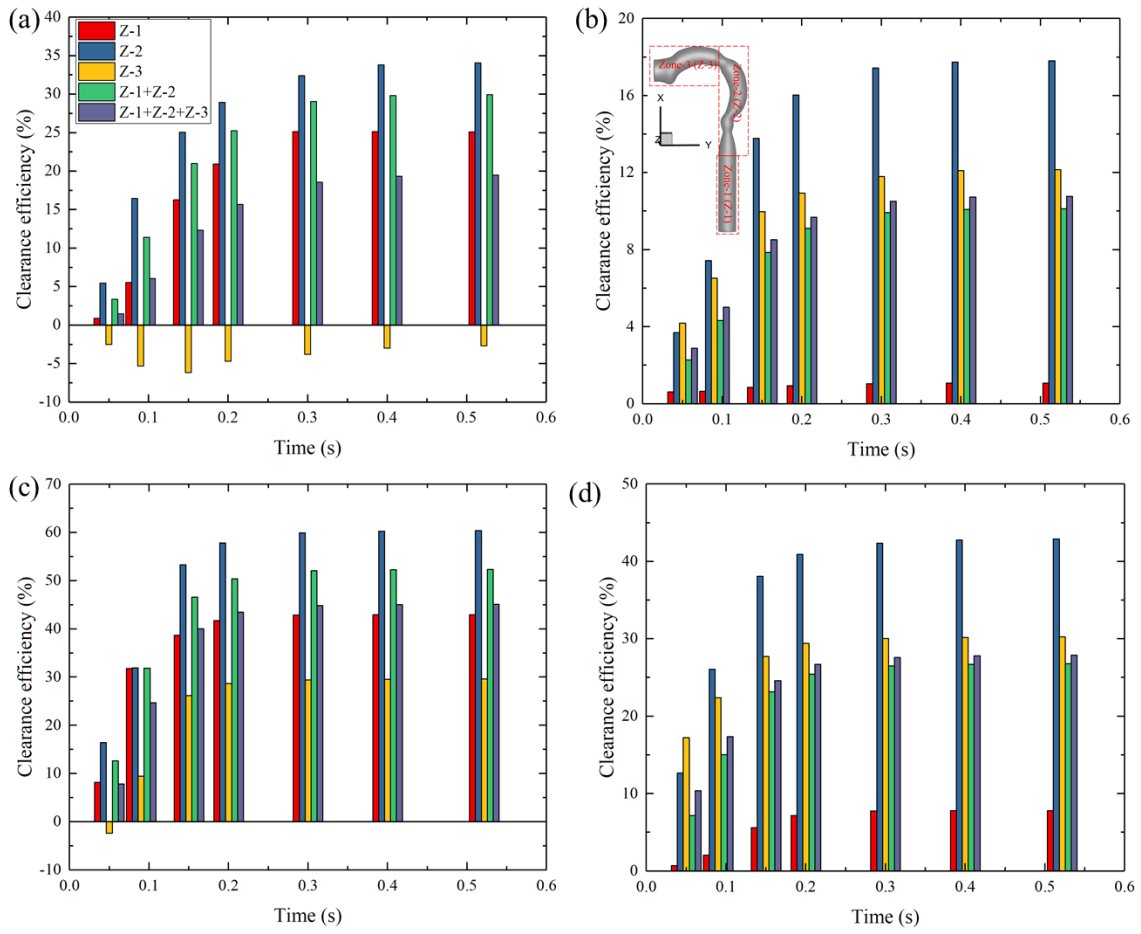

Figure 4.7 Mucus clearance efficiency in the MT model with non-Newtonian mucus under different conditions: (a) CS-I and $\sigma = 1.0\ mm$; (b) CS-I and $\sigma = 0.5\ mm$; (c) CS-II and $\sigma = 1.0\ mm$; (d) CS-II and $\sigma = 0.5\ mm$.

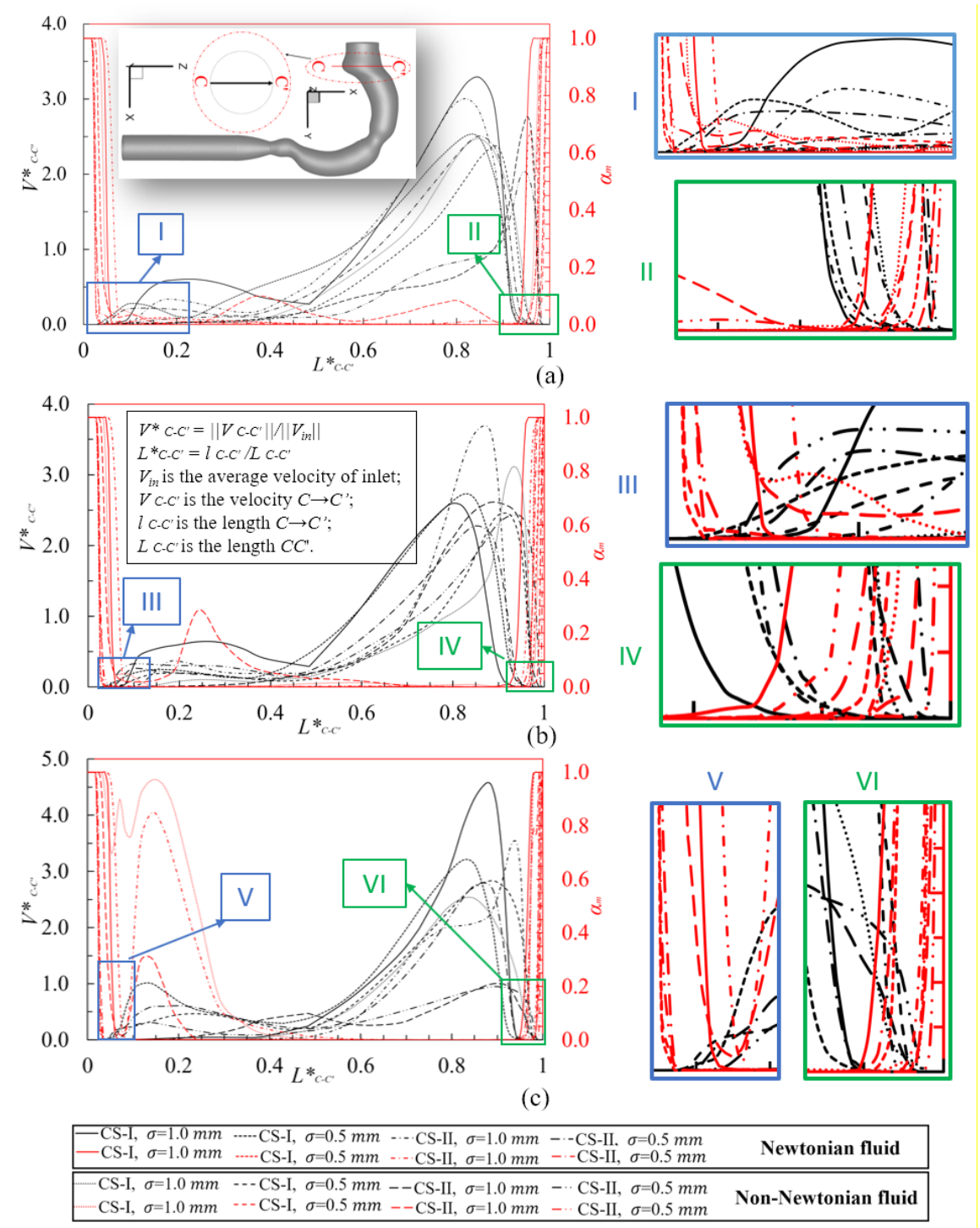

Figure 4.8 Nondimensionalized velocity profiles and mucus volume fraction at the cross-section C-C' computed with different cough strengths and mucus properties at different time stations in a cough-wave: (a) t = 0.05 *s*; (b) t = 0.09 *s*; (c) t = 0.40 *s*.

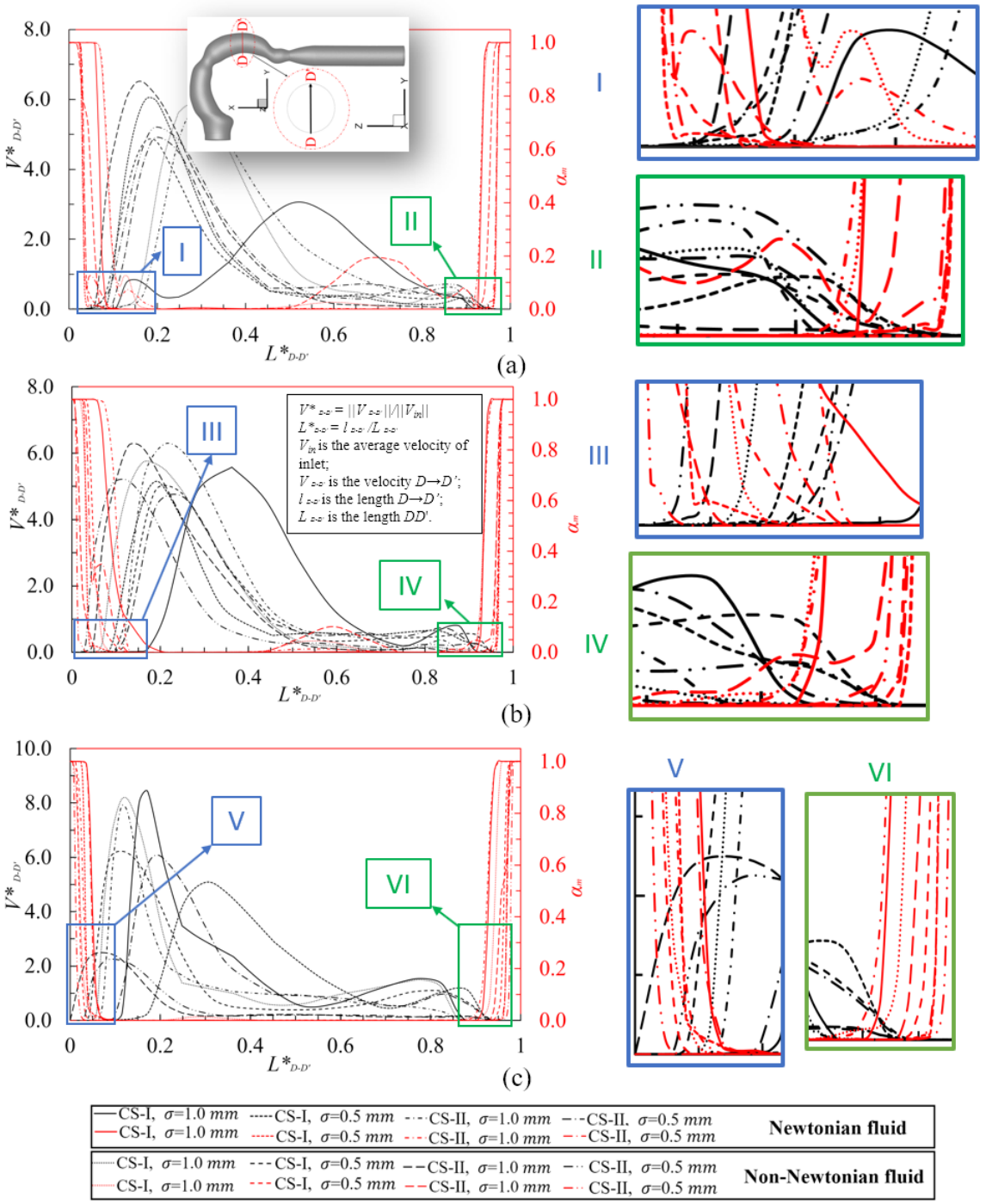

Figure 4.9 Nondimensionalized velocity profiles V^* and mucus volume fraction α_m at the cross-section D-D' computed with different cough strengths and mucus properties at different time stations in a cough-wave: (a) t = 0.05 s; (b) t = 0.09 s; (c) t = 0.40 s.

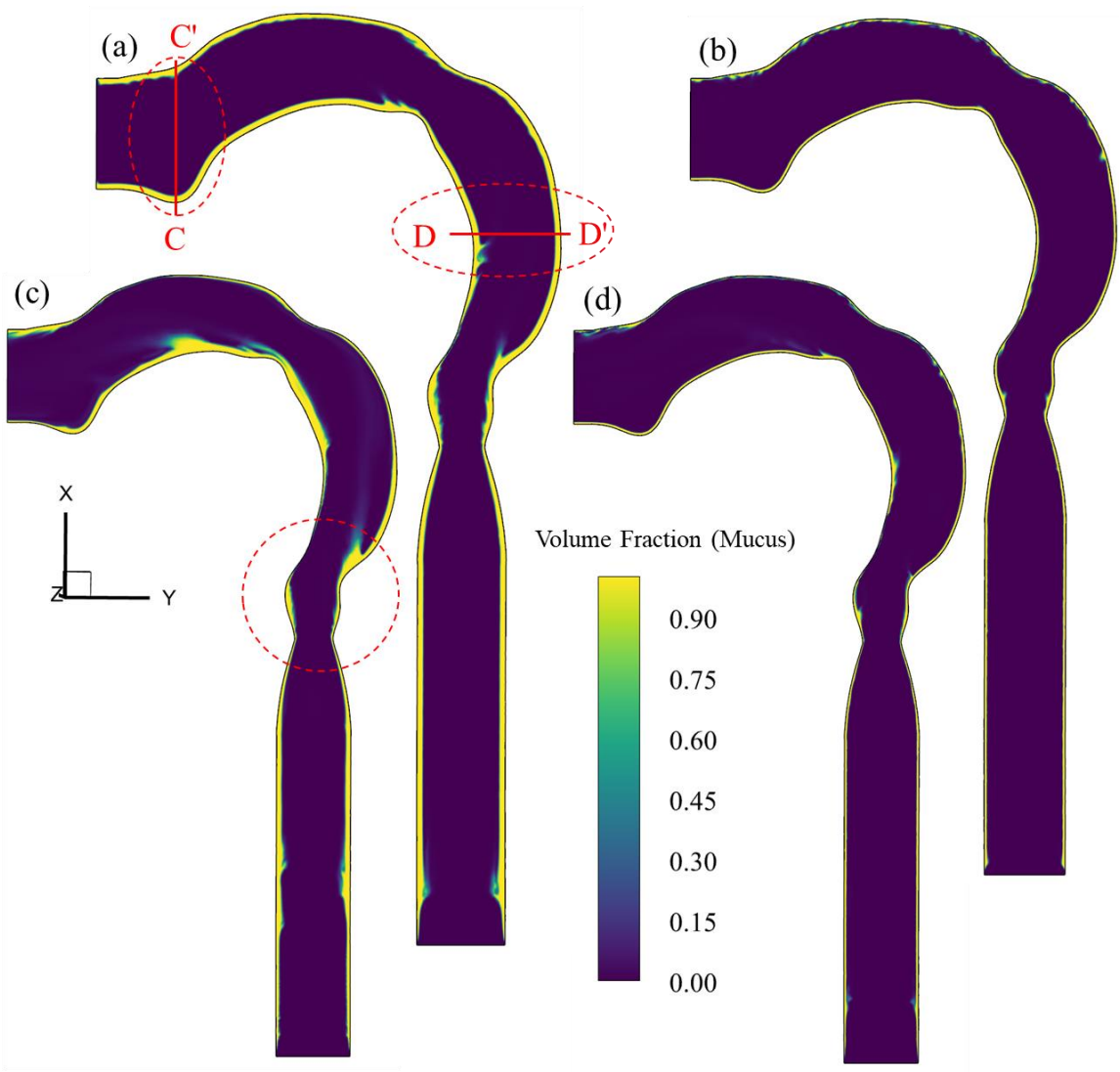

Figure 4.10 Mucus distributions in the sagittal plant (Z = 0) with CS-I at t = 0.09 s with different mucus thicknesses and mucus rheological properties: (a) $\sigma = 1.0\ mm$ with Newtonian fluid; (b) σ = 0.5 mm and Newtonian fluid; (c) $\sigma = 1.0\ mm$ and non-Newtonian fluid; (d) σ = 0.5 mm and non-Newtonian fluid.

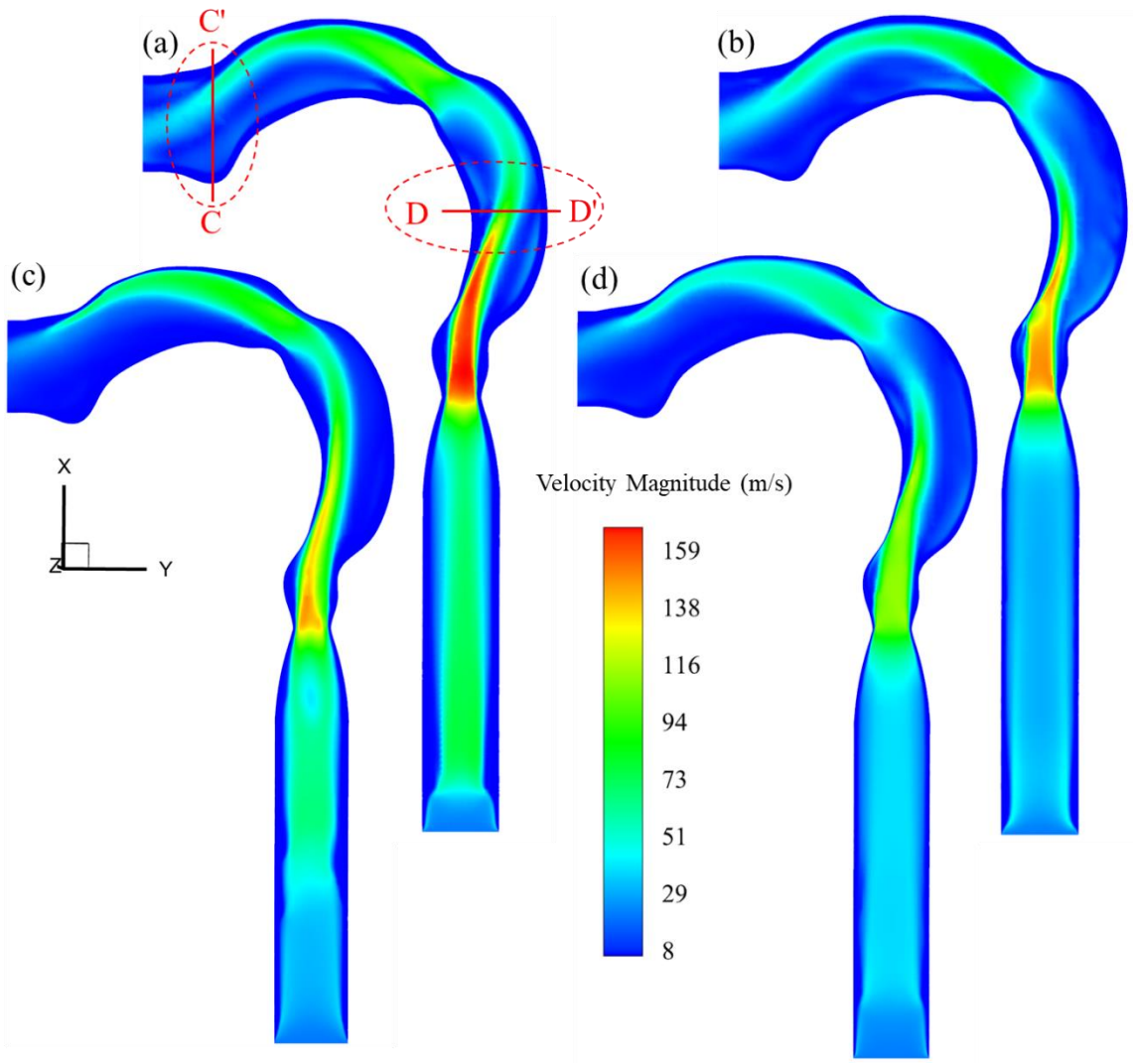

Figure 4.11 Velocity magnitudes in the sagittal plane (Z = 0) with CS-I at t = 0.09s (cough-wave peak) under different mucus thicknesses and mucus rheological properties: (a) $\sigma = 1.0\ mm$ with Newtonian fluid; (b) σ = 0.5 mm and Newtonian fluid; (c) $\sigma = 1.0\ mm$ and non-Newtonian fluid; (d) σ = 0.5 mm and non-Newtonian fluid.

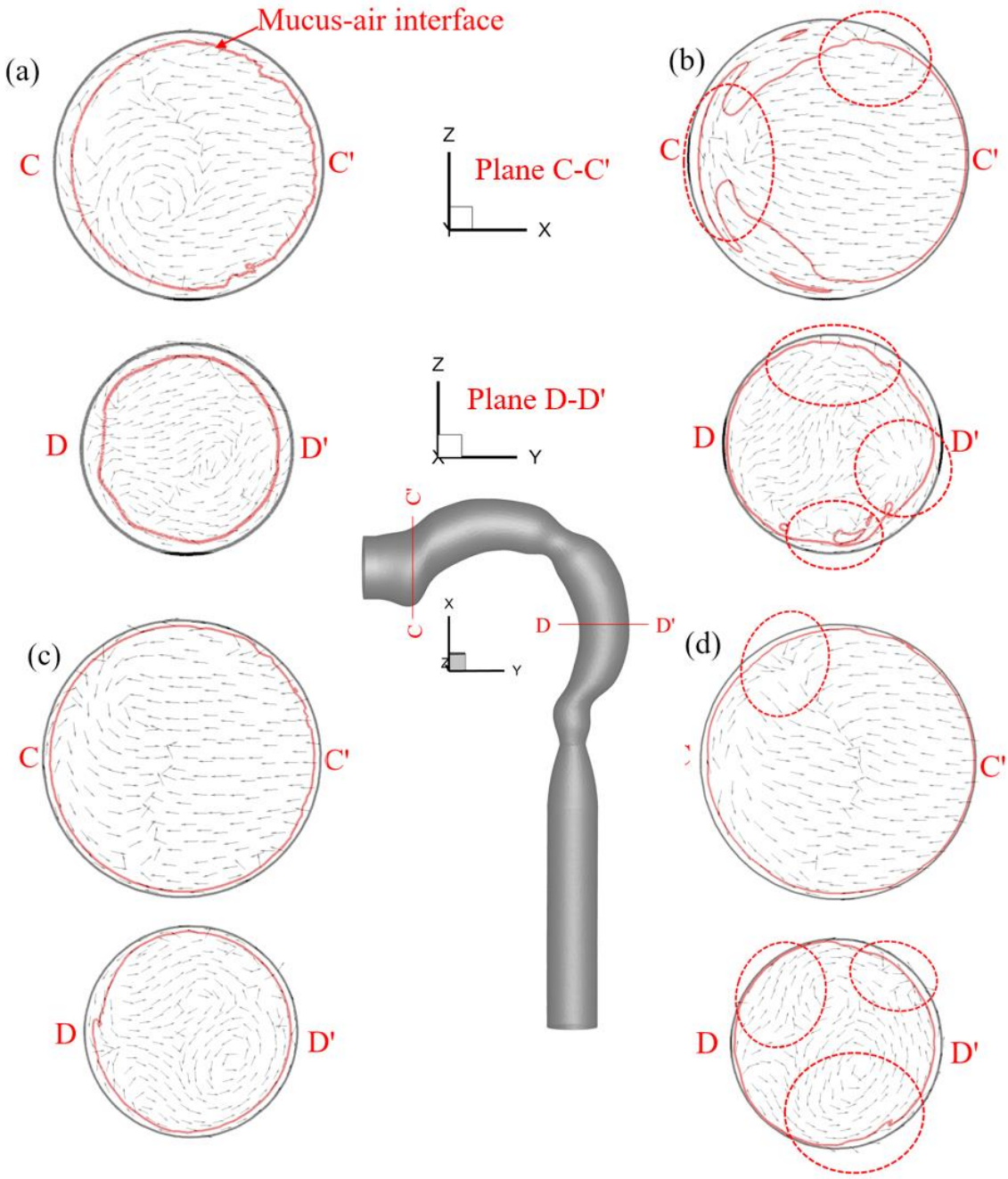

Figure. 4.12 Velocity vectors in selected planes C-C' and D-D' with CS I at $t = 0.09s$ with different mucus properties: (a) $\sigma = 1.0\ mm$ with Newtonian fluid; (b) $\sigma = 1.0\ mm$ and non-Newtonian fluid; (c) σ = 0.5 mm and Newtonian fluid; (d) σ = 0.5 mm and non-Newtonian fluid.

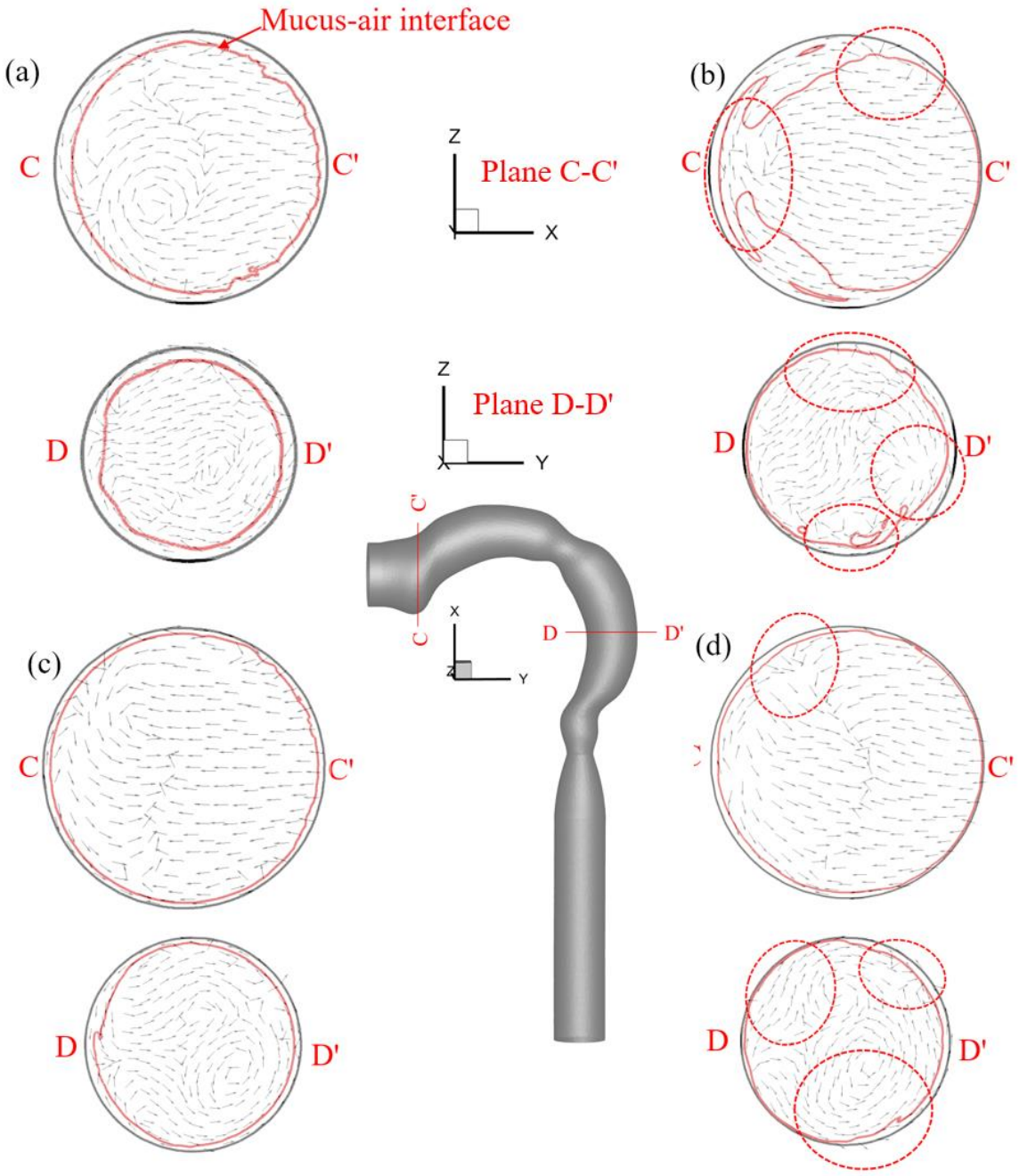

Figure 4.13 Velocity vectors in selected planes C-C' and D-D' with CS II at $t = 0.09s$ with different mucus characteristics: (a) $\sigma = 1.0\ mm$ with Newtonian fluid; (b) $\sigma = 1.0\ mm$ and non-Newtonian fluid; (c) σ = 0.5 mm and Newtonian fluid; (d) σ = 0.5 mm and non-Newtonian fluid.

Table 4.2 Average volumetric flow rate $\bar{q}_m$ (ml/s) in the selected time stations in a single cough.

Conditions			Time (s)						
Mucus thickness (mm)	Mucus viscosity $(Pa \cdot s)$	Cough strength	0.05	0.09	0.15	0.20	0.30	0.40	0.5126
1.0	7.9	CS-I	1.05	1.11	1.38	1.25	0.96	0.76	0.60
	1 ~ 14.8	CS-I	3.34	7.64	9.30	8.88	7.01	5.47	4.31
	7.9	CS-II	3.20	5.35	5.94	5.76	4.67	3.72	2.92
	1 ~ 14.8	CS-II	17.73	31.10	30.25	24.61	16.92	12.75	9.96
0.5	7.9	CS-I	0.58	0.43	0.35	0.30	0.24	0.19	0.15
	1 ~ 14.8	CS-I	3.14	3.03	3.09	2.63	1.90	1.46	1.14
	7.9	CS-II	1.77	1.65	1.53	1.33	1.00	0.76	0.60
	1 ~ 14.8	CS-II	11.27	10.49	8.92	7.26	5.00	3.78	2.96

Table 4.3 Mucus clearance efficiency (%) at selected time stations during a single cough

Conditions			Time (s)						
Mucus thickness (mm)	Mucus viscosity $(Pa \cdot s)$	Cough strength	0.05	0.09	0.15	0.20	0.30	0.40	0.5126
1.0	7.9	CS-I	0.46	0.88	1.84	2.22	2.55	2.67	2.71
	1 ~ 14.8		1.48	6.67	12.32	15.68	18.56	19.33	19.50
	7.9	CS-II	1.41	4.25	7.86	10.17	12.38	13.12	13.20
	1 ~ 14.8		7.83	24.71	40.07	43.47	44.82	45.03	45.08
0.5	7.9	CS-I	0.54	0.73	0.97	1.11	1.30	1.37	1.38
	1 ~ 14.8		2.89	5.02	8.52	9.69	10.51	10.73	10.77
	7.9	CS-II	1.63	2.73	4.22	4.90	5.54	5.70	5.73
	1 ~ 14.8		10.36	17.37	24.61	26.71	27.62	27.82	27.90

Table 4.4 Average mucus velocity $\bar{v}_m$ (m/s) at each across planes C-C' and D-D' in selected time stations.

Conditions				Side of interface at C-C' and D-D'			
Mucus thickness (mm)	Mucus viscosity $(Pa \cdot s)$	Cough strength	Time (s)	C	C'	D	D'
1.0	7.9	CS-I	0.05	0.0029	0.1739	0.01959	0.0048
			0.09	0.0047	0.3610	1.0864	0.0274
			0.40	0.0001	0.0013	0.0037	0.0004
	1 ~ 14.8		0.05	0.0010	1.2773	2.5962	0.03479
			0.09	0.04567	1.1141	11.8016	0.3814
			0.40	0.0293	0.07347	1.03245	0.0069
	7.9	CS-II	0.05	0.0061	1.3163	8.8395	0.1527
			0.09	0.0117	1.7271	11.4333	0.06409
			0.40	0.0771	0.08	0.0075	0.0007
	1 ~ 14.8		0.05	0.1522	8.5800	14.8327	1.0214
			0.09	0.2046	0.9130	8.6889	0.4422
			0.40	0.0024	0.0080	Not appliable	0.0070
0.5	7.9	CS-I	0.05	0.0074	0.2114	0.5570	0.2112
			0.09	0.0040	0.0480	0.2893	0.0111
			0.40	0.0004	0.0004	0.0015	0.0002
	1 ~ 14.8		0.05	0.0119	1.5842	1.2038	0.0682
			0.09	0.0175	2.270	0.9951	0.0375
			0.40	0.0002	0.0052	0.0067	0.0034
	7.9	CS-II	0.05	0.00332	1.0773	0.3384	0.0329
			0.09	0.0038	0.3119	0.4813	0.2182
			0.40	0.0002	0.0041	0.0065	0.0006
	1 ~ 14.8		0.05	0.0574	3.4777	2.8216	0.6093
			0.09	0.0166	1.0061	1.8391	0.2090
			0.40	0.00001	0.0001	0.0005	0.0001

4.5.3 Effects of Mucus Thickness

Two mucus thicknesses $\sigma = 1.0\ \ mm$ and $= 0.5\ \ mm$ were employed in this study to morphologically represent two COPD levels, i.e., GOLD I and GOLD II (see Figure 4.1) for investigating the mucus thickness effects on mucus clearance efficiency and transport behaviors. Figures 4.7 (a) & (c) are the regional mucus clearance efficiencies (η_{ce}) in the MT model with $\sigma = 1.0\ mm$, and Figures 4.7 (b) & (d) are η_{ce} values with $\sigma = 0.5\ mm$ during a single cough at different time stations. In addition, Table 4.3 lists the η_{ce} values at different times and shows that the maximum η_{ce} is 45.08%, which is with strong cough CS-II and $\sigma = 1.0\ mm$, and the minimum η_{ce} is 10.77%, which is with mild cough CS-I and $\sigma = 0.5\ mm$. Comparisons between Figure 4.6 and Figure 4.7 demonstrate that with the same cough waveform, the upper airway model with thicker mucus generates higher mucus clearance efficiency. Specifically, with the same cough waveform, η_{ce} in the MT model with $\sigma = 1.0\ mm$ is about 2 times of the η_{ce} value in the MT model with $\sigma = 0.5\ mm$. The higher η_{ce} is because the average mucus volumetric flow rate $\bar{q}_m$ with $\sigma = 1.0\ \ mm$ is approximately 4 times of $\bar{q}_m$ with $\sigma = 0.5\ \ mm$ (see Table 4.2). Indeed, although when cough strengths are the same, thicker mucus can lead to smaller lumen for the airflow. The smaller lumen can lead to a higher velocity gradient and shear-stress at the mucus-air interfaces (see Figures. 4.11 (c) & (d), 4.15 (c) & (d)). As an example of the evidence to support the abovementioned underlying fluid dynamics, the average mucus velocity $\bar{v}_m$ in the upper airway with $\sigma = 1.0\ mm$ is higher than $\bar{v}_m$ in the simulation results with $\sigma = 0.5\ mm$ (see Figures 4.8 & 4.9 and Table 4.4).

It can be also found that the mucus layer thickness varies spatially in different regions (i.e., Z-1, Z-2, and Z-3), during the clearance process driven by the coughs (see Figures 4.7, 4.10, 4.14, and 4.16). Mucus can be accumulated and entrapped in Z-3 with more severity level (see R-1 to R-3 in Figures 4.16 (a) and (b)), especially under the condition with CS-I that the clearance efficiencies are negative at all selected time stations (see Figure 4.7). Such accumulation effect in Z-3 is because

the mucus in Z-1 and Z-2 can move into Z-3 easily, but not be able to move further to the mouth front due to the combined effect of gravity and low airflow momentum (see Figures 4.11 (c), 4.11 (d), 4.15 (c), and 4.15 (d)). In contrast, with $\sigma = 0.5\ mm$, the mucus thickness distribution is more even and has no distinguished changes in the submandibular region (see R-3 in Figures 4.16 (c) & (d)), which indicates no accumulation of the mucus in Z-3 during the expiratory cough when the COPD condition is not severe.

Moreover, it has been commonly recognized that mucus can be easily spat out from the mouth by moving the oral muscles if mucus can be transported through the throat from the trachea to the oral region (Gavião & Bilt, 2004; Hewitt, Smeeth, Bulpitt, Tulloch, & Fletcher, 2005). Thus, the total mucus clearance efficiency in Z-1 and Z-2 may be more informative to represent the difficulty of mucus clearance than the entire MT model. However, it is interesting to find that with mild COPD condition (i.e., $\sigma = 0.5\ mm$), the clearance efficiency in the entire MT model is higher than the total of Z-1 and Z-2 (see Figures 4.7 (b) & (d)). It is due to the volume of mucus feeding into Z-3 is less than the amount cleared out from this region, implying that the viscosity resistance plays a more significant role on the mucus transport behaviors.

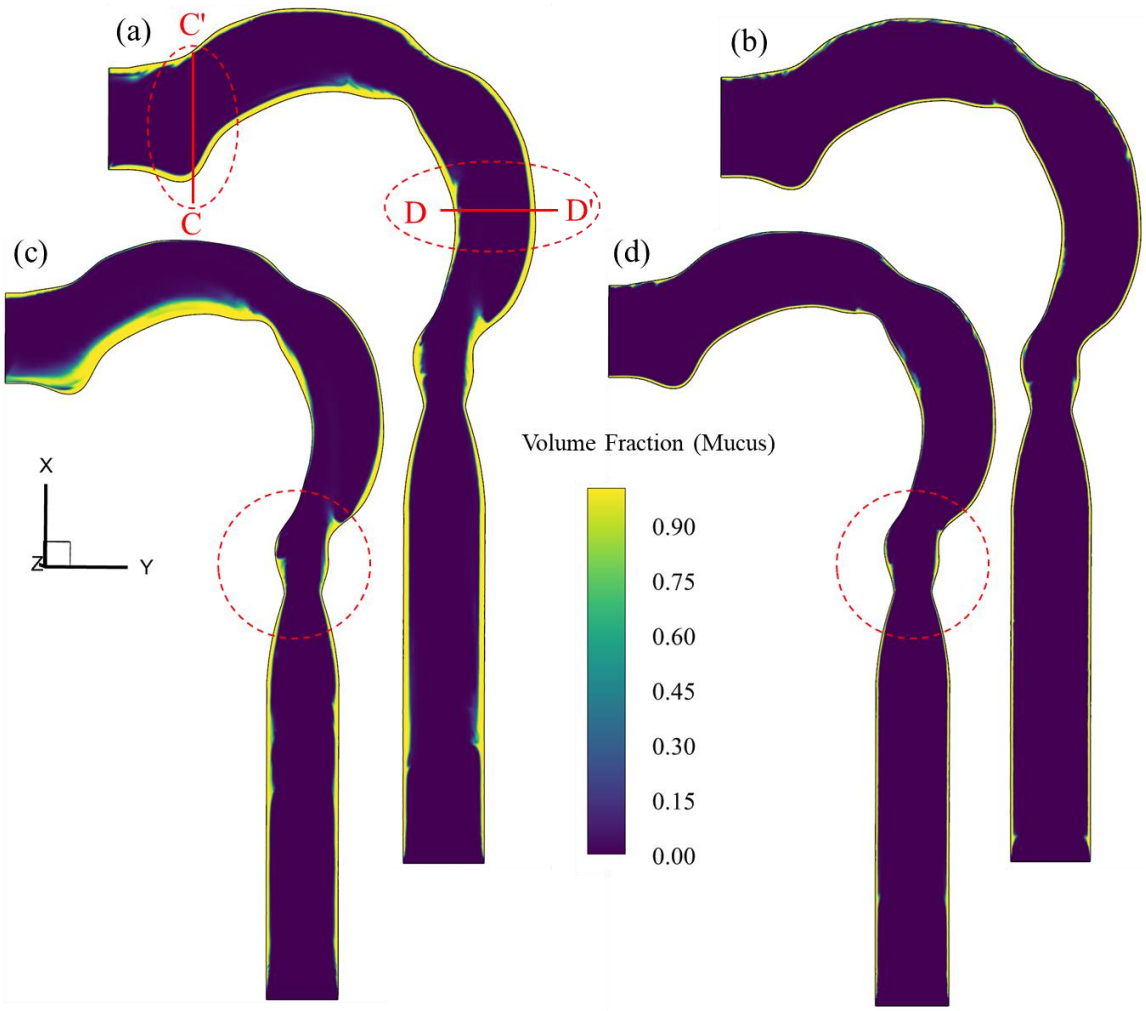

Figure 4.14 Mucus distributions in the sagittal plane (Z = 0) with CS-I at t = 0.40s under different mucus thicknesses and mucus rheological properties: (a) $\sigma = 1.0\ mm$ with Newtonian fluid; (b) $\sigma = 0.5\ mm$ and Newtonian fluid; (c) $\sigma = 1.0\ mm$ and non-Newtonian fluid; (d) $\sigma = 0.5\ mm$ and non-Newtonian fluid.

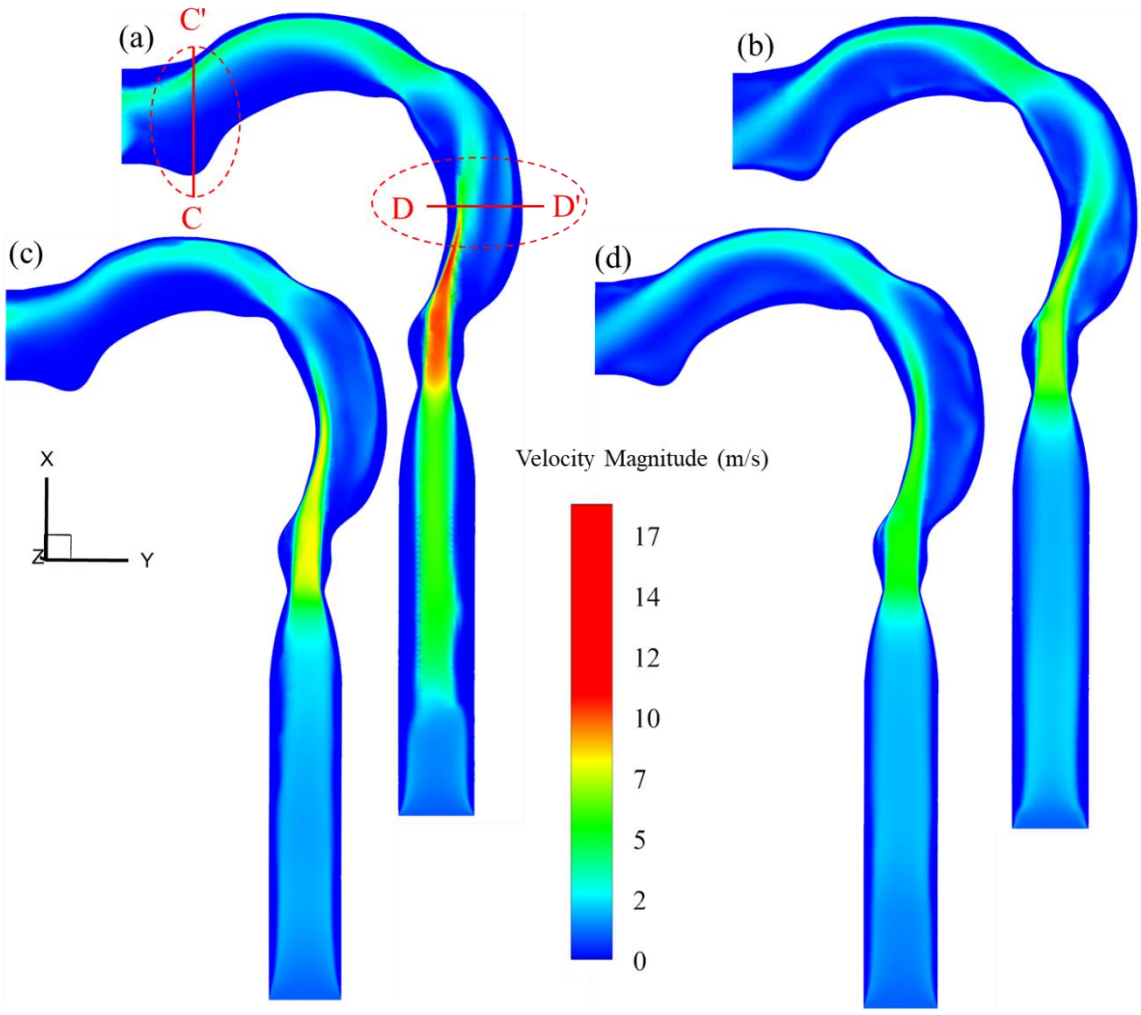

Figure 4.15 Velocity magnitudes in the sagittal plane (Z = 0) with CS-II at t = 0.40s (cough-wave peak) under different mucus thicknesses and mucus rheological properties: (a) $\sigma = 1.0$ mm with Newtonian fluid; (b) $\sigma = 0.5$ mm and Newtonian mucus; (c) $\sigma = 1.0$ mm and non-Newtonian mucus; (d) $\sigma = 0.5$ mm and non-Newtonian fluid.

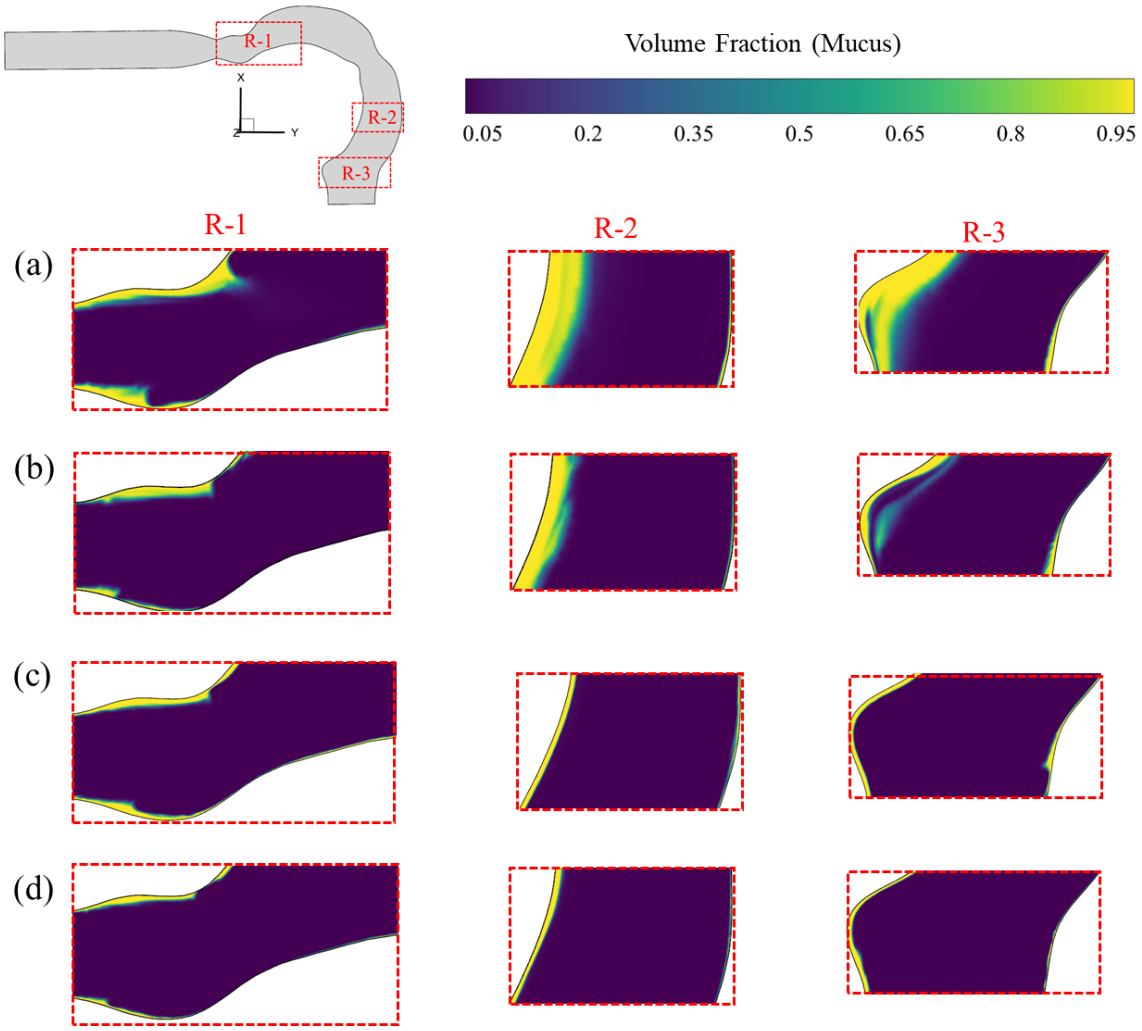

Figure 4.16 Distributions of non-Newtonian mucus in different regions (t = 0.5126 s): (a) $\sigma = 1.0\ mm$ and CS-I; (b) $\sigma = 1.0\ mm$ and CS-II; (c) $\sigma = 0.5\ mm$ and CS-I; (d) $\sigma = 0.5\ mm$ and CS-II.

Table 4.5 Mucus clearance efficiency (%) in non-Newtonian fluid simulations at Z-1 during a single cough.

Conditions		Time (s)						
Mucus thickness (mm)	Cough strength	0.05	0.09	0.15	0.20	0.30	0.40	0.5126
1.0	CS-I	0.87	5.54	16.26	20.92	25.11	25.13	25.09
	CS-II	8.19	31.78	38.69	41.71	42.86	42.92	42.91
0.5	CS-I	0.61	0.64	0.86	0.94	1.05	1.08	1.07
	CS-II	0.71	2.04	5.59	7.18	7.78	7.80	7.79

4.5.4 Effects of Cough Strength

Two cough waveforms, i.e., CS-I and CS-II, representing two different cough strengths (see Figure 4. 4) with the relationship of $q_{CS-I} = 1/2 q_{CS-II}$, were employed to investigate its effects on mucus clearance efficiency. The mucus clearance efficiencies shown in Figure 4.7 imply that cough intensity plays a critical role on mucus clearance efficiency and mucus movement behaviors. Specifically, stronger cough (CS-II) can enhance the clearance efficiency, which is aligned with previous studies in idealized tracheas and bifurcated airways (C. S. Kim, Greene, et al., 1986; C. S. Kim et al., 1987; C. S. Kim, Rodriguez, et al., 1986; Ren et al., 2020). The mucus clearance efficiencies in the MT model with CS-II are 2.31 and 2.51 times higher than CS-I in two COPD severity levels, i.e., GOLD I and GOLD II, respectively (see Table 4.3). In addition, the cough intensity can affect the mucus distribution in the upper airways significantly (see Figures 4.12 (b), 4.12 (d), 4.13 (b), and 4.13 (d)). Figure 4.7 shows that a stronger cough can help COPD patients to carry the secreted mucus from the trachea to the oral cavity. Such a phenomenon is more apparent in the upper airways with the thicker mucus condition. Indeed, the mucus initially in the trachea and the oropharynx (Z-1 and Z-2) moved into the oral cavity (Z-3). Therefore, mucus

accumulations are formed in the oral cavity, which causes decreases in clearance efficiency in Z-3 (see Figure 4.7). Furthermore, as shown in highlighted regions of planes C-C' and D-D' in Figures 4.9 & 4.10, the stronger cough can generate a thinner mucus layer due to the higher shear rate at the mucus-air interface that could be developed by higher expiratory airflow velocity. Comparisons between Figure 4.7 (a) and Figure 4.7 (b) show that the mucus can overcome the gravity and viscous force in Z-1 when the expiratory airflow rate is higher than 6.59 L/s and avoid the mucus accumulation from Z-1 and Z-2 in this region with $\sigma = 1.0\ mm$. This observation is supported by mucus volume fraction contours shown in Figures 4.16 (a) & (b).

However, the mucus in the right side of the supraglottic region and the oropharynx (see highlighted circled region in Figures 4.14 (c) & (d), as well as R-1 and R-2 in Figure 4.16 are cleared by the increased expiratory airflow. Such fast removal could lead to direct exposure of the airway to inhaled air, toxicants, and virus-laden droplets without the protection of mucus. It may cause potential damages to the airway tissue and enhanced exposure risks. Thus, attention should be paid when the COPD patients develop intense cough strength to assist mucus clearance in pulmonary airways.

4.5.5 Mucus Rheology Driven by Transient Expiratory Airflows

During a single cough (see Figure 4.4), the airflow driven mucus clearance varies with time. Specifically, since the air velocity increases sharply to the maximum at $t = 0.09\ s$, and then decreases from 0.09 s to 0.40 s, the clearance efficiency (see Figure 4.7) increases rapidly till $t = 0.09\ s$,, while the growth rate tends to slow down after $t = 0.40\ s$. It can be explained by the fact that the larger shear stress produced by higher velocities around the cough peak can carry the mucus faster than at the time when airflow velocity is low. In all selected time stations (see Table 4.3), i.e., t = 0.05 s, 0.09 s, 0.15 s, 0.20 s, 0.30 s, 0.40 s, and 0.5126 s, the mucus was cleared more

efficiently with CS-II and $\sigma = 1.0\ mm$, which is also due to the high expiratory airflows (also see Section 4.5.3 and 4.5.4).

Additionally, gravity also has a noticeable impact on the mucus transport and clearance, which can be observed apparently from the clearance efficiency in Z-1 from $t = 0.40\ s$ to the end of the cough (see Table 4.5 and Figure 4.7). Specifically, the mucus clearance efficiency in Z-1 decreases from $t = 0.40\ s$ to $t = 0.5126\ s$. The decline in mucus clearance efficiency is because of the reversed flow from the upper airway to the trachea (i.e., from Z-2 back to Z-1) driven by the gravitational force. Therefore, reasonably intense expiratory airflow is needed to overcome gravity and to enhance the mucus clearance efficiency, although it will be difficult to achieve for severe COPD patients.

4.6 Summary

The effects of the mucus viscosity model, cough strength, and mucus thickness on the airflow-driven COPD mucus clearance process have been studied systematically in this chapter using an experimentally validated VOF model. Quantitative conclusions are listed as follows:

- Using the Newtonian fluid viscosity model for mucus can significantly underpredict in mucus transport velocity and clearance, compared with the numerical results using realistic shear-thinning non-Newtonian fluid viscosity model. Therefore, it is highly recommended to model the mucus as a shear-thinning non-Newtonian fluid, rather than to simplify it as a Newtonian fluid.
- The cough intensity plays a critical role in affecting mucus movement and clearance, i.e., the higher cough flow rate can increase the mucus clearance efficiency in the upper airway.
- Although higher mucus clearance efficiency is observed for severe COPD condition with thicker mucus layer, there is a possibility of mucus accumulation and obstruction in the

upper airway for such COPD condition if the cough is not strong enough, which will possibly cause further breathing difficulty.

4.7 Limitation of Current Study and Future Work

This study is not able to simulate the cilia motion and the driven mucus transport phenomena explicitly or realistically. Accordingly, the feasible modeling strategy as the future work is to build a VOF plus Discrete Phase Model (VOF-DPM) (more detailed introduction in Chapter V) with moving boundary conditions, to explicitly model how cilia beats can drive the mucus, and track the air-mucus mixture, and trace the mucus clearance effect with the explicit tracking of inhaled particle transport in pulmonary airflow and mucus. The moving wall boundary conditions, i.e., the transient cilia beating velocities, can be applied, following the physiologically realistic beating patterns (Gueron & Levit-Gurevich, 1998; D. Smith, E. Gaffney, & J. Blake, 2008). The cilia velocity can be given in the form of a Fourier series (Fulford & Blake, 1986).

CHAPTER V

CONCLUSIONS AND FUTURE WORK

5.1 Conclusions

The research objectives (i.e., Aim I, Aim II, and Aim III) outlined in Chapter I have been fulfilled. A systematic study has been conducted to investigate the mechanisms of large LPG pool fires and mucus transport phenomena in upper lung airways using CFD methods. The discovered results from this work can not only directly improve fundamental understandings of large LPG pool fires, but also help us to better recognize the mucus transport dynamics in the respiratory system, which can assist us in building a more physiologically environment to assess health risks from LPG pool fires to human lung airways. Based on the summaries (i.e., Sections 2.6, 3.6, and 4.6) from Chapter II to Chapter IV, major conclusions are summarized as follows:

5.1.1 Heat Radiation from Large Liquefied Petroleum Gas Pool Fires

An experimentally validated CFD model was developed to investigate the surface emissive power and incidentally radiative heat flux from large LPG pool fires. Simulation results were compared with existing experimental values and previous correlations, and several quantitative conclusions

were achieved as follows:

- With the advantages of P-1 radiation model and non-premixed combustion model, it is more reliable and accurate to describe the scenarios of large LPG pool fires than empirical correlations.
- Based on the empirical models and experimental data, a new correlation for SEP in LPG (100% propane) pool fire (10 m $\leq D \leq$ 20 m) has been proposed, which provides better prediction accuracies than existing models.
- CFD simulations show that the airflow conditions have less impact on maximum and average incident radiations to the surrounding individuals and structures, which are determined by the burning rate.
- The airflow condition can have significant impacts on the distribution of incident radiation in the same iso-surface, and it would tilt to wind direction because radiative heat flux distribution is determined by the flame configuration.
- Based on available results from CFD simulations, the safe separation distances have been suggested under the requirements of different codes.

5.1.2 Configurations of Large Liquefied Petroleum Gas Pool Fires

Employing the developed CFD model in Chapter I to investigate the characteristics of large LPG pool fires by integrating the limited experimental tests, several conclusions can be obtained as follows:

- The selection of the burning rate model can significantly influence the accuracy of flame height predictions using the CFD model. Johnson's burning rate model is the best model among the three burning rate models employed in this study.
- Higher horizontal wind velocity will lead to stronger convection effect in the horizontal direction. As a result, it will reduce the flame height and increase the flame tilt angle.

- The configuration of LPG pool fires with larger diameters will be less sensitive to the ambient wind velocity.
- The new correlations proposed in this study provide more accurate predictions of the flame height and tilt angle than any existing empirical models. The two correlations will facilitate engineers and scientists when estimating the flame configurations for large LPG pool fires with pool diameters between 10 m and 20 m, and ambient wind velocity between 0 and 3 m/s.
- With the enhanced fundamental understandings and the new proposed correlations of flame height and tilt, the numerical study and parametric analysis can be further employed to facilitate the precise risk assessment for large LPG pool fires in a time-saving and cost-effective manner.

5.1.3 Lung Disease Effect on the Cough-Driven Mucus Movement and Clearance in an Idealized Upper Airway Model

Using an experimentally validated VOF model to systematically investigate airflow-driven COPD mucus clearance process under different conditions, quantitative conclusions are listed as below:

- Using the Newtonian fluid viscosity model for mucus can significantly underpredict in mucus transport velocity and clearance, compared with the numerical results using realistic shear-thinning non-Newtonian fluid viscosity model. Therefore, it is highly recommended to model the mucus as a shear-thinning non-Newtonian fluid rather than to simplify it as a Newtonian fluid.
- The cough intensity plays a critical role in affecting mucus movement and clearance, i.e., the higher cough flow rate can increase the mucus clearance efficiency in the upper airway.
- Although higher mucus clearance efficiency is observed for severe COPD condition with thicker mucus layer, there is a possibility of mucus accumulation and obstruction in the

upper airway for such COPD condition if the cough is not strong enough, which will possibly cause further breathing difficulty.

5.2 Novel Contributions

The novel research contributions of this study can be summarized in the following:

- An alternative computational method is developed to complement experimental approaches to investigate the mechanisms of large LPG pool fires.
- Proposed safe separation distances to satisfy the requirements of different codes using the developed CFD model.
- A new correlation for the surface emissive power in LPG (100% propane) pool fire (10 m $\leqslant$ D $\leqslant$ 20 m) with fewer relative errors than other empirical models.
- Two new correlations for the flame height and tilt angle for large LPG pool fires contributing more accurate predictions than any existing empirical models.
- The general mechanism of cough-driven mucus clearance and transport behaviors to assist other researchers and scientists to build a more physiologically realistic upper airway model which can predict the clearance and transport behaviors of the toxic matters and hot temperature air in a large LPG pool fire scenario.

5.3 Future Directions

Our long-term goal is to develop an all-in-one computational modeling framework to quantitatively assess the fate of high-temperature air and toxic matters from their generation and ambient transmission to the transport and deposition in the human respiratory system. The generated aerosolized toxicants and emitted heat flux by fire have potential risks to the nearby firefighters and residents (Ahn & Jeong, 2015; Brandt-Rauf, Cosman, Fallon, Tarantini, & Idema, 1989; Brandt-Rauf, Fallon, Tarantini, Idema, & Andrews, 1988; Caban-Martinez et al., 2018; Chean, Abdulrahman, Chan, & Tan, 2019; Chia, Jeyaratnam, Chan, & Lim, 1990; Demers, Heyer, &

Rosenstock, 1992; Easterling & Prince, 2007; Hansen, 1990; Hong, Park, & Ha, 2000; Y. T. Kim et al., 2020; Neitzel, Hong, Quinlan, & Hulea, 2013; Rosénstock, Demers, Heyer, & Barnhart, 1990; Shusterman, Kaplan, & Canabarro, 1993). Specifically, exposure to the toxic matter poses severe health threats to individuals as the toxic components can cause respiratory diseases, neurological ailments, and ultimately cancer (Hannu, Piipari, Tuppurainen, Nordman, & Tuomi, 2007; Sjögren, Hansen, Kjuus, & Persson, 1994; Zhao et al., 2019). The most common toxic gases, i.e., nitrous oxides (NO_x) and carbon monoxide (CO) emitted from inadequate combustion of LPG pool fires, can cause respiratory disorders, such as increased inflammation of the airways and reduced lung function (Chitano, Hosselet, Mapp, & Fabbri, 1995; De Flora, 2000; Kampa & Castanas, 2008). Therefore, the fire departments should have a clear risk control plan in place with adequate information about the transport mechanisms of generated toxicants to respiratory airways for the people close to a fire. Although several methods are available to test real-time experiments which present transient exposure measurements (Pires, Quintino, Amaral, & Rosado, 2010; J. Wang, Hoang, Floyd, & Regens, 2017), it is still challenging to carry out observations and measurements on regional and local lung deposition *in vivo* due to the limitations of imaging resolution and operational flexibilities (Brand et al., 2013; Graczyk et al., 2016; Tian, Hindle, Lee, & Longest, 2015; Zhao et al., 2019). CFPD based models that overcome the drawbacks of the conventional investigating methods can provide informative high-resolution deposition data based on the natural laws of physics in a noninvasive manner (Utzinger, 2004). Various studies have been done for the development of CFPD models to predict the transport and deposition behaviors of particles and vapors in idealized and subject-specific human respiratory systems (Calmet et al., 2018; J. Feng & Xu, 2014; Haghnegahdar, Feng, Chen, & Lin, 2018; Y. H. Kim, Tong, Chan, & Yang, 2019; Kolanjiyil & Kleinstreuer, 2017; Koullapis, Nicolaou, & Kassinos, 2018; Lambert, O'Shaughnessy, Tawhai, Hoffman, & Lin, 2011; Longest et al., 2019; Xi et al., 2016; Xu, Shang, Tian, Weng, & Tu, 2018; Zhang, Kleinstreuer, & Hyun, 2012; Zhao et al., 2019), which have

confirmed that CFPD can be an available method to investigate transport dynamics of health threatened matter in lung airways by a fire. Thus, to achieve the long-term goal, future work can be conducted based on the following tentative plans:

5.3.1 Predict the Distributions of Generated Toxic Gases and Heat Flux by a LPG Pool Fire in an Indoor Environment

Using the CFD model (Yi et al., 2020; Yi et al., 2019) developed in Chapters II and III, we can employ the non-premixed combustion model with PDF table (Pope, 1985) to compute concentration distributions of carbon monoxide (CO) and other matters generated from an LPG pool fire. We can use the P1 model (Eby, Trépanier, & Zhang, 1998) to obtain the heat flux distribution from the LPG pool fire in a virtual indoor space. The results from this work will provide the boundary conditions information of heat intensity and toxic gas concentrations for the work in Section 5.3.2.

5.3.2 Predictions of the Transport and Deposition of Toxic Gases, as well as the Heat Transfer in a Representative Human Respiratory System

Using the gas emitted concentration and heat flux obtained from Section 5.3.1, the VOF-DPM model can be employed to track the transport, deposition, and clearance of the toxic particles/gases and heat source in a representative human respiratory system. The deposition behaviors of the toxicant concentration distributions in human respiratory systems should be investigated comprehensively. Specifically, we can try to obtain heat and toxicant concentrations distributions at any specific location in the idealized airways using the CFD method. Also, a tentative parametric study can be conducted to better understand the mechanisms of factors, i.e., mucus thickness, mucus viscosity, breathing patterns, toxic gas concentration, and air temperature, which may influence the transport behaviors of heat and toxic gases in lung airways intensively.

REFERENCES

49CFR. (2018). Liquefied natural gas facilities, Part 193.

A. Croce, P., & Mudan, K. S. (1986). Calculating impacts for large open hydrocarbon fires. *Fire Safety Journal, 11*(1), 99-112. doi:https://doi.org/10.1016/0379-7112(86)90055-X

A.G.A. (1974). *LNG safety research program* (Report IS 3-1). Retrieved from

Ahn, Y.-S., & Jeong, K. S. (2015). Mortality due to malignant and non-malignant diseases in Korean professional emergency responders. *Plos One, 10*(3), e0120305-e0120305. doi:10.1371/journal.pone.0120305

Antonov, A. N., & Bondarev, E. N. (1968). Approximate method for calculating turbulent boundary layer with positive pressure gradient. *Fluid Dynamics, 3*(1), 41-42. doi:10.1007/BF01016234

API-Standard521. (2014). Pressure-relieving and depressuring systems (6th ed.).

Attar, A. A., Pourmanhdian, M., Anvaripour, P. . (2013). Experimental study and CFD simulation of pool fires. *International Journal of Computer Applications, 70*(11), 9-15.

Aurell, J., Gullett, B. K., Tabor, D., Williams, R. K., Mitchell, W., & Kemme, M. R. (2015). Aerostat-based sampling of emissions from open burning and open detonation of military ordnance. *Journal of Hazardous Materials, 284*, 108-120. doi:https://doi.org/10.1016/j.jhazmat.2014.10.029

Aurell, J., Hubble, D., Gullett, B. K., Holder, A., Washburn, E., & Tabor, D. (2017). Characterization of Emissions from Liquid Fuel and Propane Open Burns. *Fire technology, 53*(6), 2023-2038. doi:10.1007/s10694-017-0670-2

Babrauskas, V. (1983). Estimating large pool fire burning rate. *Fire technology, 19(4)*, 251-261.

Babrauskas, V. (2002). *Heat release rate. SFPE handbook of fire protection engineering (3rd ed.)* (Vol. Section 3). MA: National Fire Protection Association.

Bariha, N., Srivastava Vimal, C., & Mishra Indra, M. (2017). Theoretical and experimental studies on hazard analysis of LPG/LNG release: a review. In *Reviews in Chemical Engineering* (Vol. 33, pp. 387).

Basser, P. J., McMahon, T. A., & Griffith, P. (1989). The mechanism of mucus clearance in cough. *Journal of Biomechanical Engineering-Transactions of the Asme, 111*(4), 288-297. doi:10.1115/1.3168381

Blinov, V. I., & Khudiakov, G. N. (1957). Certain laws governing the diffusive burning of liquids. *Academiia Nauk, SSR Doklady, 113*, 1094-1098. Retrieved from https://ci.nii.ac.jp/naid/10018472696/en/

Brackbill, J. U., Kothe, D. B., & Zemach, C. (1992). A continuum method for modeling surface tension. *Journal of Computational Physics, 100*(2), 335-354. doi:https://doi.org/10.1016/0021-9991(92)90240-Y

Brand, P., Bischof, K., Siry, L., Bertram, J., Schettgen, T., Reisgen, U., . . . Gube, M. (2013). Exposure of healthy subjects with emissions from a gas metal arc welding process: Part 3 - Biological effect markers and lung function. *International Archives of Occupational and Environmental Health, 86*(1), 39-45. doi:10.1007/s00420-012-0740-1

Brandt-Rauf, P. W., Cosman, B., Fallon, L. F., Jr., Tarantini, T., & Idema, C. (1989). Health hazards of firefighters: acute pulmonary effects after toxic exposures. *British journal of industrial medicine, 46*(3), 209-211. doi:10.1136/oem.46.3.209

Brandt-Rauf, P. W., Fallon, L. F., Jr., Tarantini, T., Idema, C., & Andrews, L. (1988). Health hazards of fire fighters: exposure assessment. *British journal of industrial medicine, 45*(9), 606-612. doi:10.1136/oem.45.9.606

Button, B., & Boucher, R. C. (2008). Role of mechanical stress in regulating airway surface hydration and mucus clearance rates. *Respiratory Physiology & Neurobiology, 163*(1-3), 189-201. doi:10.1016/j.resp.2008.04.020

Caban-Martinez, A. J., Kropa, B., Niemczyk, N., Moore, K. J., Baum, J., Solle, N. S., . . . Kobetz, E. N. (2018). The "Warm Zone" Cases: Environmental Monitoring Immediately Outside the Fire Incident Response Arena by Firefighters. *Safety and health at work, 9*(3), 352-355. doi:10.1016/j.shaw.2017.12.003

Calmet, H., Kleinstreuer, C., Houzeaux, G., Kolanjiyil, A. V., Lehmkuhl, O., Olivares, E., & Vázquez, M. (2018). Subject-variability effects on micron particle deposition in human nasal cavities. *Journal of Aerosol Science, 115*, 12-28. doi:https://doi.org/10.1016/j.jaerosci.2017.10.008

Camassa, R., Forest, M. G., Lee, L., Ogrosky, H. R., & Olander, J. (2012). Ring waves as a mass transport mechanism in air-driven core-annular flows. *Physical Review E, 86*(6). doi:ARTN 06630510.1103/PhysRevE.86.066305

Camassa, R., Forest, M. G., Lee, L., Ogrosky, H. R., Olander, J. J. P. r. E., Statistical, nonlinear,, & physics, s. m. (2012). Ring waves as a mass transport mechanism in air-driven core-annular flows. *86 6 Pt 2*, 066305.

Chatelin, R., Anne-Archard, D., Murris-Espin, M., Thiriet, M., & Poncet, P. (2017). Numerical and experimental investigation of mucociliary clearance breakdown in cystic fibrosis. *J Biomech, 53*, 56-63. doi:10.1016/j.jbiomech.2016.12.026

Chean, K. Y., Abdulrahman, S., Chan, M.-W., & Tan, K.-C. (2019). A Comparative Study of Respiratory Quality of Life among Firefighters, Traffic Police and Other Occupations in Malaysia. *The international journal of occupational and environmental medicine, 10*(4), 203-215. doi:10.15171/ijoem.2019.1657

CHENG, P. (1964). Two-dimensional radiating gas flow by a moment method. *AIAA Journal, 2*(9), 1662-1664. doi:10.2514/3.2645

Cheng, Y.-S., Zhou, Y., & Chen, B. T. (1999). Particle Deposition in a Cast of Human Oral Airways. *Aerosol Science and Technology, 31*(4), 286-300. doi:10.1080/027868299304165

Chia, K. S., Jeyaratnam, J., Chan, T. B., & Lim, T. K. (1990). Airway responsiveness of firefighters after smoke exposure. *British journal of industrial medicine, 47*(8), 524-527. doi:10.1136/oem.47.8.524

Chitano, P., Hosselet, J. J., Mapp, C. E., & Fabbri, L. M. (1995). Effect of oxidant air pollutants on the respiratory system: Insights from experimental animal reseach. *European Respiratory Journal, 8*(8), 1357-1371. doi:10.1183/09031936.95.08081357

Chow, W. K., Dang, J. F., Gao, Y., & Chow, C. L. (2017). Dependence of flame height of internal fire whirl in a vertical shaft on fuel burning rate in pool fire. *Applied Thermal Engineering, 121*, 712-720. doi:https://doi.org/10.1016/j.applthermaleng.2017.04.108

Clements, J. A., Brown, E. S., & Johnson, R. P. (1958). Pulmonary Surface Tension and the Mucus Lining of the Lungs: Some Theoretical Considerations. *Journal of Applied Physiology, 12*(2), 262-268. doi:10.1152/jappl.1958.12.2.262

Cone, R. A. (2009). Barrier properties of mucus. *Advanced Drug Delivery Reviews, 61*(2), 75-85. doi:https://doi.org/10.1016/j.addr.2008.09.008

Cowley, L. T., & Johnson, A. D. (1992). *Oil and gas fires: Characteristics and impact, offshore technology information* (OTI Report No. 596). Retrieved from Berkshire:

D'Avino, G. (2015). 8 - Numerical Simulations of Viscoelastic Suspension Fluid Dynamics. In F. Chinesta & G. Ausias (Eds.), *Rheology of Non-Spherical Particle Suspensions* (pp. 235-280): Elsevier.

De Flora, S. (2000). Threshold mechanisms and site specificity in chromium(VI) carcinogenesis. *Carcinogenesis, 21*(4), 533-541. doi:10.1093/carcin/21.4.533

DeBar, R. B. (1974). *Fundamentals of the KRAKEN code. [Eulerian hydrodynamics code for compressible nonviscous flow of several fluids in two-dimensional (axially symmetric) region]* (UCID-17366 United States 10.2172/7227630 Dep. NTIS LLNL English). Retrieved from https://www.osti.gov/servlets/purl/7227630

Delichatsios, M. A. (1993). Transition from momentum to buoyancy-controlled turbulent jet diffusion flames and flame height relationships. *Combustion and Flame, 92*(4), 349-364. doi:10.1016/0010-2180(93)90148-V

Demers, P. A., Heyer, N. J., & Rosenstock, L. (1992). Mortality among firefighters from three northwestern United States cities. *British journal of industrial medicine, 49*(9), 664-670. doi:10.1136/oem.49.9.664

Dincer, A. F. I. (2018). *Exergy for A Better Environment and Improved Sustainability 1: Fundamentals*. Switzerland AG: Springer International Publishing.

Droste, B., & Schoen, W. (1988). Full scale fire tests with unprotected and thermal insulated LPG storage tanks. *Journal of Hazardous Materials*.

Drysdale, D. (2011). *An introduction to fire dynamics* (third ed. ed.). NY: John Wiley & Sons.

Dudalski, N., Mohamed, A., Mubareka, S., Bi, R., Zhang, C., & Savory, E. (2020). Experimental investigation of far-field human cough airflows from healthy and influenza-infected subjects. *Indoor Air*. doi:10.1111/ina.12680

Dulfano, M. J., Adler, K., & Philippoff, W. (1971). Sputum Viscoelasticity in Chronic Bronchitis. *American Review of Respiratory Disease*, *104*(1), 88-98. doi:10.1164/arrd.1971.104.1.88

Easterling, G. H., & Prince, S. (2007). Respiratory protection programs for firefighters: a survey of practices for the state of Kentucky. *Public health reports (Washington, D.C. : 1974), 122*(6), 725-732. doi:10.1177/003335490712200604

Eby, S. D., Trépanier, J. Y., & Zhang, X. D. (1998). Modelling radiative transfer in circuit-breaker arcs with the P-1 approximation. *Journal of Physics D: Applied Physics*, *31*(13), 1578-1588. doi:10.1088/0022-3727/31/13/012

Emmanouil, G. V. (2019). Environmental and Occupational Epidemiology Principles. In *Environmental Exposures and Human Health Challenges* (pp. 147-157). Hershey, PA, USA: IGI Global.

EN1473. (2016). Installation and equipment for liquefied natural gas-design of on-shore installations. In.

Faghri, M., & Sundén, B. (2008). *Transport phenomena in fires* (Vol. 20): WIT press.

Fahy, J. V., & Dickey, B. F. (2010). Airway mucus function and dysfunction. *N Engl J Med, 363*(23), 2233-2247. doi:10.1056/NEJMra0910061

Fay, J. A. (2006). Model of large pool fires. *Journal of Hazardous Materials, 136*(2), 219-232. doi:https://doi.org/10.1016/j.jhazmat.2005.11.095

Feng, J., & Xu, B. (2014). Reaction mechanisms for the heterogeneous hydrogenolysis of biomass-derived glycerol to propanediols. *Progress in Reaction Kinetics and Mechanism*, *39*(1), 1-15. doi:10.3184/97809059274714X13874723178485

Feng, Y., Kleinstreuer, C., Castro, N., & Rostami, A. (2016). Computational transport, phase change and deposition analysis of inhaled multicomponent droplet–vapor mixtures in an idealized human upper lung model. *Journal of Aerosol Science*, *96*, 96-123. doi:https://doi.org/10.1016/j.jaerosci.2016.03.001

Feng, Y., Marchal, T., Sperry, T., & Yi, H. (2020). Influence of wind and relative humidity on the social distancing effectiveness to prevent COVID-19 airborne transmission: A numerical study. *Journal of Aerosol Science, 147*, 105585. doi:https://doi.org/10.1016/j.jaerosci.2020.105585

Feng, Y., Zhao, J., Kleinstreuer, C., Wang, Q., Wang, J., Wu, D. H., & Lin, J. (2018). An in silico inter-subject variability study of extra-thoracic morphology effects on inhaled particle transport and deposition. *Journal of Aerosol Science, 123*, 185-207. doi:https://doi.org/10.1016/j.jaerosci.2018.05.010

Fluent Theory Guide. (2019). [2019 R3].

Fu, T. T. (1974). Heat radiation from fires of aviation fuels. *Fire technology*, *10*(1), 54-67. doi:10.1007/BF02590512

Fulford, G. R., & Blake, J. R. (1986). Muco-ciliary transport in the lung. *Journal of theoretical Biology*, *121*(4), 381-402.

Galea, E. (1989). On the Field Modelling Approach to the Simulation of Enclosure Fires. *Journal of Fire Protection Engineering*, *1*(1), 11-22. doi:10.1177/104239158900100103

Gavião, M. B. D., & Bilt, A. V. d. (2004). Salivary secretion and chewing: stimulatory effects from artificial and natural foods %J Journal of Applied Oral Science. *12*, 159-163. Retrieved from http://www.scielo.br/scielo.php?script=sci_arttext&pid=S1678-77572004000200015&nrm=iso

Graczyk, H., Lewinski, N., Zhao, J., Sauvain, J.-J., Suarez, G., Wild, P., . . . Riediker, M. (2016). Increase in oxidative stress levels following welding fume inhalation: a controlled human exposure study. *Particle and Fibre Toxicology, 13*(1), 31. doi:10.1186/s12989-016-0143-7

Groth, M. L., Macri, K., & Foster, W. M. (1997). Cough and Mucociliary Transport of Airway Particulate in Chronic Obstructive Lung Disease. *The Annals of Occupational Hygiene, 41*(inhaled_particles_VIII), 515-521. doi:10.1093/annhyg/41.inhaled_particles_VIII.515

Gueron, S., & Levit-Gurevich, K. (1998). Computation of the internal forces in cilia: application to ciliary motion, the effects of viscosity, and cilia interactions. *Biophysical journal*, *74*(4), 1658-1676.

Gupta, J. K., Lin, C.-H., & Chen, Q. (2011). Transport of expiratory droplets in an aircraft cabin. *Indoor Air, 21*(1), 3-11. doi:10.1111/j.1600-0668.2010.00676.x

Gupta, J. K., Lin, C. H., & Chen, Q. (2009). Flow dynamics and characterization of a cough. *Indoor Air, 19*(6), 517-525. doi:10.1111/j.1600-0668.2009.00619.x

Hägglund, B., & Persson, L. (1976). *The heat radiation from petroleum fires*. Stockholm: Forsvarets Forskningsanstalt.

Haghnegahdar, A., Feng, Y., Chen, X., & Lin, J. (2018). Computational analysis of deposition and translocation of inhaled nicotine and acrolein in the human body with e-cigarette puffing topographies. *Aerosol Science and Technology, 52*(5), 483-493. doi:10.1080/02786826.2018.1447644

Hahn, E. (2019). LPG gas mixture of propane & butane: Which gas is present in LPG. Retrieved from https://www.elgas.com.au/blog/1972-lpg-contains-which-gases-gases-present-in-lpg-gases-used. Retrieved 05.07.19. https://www.elgas.com.au/blog/1972-lpg-contains-which-gases-gases-present-in-lpg-gases-used

Hamed, R., & Fiegel, J. (2014). Synthetic tracheal mucus with native rheological and surface tension properties. *J Biomed Mater Res A, 102*(6), 1788-1798. doi:10.1002/jbm.a.34851

Hannu, T., Piipari, R., Tuppurainen, M., Nordman, H., & Tuomi, T. (2007). Occupational asthma caused by stainless steel welding fumes: a clinical study. *European Respiratory Journal, 29*(1), 85. doi:10.1183/09031936.00058106

Hansen, E. S. (1990). A cohort study on the mortality of firefighters. *British journal of industrial medicine, 47*(12), 805-809. doi:10.1136/oem.47.12.805

Heskestad, G. (1981). Peak gas velocities and flame heights of buoyancy-controlled turbulent diffusion flames. *Symposium (International) on Combustion, 18*(1), 951-960. doi:https://doi.org/10.1016/S0082-0784(81)80099-9

Heskestad, G. (1983). Luminous heights of turbulent diffusion flames. *Fire Safety Journal Fire Safety Journal, 5*(2), 103-108.

Hewitt, J., Smeeth, L., Bulpitt, C. J., Tulloch, A. J., & Fletcher, A. E. (2005). Respiratory symptoms in older people and their association with mortality. *60*(4), 331-334. doi:10.1136/thx.2004.029579 %J Thorax

Hill, D. B., Vasquez, P. A., Mellnik, J., McKinley, S. A., Vose, A., Mu, F., . . . Forest, M. G. (2014). A biophysical basis for mucus solids concentration as a candidate biomarker for airways disease. *Plos One, 9*(2). doi:ARTN e8768110.1371/journal.pone.0087681

Hiroshi, K., & Koseki, H. (2001a). Large scale pool fires: results of recent experiments. *Fire Safety Science Proceedings of 6th International Symposium*, 71-88.

Hiroshi, K., & Koseki, H. (2001b). Large Scale Pool Fires:Results of Recent Experiments. *Fire Safety Science Proceedings of 6th International Symposium*, 71-88.

Hirt, C. W., & Nichols, B. D. (1981). Volume of fluid (VOF) method for the dynamics of free boundaries. *Journal of Computational Physics, 39*(1), 201-225. doi:https://doi.org/10.1016/0021-9991(81)90145-5

Hong, Y. C., Park, H. S., & Ha, E. H. (2000). Influence of genetic susceptibility on the urinary excretion of 8-hydroxydeoxyguanosine of firefighters. *Occupational and environmental medicine, 57*(6), 370-375. doi:10.1136/oem.57.6.370

Hostikka, S., Mcgrattan, K.B. and Hamins, A. (2003). Numerical Modeling Of Pool Fires Using Les And Finite Volume Method For Radiation. *Fire Safety Science Proceedings of 6th International Symposium, 7*, 383-394.

Hottel, H. C. (1959). Review: Certain laws governing the diffusive burning of liquids by Blinov and Khudiakov(1957). *Fire Research Abstracts and Reviews, 1*, 41. Retrieved from https://ci.nii.ac.jp/naid/10007951952/en/

Hu, L., Liu, S., de Ris, J. L., & Wu, L. (2013). A new mathematical quantification of wind-blown flame tilt angle of hydrocarbon pool fires with a new global correlation model. *Fuel, 106*, 730-736. doi:https://doi.org/10.1016/j.fuel.2012.10.075

Hu, Y. Y., Bian, S. Y., Grotberg, J., Filoche, M., White, J., Takayama, S., & Grotberg, J. B. (2015). A microfluidic model to study fluid dynamics of mucus plug rupture in small lung airways. *Biomicrofluidics, 9*(4), 044119-044119. doi:10.1063/1.4928766

Hurley, M. J., Gottuk, D. T., Hall Jr, J. R., Harada, K., Kuligowski, E. D., Puchovsky, M., . . . Wieczorek, C. J. (2016). SFPE Handbook of Fire Protection Engineering.

Ishii, M., & Hibiki, T. (2011). *Thermo-Fluid Dynamics of Two-Phase Flow*: Springer, New York, NY.

Jeanneret-Grosjean, A., King, M., Michoud, M. C., Liote, H., & Amyot, R. (1988). Sampling Technique and Rheology of Human Tracheobronchial Mucus. *American Review of Respiratory Disease, 137*(3), 707-710. doi:10.1164/ajrccm/137.3.707

Johnson, D. W., Martinsen, W. E., Cavin, W. D., Chilton, P. D., Lawson, H. P., & Welker, J. R. (1980). *Control and extinguishment of LPG fires. Final report* (DOE/EV/06020-T3 United States 10.2172/5169763 NTIS, PC A06/MF A01. ORO English). Retrieved from https://www.osti.gov/servlets/purl/5169763

Jones, W. P., & Whitelaw, J. H. (1982). Calculation methods for reacting turbulent flows: A review. *Combustion and Flame, 48*, 1-26. doi:https://doi.org/10.1016/0010-2180(82)90112-2

Joshi, P., Bikkina, P., & Wang, Q. (2016). Consequence analysis of accidental release of supercritical carbon dioxide from high pressure pipelines. *International Journal of Greenhouse Gas Control, 55*, 166-176. doi:https://doi.org/10.1016/j.ijggc.2016.10.010

Kampa, M., & Castanas, E. (2008). Human health effects of air pollution. *Environmental Pollution, 151*(2), 362-367. doi:10.1016/j.envpol.2007.06.012

Karamaoun, C., Sobac, B., Mauroy, B., Van Muylem, A., & Haut, B. (2018). New insights into the mechanisms controlling the bronchial mucus balance. *Plos One, 13*(6), e0199319. doi:10.1371/journal.pone.0199319

Katopodes, N. D. (2019). Chapter 12 - Volume of Fluid Method. In N. D. Katopodes (Ed.), *Free-Surface Flow* (pp. 766-802): Butterworth-Heinemann.

Khajehnajafi, S., Pourdarvish, R., & Cowles, C. (2010). The many faces of fire hazards in industrial settings. *Occup Health Saf, 79*(12), 16, 18-19.

Kim, C. S., Greene, M. A., Sankaran, S., & Sackner, M. A. (1986). Mucus transport in the airways by two-phase gas-liquid flow mechanism: continuous flow model. *J Appl Physiol, 60*(3), 908-917. doi:10.1152/jappl.1986.60.3.908

Kim, C. S., Iglesias, A. J., & Sackner, M. A. (1987). Mucus clearance by two-phase gas-liquid flow mechanism: asymmetric periodic flow model. *J Appl Physiol, 62*(3), 959-971. doi:10.1152/jappl.1987.62.3.959

Kim, C. S., Rodriguez, C. R., Eldridge, M. A., & Sackner, M. A. (1986). Criteria for mucus transport in the airways by two-phase gas-liquid flow mechanism. *J Appl Physiol, 60*(3), 901-907. doi:10.1152/jappl.1986.60.3.901

Kim, Y. H., Tong, Z. B., Chan, H. K., & Yang, R. Y. (2019). CFD modelling of air and particle flows in different airway models. *Journal of Aerosol Science, 134*, 14-28. doi:10.1016/j.jaerosci.2019.04.015

Kim, Y. T., Kim, W. J., Choi, J. E., Bae, M. J., Jang, H., Lee, C. J., . . . Kim, C. (2020). Cohort Profile: Firefighter Research on the Enhancement of Safety and Health (FRESH), a Prospective Cohort Study on Korean Firefighters. *Yonsei medical journal, 61*(1), 103-109. doi:10.3349/ymj.2020.61.1.103

King, M., Brock, G., & Lundell, C. (1985). Clearance of Mucus by Simulated Cough. *Journal of Applied Physiology, 58*(6), 1776-1782. Retrieved from <Go to ISI>://WOS:A1985AKS2800005

Knowles, M. R., & Boucher, R. C. (2002). Mucus clearance as a primary innate defense mechanism for mammalian airways. *Journal of Clinical Investigation, 109*(5), 571-577. doi:10.1172/Jci200215217

Kojima, M. (2011). *The Role of Liquefied Petroleum Gas in Reducing Energy Poverty*. Retrieved from Washington, DC:

Kolanjiyil, A. V., & Kleinstreuer, C. (2017). Computational analysis of aerosol-dynamics in a human whole-lung airway model. *Journal of Aerosol Science, 114*, 301-316. doi:10.1016/j.jaerosci.2017.10.001

Koseki, H. (1989). Combustion properties of large liquid pool fires. *Fire technology, 25*(3), 241-255. doi:10.1007/BF01039781

Koullapis, P. G., Nicolaou, L., & Kassinos, S. C. (2018). In silico assessment of mouth-throat effects on regional deposition in the upper tracheobronchial airways. *Journal of Aerosol Science, 117*, 164-188. doi:10.1016/j.jaerosci.2017.12.001

Labiris, N. R., & Dolovich, M. B. (2003). Pulmonary drug delivery. Part I: physiological factors affecting therapeutic effectiveness of aerosolized medications. *British journal of clinical pharmacology, 56*(6), 588-599. doi:10.1046/j.1365-2125.2003.01892.x

Lai, S. K., Wang, Y. Y., Wirtz, D., & Hanes, J. (2009). Micro- and macrorheology of mucus. *Adv Drug Deliv Rev, 61*(2), 86-100. doi:10.1016/j.addr.2008.09.012

Lambert, A. R., O'Shaughnessy, P. T., Tawhai, M. H., Hoffman, E. A., & Lin, C. L. (2011). Regional deposition of particles in an image-based airway model: Large-eddy simulation and left-right lung ventilation asymmetry. *Aerosol Science and Technology, 45*(1), 11-25. doi:10.1080/02786826.2010.517578

Leal, J., Smyth, H. D. C., & Ghosh, D. (2017). Physicochemical properties of mucus and their impact on transmucosal drug delivery. *International Journal of Pharmaceutics, 532*(1), 555-572. doi:https://doi.org/10.1016/j.ijpharm.2017.09.018

Leiner, G. C., Abramowitz, S., Small, M. J., & Stenby, V. B. (1966). Cough peak flow rate. *Am J Med Sci, 251*(2), 211-214. doi:10.1097/00000441-196602000-00013

Levy, R., Hill, D. B., Forest, M. G., & Grotberg, J. B. (2014). Pulmonary Fluid Flow Challenges for Experimental and Mathematical Modeling. *Integrative and Comparative Biology, 54*(6), 985-1000. doi:10.1093/icb/icu107

Liu, B., Liang, D., & Huang, Y. (2009). Calculation and simulation of thermal radiation of pool fire. *Health and Safety and the Environment, 9*(1), 36-38.

Longest, P. W., Bass, K., Dutta, R., Rani, V., Thomas, M. L., El-Achwah, A., & Hindle, M. (2019). Use of computational fluid dynamics deposition modeling in respiratory drug delivery. *Expert Opinion on Drug Delivery, 16*(1), 7-26. doi:10.1080/17425247.2019.1551875

Ma, B., Ruwet, V., Corieri, P., Theunissen, R., Riethmuller, M., & Darquenne, C. (2009). CFD Simulation and Experimental Validation of Fluid Flow and Particle Transport in a Model of Alveolated Airways. *Journal of Aerosol Science, 40*(5), 403-141. doi:10.1016/j.jaerosci.2009.01.002

Mahajan, R. P., Singh, P., Murty, G. E., & Aitkenhead, A. R. (1994). Relationship between expired lung volume, peak flow rate and peak velocity time during a voluntary cough manoeuvre. *Br J Anaesth, 72*(3), 298-301. doi:10.1093/bja/72.3.298

Mannan, S. (2012). Lees' Loss Prevention in the Process Industries, Volumes 1-3 - Hazard Identification, Assessment and Control (4th Edition). In: Elsevier.

Manolidis, M., Isabey, D., Louis, B., Grotberg, J. B., & Filoche, M. (2016). A Macroscopic Model for Simulating the Mucociliary Clearance in a Bronchial Bifurcation: The Role of Surface Tension. *Journal of Biomechanical Engineering-Transactions of the Asme, 138*(12). doi:Artn 12100510.1115/1.4034507

Mauroy, B., Fausser, C., Pelca, D., Merckx, J., & Flaud, P. (2011). Toward the modeling of mucus draining from the human lung: role of the geometry of the airway tree. *Phys Biol, 8*(5), 056006. doi:10.1088/1478-3975/8/5/056006

May, W. G., & McQueen, W. (1973). Radiation from Large Liquefied Natural Gas Fires. *Combustion Science and Technology, 7*(2), 51-56. doi:10.1080/00102207308952342

McCaffrey, B. (1995). *"Flame height," SFPE handbook of fire protection engineering*. Quincy, Mass.: National Fire Protection Association ; Society of Fire Protection Engineers.

McCaffrey, B. J., & Harkleroad, M. (1989). Combustion efficiency, radiation, co and soot yield from a variety of gaseous, liquid, and solid fueled buoyant diffusion flames. *Symposium (International) on Combustion, 22*(1), 1251-1261. doi:10.1016/S0082-0784(89)80136-5

McGrattan, K. B., Baum, H. R., & Hamins, A. (2000). *Thermal radiation from large pool fires fires (NISTIR 6546)*. Retrieved from MD:

Menter, F. R. (1994). Two-equation eddy-viscosity turbulence models for engineering applications. *AIAA Journal, 32*(8), 1598-1605. doi:10.2514/3.12149

Menter, F. R., Langtry, R., & Völker, S. (2006). Transition Modelling for General Purpose CFD Codes. *Flow, Turbulence and Combustion, 77*(1), 277-303. doi:10.1007/s10494-006-9047-1

Mitran, S. (2013). Continuum-kinetic-microscopic model of lung clearance due to core-annular fluid entrainment. *Journal of Computational Physics, 244*, 193-211. doi:10.1016/j.jcp.2013.01.037

Moorhouse, J. (1982). *Scaling criteria for pool fires derived from large scale experiments*: British Gas Corporation,Solihull, England;.

Mudan, K. S. (1984). *Hydrocarbon pool and vapour fire data analysis* (USDOE Report DE-AC01-83EP16008). Retrieved from

Mudan, K. S. (1984). Thermal radiation hazards from hydrocarbon pool fires. *Progress in Energy and Combustion Science Progress in Energy and Combustion Science, 10*(1), 59-80.

Muñoz, M., Arnaldos, J., Casal, J., & Planas, E. (2004). Analysis of the geometric and radiative characteristics of hydrocarbon pool fires. *Combustion and Flame, 139*(3), 263-277. doi:https://doi.org/10.1016/j.combustflame.2004.09.001

Neitzel, R., Hong, O., Quinlan, P., & Hulea, R. (2013). Pilot task-based assessment of noise levels among firefighters. *International journal of industrial ergonomics, 43*(6), 479-486. doi:10.1016/j.ergon.2012.05.004

NFPA58. (2017). NFPA 58: Liquefied Petroleum Gas Code. In *NFPA 58*. Quincy, MA: National Fire Protection Association.

NFPA59. (2018). NFPA 59: Utility LP-Gas Plant Code. In *NFPA 59*. Quincy, MA: National Fire Protection Association.

NFPA. (2014). NFPA 58: Liquefied Petroleum Gas Code. In. Quincy, Massachusetts: National Fire Protection Association

NFPA. (2016). NFPA 59A: Standard for the production, storage, and handling of liquefied natural gas (LNG). In.

Noh, W. F. W., P.,. (1976). *SLIC (Simple Line Interface Calculation).* Paper presented at the In: Fifth International Conference on Numerical Methods in Fluid Dynamics, Enschede, The Netherlands.

Oka, Y., Sugawa, O., Imamura, T., & Matsubara, Y. (2003). Effect of cross-winds to apparent flame height and tilt angle from several kinds of fire source. *Fire Safety Science, 7*, 915-926.

Palazzi, E., & Fabiano, B. (2012). Analytical modelling of hydrocarbon pool fires: Conservative evaluation of flame temperature and thermal power. *Process Safety and Environmental Protection, 90*(2), 121-128. doi:https://doi.org/10.1016/j.psep.2011.06.009

Paz, C., Suárez, E., & Vence, J. (2017). CFD transient simulation of the cough clearance process using an Eulerian wall film model. *Computer Methods in Biomechanics and Biomedical Engineering, 20*(2), 142-152. doi:10.1080/10255842.2016.1206532

Paz, C., Suarez, E., Vence, J., & Cabarcos, A. (2019). Analysis of the volume of fluid (VOF) method for the simulation of the mucus clearance process with CFD. *Computer Methods in Biomechanics and Biomedical Engineering, 22*(5), 547-566. doi:10.1080/10255842.2019.1569637

Perry, R., Green, D., & Maloney, J. (1984). Perry's chemical engineers' handbook, 6th editionMcGraw-Hill. *New York*.

Picchi, D., Poesio, P., Ullmann, A., & Brauner, N. (2017). Characteristics of stratified flows of Newtonian/non-Newtonian shear-thinning fluids. *International Journal of Multiphase Flow, 97*, 109-133. doi:https://doi.org/10.1016/j.ijmultiphaseflow.2017.06.005

Pires, I., Quintino, L., Amaral, V., & Rosado, T. (2010). Reduction of fume and gas emissions using innovative gas metal arc welding variants. *International Journal of Advanced Manufacturing Technology, 50*(5-8), 557-567. doi:10.1007/s00170-010-2551-4

Pope, S. B. (1985). PDF methods for turbulent reactive flows. *Progress in Energy and Combustion Science, 11*(2), 119-192. doi:https://doi.org/10.1016/0360-1285(85)90002-4

Pourdarvish, R., Khajehnajafi, S., & Cowles, C. (2010). The Many Faces of Fire Hazards in Industrial Settings. *Occupational Health & Safety*.

Pozzetti, G., & Peters, B. (2018). A multiscale DEM-VOF method for the simulation of three-phase flows. *International Journal of Multiphase Flow, 99*, 186-204. doi:https://doi.org/10.1016/j.ijmultiphaseflow.2017.10.008

Puchelle, E., Zahm, J. M., & Duvivier, C. (1983). Spinability of bronchial mucus. Relationship with viscoelasticity and mucous transport properties. *Biorheology, 20*, 239-249. doi:10.3233/BIR-1983-20214

Quintiere, J. G., & Grove, B. S. (1998). A unified analysis for fire plumes. *Symposium (International) on Combustion, 27*(2), 2757-2766. doi:https://doi.org/10.1016/S0082-0784(98)80132-X

Quraishi, M. S., Jones, N. S., & Mason, J. (1998). The rheology of nasal mucus: a review. *Clinical Otolaryngology, 23*(5), 403-413. doi:DOI 10.1046/j.1365-2273.1998.00172.x

Rajendran, R. R., & Banerjee, A. (2019). Mucus transport and distribution by steady expiration in an idealized airway geometry. *Medical Engineering & Physics, 66*, 26-39. doi:10.1016/j.medengphy.2019.02.006

Ramos, F. L., Krahnke, J. S., & Kim, V. (2014). Clinical issues of mucus accumulation in COPD. *International journal of chronic obstructive pulmonary disease, 9*, 139-150. doi:10.2147/COPD.S38938

Rawat, R., Pitsch, H. & Ripoll, J. F. . (2002). *Large-eddy simulation of pool fires with detailed chemistry using an unsteady flamelet model*. Paper presented at the Proceedings of the Summer Program.

Ray, M. S. (1994). Thermal Radiation Heat Transfer, 3rd edn, by R. Siegel and J.R. Howell, Hemisphere Publishing Corporation, USA (1992). 1072 pages. ISBN 0-89116-271-2. *Developments in Chemical Engineering and Mineral Processing, 2*(2 - 3), 190-190. doi:10.1002/apj.5500020220

Ren, S., Li, W., Wang, L., Shi, Y., Cai, M., Hao, L., . . . Luo, Z. (2020). Numerical Analysis of Airway Mucus Clearance Effectiveness Using Assisted Coughing Techniques. *Scientific reports, 10*(1), 2030. doi:10.1038/s41598-020-58922-7

Rengel, B., Mata, C., Pastor, E., Casal, J., & Planas, E. (2018). A priori validation of CFD modelling of hydrocarbon pool fires. *Journal of Loss Prevention in the Process Industries, 56*, 18-31. doi:https://doi.org/10.1016/j.jlp.2018.08.002

Rew, P. J., Hulbert, W. G., & Deaves, D. M. (1996). *Development of pool fire thermal radiation model* (No. 96/1996). Retrieved from United Kingdom:

Richardson, M. (2003). The physiology of mucus and sputum production in the respiratory system. *Nursing Times, 99*(23), 63. Retrieved from https://www.nursingtimes.net/clinical-archive/respiratory-clinical-archive/the-physiology-of-mucus-and-sputum-production-in-the-respiratory-system-10-06-2003/

Rosénstock, L., Demers, P., Heyer, N. J., & Barnhart, S. (1990). Respiratory mortality among firefighters. *British journal of industrial medicine, 47*(7), 462-465. doi:10.1136/oem.47.7.462

Rubin, B. K. (2002). Physiology of airway mucus clearance. *Respiratory care, 47*(7), 761.

Rubin, B. K., Ramirez, O., & Ohar, J. A. (1996). Iodinated Glycerol Has No Effect on Pulmonary Function, Symptom Score, or Sputum Properties in Patients With Stable Chronic Bronchitis. *Chest, 109*(2), 348-352. doi:https://doi.org/10.1378/chest.109.2.348

Rubin, B. K., Ramirez, O., Zayas, J. G., Finegan, B., & King, M. (1990). Collection and Analysis of Respiratory Mucus from Subjects without Lung Disease. *American Review of Respiratory Disease, 141*(4_pt_1), 1040-1043. doi:10.1164/ajrccm/141.4_Pt_1.1040

Salvaggio, J. E. (1994). Inhaled particles and respiratory disease. *Journal of Allergy and Clinical Immunology, 94*(2), 304-309. doi:10.1053/ai.1994.v94.a56009

Samet, J. M., & Cheng, P. W. (1994). The role of airway mucus in pulmonary toxicology. *Environmental Health Perspectives, 102*, 89-103. doi:Doi 10.2307/3431824

Sanchez, D., Hume, L., Chatelin, R., & Poncet, P. (2018). *Analysis of 3D non-linear Stokes problem coupled to transport-diffusion for shear-thinning heterogeneous microscale flows, applications to digital rock physics and mucociliary clearance*. Retrieved from https://hal.archives-ouvertes.fr/hal-01718335

Sanders, N., Rudolph, C., Braeckmans, K., De Smedt, S. C., & Demeester, J. (2009). Extracellular barriers in respiratory gene therapy. *Advanced Drug Delivery Reviews, 61*(2), 115-127. doi:https://doi.org/10.1016/j.addr.2008.09.011

Sengupta, A. (2019). Optimal Safe Layout of Fuel Storage Tanks Exposed to Pool Fire: One Dimensional Deterministic Modelling Approach. *Fire technology, 55*(5), 1771-1799. doi:10.1007/s10694-019-00830-y

Shah, P. L., Scott, S. F., Knight, R. A., Marriott, C., Ranasinha, C., & Hodson, M. E. (1996). In vivo effects of recombinant human DNase I on sputum in patients with cystic fibrosis. *Thorax, 51*(2), 119-125. doi:10.1136/thx.51.2.119

Shusterman, D., Kaplan, J. Z., & Canabarro, C. (1993). Immediate health effects of an urban wildfire. *The Western journal of medicine, 158*(2), 133-138. Retrieved from https://www.ncbi.nlm.nih.gov/pubmed/8434462,https://www.ncbi.nlm.nih.gov/pmc/articles/PMC1021964/

Silberberg, A. (1982). Rheology of mucus, mucociliary interaction, and ciliary activity. *Prog Clin Biol Res, 80*, 25-28. Retrieved from https://www.ncbi.nlm.nih.gov/pubmed/7048323

Sinai, Y. L., & Owens, M. P. (1995). Validation of CFD modelling of unconfined pool fires with cross-wind: Flame geometry. *Fire Safety Journal, 24*(1), 1-34. doi:https://doi.org/10.1016/0379-7112(94)00028-E

Sivathanu, Y. R., & Faeth, G. M. (1990). Generalized state relationships for scalar properties in nonpremixed hydrocarbon/air flames. *Combustion and Flame, 82*(2), 211-230. doi:https://doi.org/10.1016/0010-2180(90)90099-D

Sjögren, B., Hansen, K. S., Kjuus, H., & Persson, P. G. (1994). Exposure to stainless steel welding fumes and lung cancer: a meta-analysis. *Occupational and environmental medicine, 51*(5), 335. doi:10.1136/oem.51.5.335

Smith, D., Gaffney, E., & Blake, J. (2008). Modelling mucociliary clearance. *Respiratory Physiology & Neurobiology, 163*(1-3), 178-188.

Smith, D. J., Gaffney, E. A., & Blake, J. R. (2008). Modelling mucociliary clearance. *Respiratory Physiology & Neurobiology, 163*(1), 178-188. doi:https://doi.org/10.1016/j.resp.2008.03.006

Souil, J. M., Joulain, P., & Gengembre, E. (1984). Experimental and Theoretical Study of Thermal Radiation from Turbulent Diffusion Flames to Vertical Target Surfaces. *Combustion Science and Technology*, *41*(1-2), 69-81. doi:10.1080/00102208408923823

Spagnolie, S. E. (2015). *Complex Fluids in Biological Systems: Experiment, Theory, and Computation*. New York: Springer Science and Business Media.

Steward, F. R. (1970a). Prediction of the Height of Turbulent Diffusion Buoyant Flames. *Combustion Science and Technology*, *2*(4), 203-212. doi:10.1080/00102207008952248

Steward, F. R. (1970b). Prediction of the Height of Turbulent Diffusion Buoyant Flames. *Combustion Science and Technology Combustion Science and Technology*, *2*(4), 203-212.

Sun, B., Guo, K., & Pareek, V. K. (2014). Computational fluid dynamics simulation of LNG pool fire radiation for hazard analysis. *Journal of Loss Prevention in the Process Industries*, *29*, 92-102. doi:https://doi.org/10.1016/j.jlp.2014.02.003

Sun, B., Guo, K., & Pareek, V. K. (2015). Dynamic simulation of hazard analysis of radiations from LNG pool fire. *Journal of Loss Prevention in the Process Industries*, *35*, 200-210. doi:https://doi.org/10.1016/j.jlp.2015.04.010

Tang, F., Li, L. J., Zhu, K. J., Qiu, Z. W., & Tao, C. F. (2015). Experimental study and global correlation on burning rates and flame tilt characteristics of acetone pool fires under cross air flow. *International Journal of Heat and Mass Transfer*, *87*, 369-375. doi:https://doi.org/10.1016/j.ijheatmasstransfer.2015.04.019

Thiriet, M. (2013). *Tissue functioning and remodeling in the circulatory and ventilatory systems*. New York: Springer.

Thomas, P. H. (1963). The size of flames from natural fires. *9th International Combustion Symposium*, 844-859.

Thomas, R. J. (2013). Particle size and pathogenicity in the respiratory tract. *Virulence*, *4*(8), 847-858. doi:10.4161/viru.27172

Tian, G., Hindle, M., Lee, S., & Longest, P. W. (2015). Validating CFD Predictions of Pharmaceutical Aerosol Deposition with in Vivo Data. *Pharmaceutical Research, 32*(10), 3170-3187. doi:10.1007/s11095-015-1695-1

Tran, C. K., ED. (2007). Biologically based lung dosimetry and exposure-dose-response models for poorly soluble inhaled particles. In D. K. B. P. (Ed.), *Particle Toxicology* (pp. 351-386). OH: CRC Press.

Trouvé, A. (2008). *CFD modeling of large-scale pool fires The Second International Energy 2030 Conference*. Abu Dhabi, U.A.E.

Trouvé, A. (2008.). *CFD modeling of large-scale pool fires* Paper presented at the The Second International Energy 2030 Conference., Abu Dhabi, U.A.E.

Tugnoli, A., Salzano, E., Di Benedetto, A., Russo, P., & Cozzani, V. (2013). Analysis of the Flash-Fire Scenario in the Viareggio Accident. *Chemical Engineering Transactions, 32*, 403-408.

Turner, R. D., & Bothamley, G. H. (2014). Cough and the Transmission of Tuberculosis. *The Journal of Infectious Diseases, 211*(9), 1367-1372. doi:10.1093/infdis/jiu625

Utzinger, J. (2004). Health impact assessment: Concepts, theory, techniques, and applications. *Bulletin of the World Health Organization, 82 (*(12), 954-954.

Van den Bosch, C. J. H., & Weterings, R. A. P. M. (1997). *Methods for the calculation of physical effects : Due to releases of hazardous materials (liquids and gases), 'Yellow Book'. CPR 14E*. The Hague: Sdu Uitgevers.

van der Schans, C. P. (2007). Bronchial Mucus Transport. *Respiratory Care, 52*(9), 1150-1158. Retrieved from http://rc.rcjournal.com/content/respcare/52/9/1150.full.pdf

van der Schans, C. P., Postma, D. S., Koeter, G. H., & Rubin, B. K. (1999). Physiotherapy and bronchial mucus transport. *European Respiratory Journal, 13*(6), 1477-1486. doi:DOI 10.1034/j.1399-3003.1999.13f37.x

Vasanth, S., Tauseef, S. M., Abbasi, T., & Abbasi, S. A. (2013). Assessment of four turbulence models in simulation of large-scale pool fires in the presence of wind using computational fluid dynamics (CFD). *Journal of Loss Prevention in the Process Industries, 26*(6), 1071-1084. doi:https://doi.org/10.1016/j.jlp.2013.04.001

Vasanth, S., Tauseef, S. M., Abbasi, T., & Abbasi, S. A. (2015). CFD simulation of pool fires situated at differing elevation. *Process Safety and Environmental Protection, 94*, 89-95. doi:https://doi.org/10.1016/j.psep.2015.01.001

Vasilopoulos, K., Mentzos, M., Sarris, E. I., & Tsoutsanis, P. (2018). Computational Assessment of the Hazardous Release Dispersion from a Diesel Pool Fire in a Complex Building's Area. *Computation, 6*(4). doi:10.3390/computation6040065

Vela, I., Chun, H., Mishra, K. B., Gawlowski, M., Sudhoff, P., Rudolph, M., . . . Schönbucher, A. (2009). Vorhersage der thermischen Strahlung großer Kohlenwasserstoff- und Peroxid-Poolfeuer mit CFD Simulation. *Forschung im Ingenieurwesen, 73*(2), 87-97. doi:10.1007/s10010-009-0094-3

Wallis, G. B. (1969). *One dimensional two-phase flow*. New York: McGraw-Hill.

Wallis, G. B., & Dodson, J. E. (1973). The onset of slugging in horizontal stratified air-water flow. *International Journal of Multiphase Flow, 1*(1), 173-193. doi:https://doi.org/10.1016/0301-9322(73)90010-4

Wang, J., Hoang, T., Floyd, E. L., & Regens, J. L. (2017). Characterization of Particulate Fume and Oxides Emission from Stainless Steel Plasma Cutting. *Annals of work exposures and health, 61*(3), 311-320. doi:10.1093/annweh/wxw031

Wang, W., He, T., Huang, W., Shen, R., & Wang, Q. (2018). Optimization of switch modes of fully enclosed platform screen doors during emergency platform fires in underground metro station. *Tunnelling and Underground Space Technology, 81*, 277-288. doi:https://doi.org/10.1016/j.tust.2018.07.015

Wang, W., He, T. F., Huang, W., Shen, R., & Wang, Q. (2018). Optimization of switch modes of fully enclosed platform screen doors during emergency platform fires in underground metro station. *Tunnelling and Underground Space Technology, 81*, 277-288. doi:10.1016/j.tust.2018.07.015

Wang, Z., Wang, W., & Wang, Q. (2016). Optimization of water mist droplet size by using CFD modeling for fire suppressions. *Journal of Loss Prevention in the Process Industries, 44*, 626-632. doi:10.1016/j.jlp.2016.04.010

Welch Stephen, Carvel Richard, & Torero José. (2007). Large-scale pool fires. *Thermal Science, 11*(2), 101-118.

Welker, J. R., & Sliepcevich, C. M. (1966a). Bending of wind-blown flames from liquid pools. *Fire technology, 2*(2), 127-135.

Welker, J. R., & Sliepcevich, C. M. (1966b). Bending of wind-blown flames from liquid pools. *Fire Technol Fire Technology, 2*(2), 127-135.

Xi, J., Yuan, J. E., Yang, M., Si, X., Zhou, Y., & Cheng, Y. S. (2016). Parametric study on mouth–throat geometrical factors on deposition of orally inhaled aerosols. *Journal of Aerosol Science, 99*, 94-106. doi:10.1016/j.jaerosci.2016.01.014

Xu, X., Shang, Y., Tian, L., Weng, W., & Tu, J. (2018). A numerical study on firefighter nasal airway dosimetry of smoke particles from a realistic composite deck fire. *Journal of Aerosol Science, 123*, 91-104. doi:10.1016/j.jaerosci.2018.06.006

Yang, J., Kim, E. K., Park, H. J., McDowell, A., & Kim, Y.-K. (2020). The impact of bacteria-derived ultrafine dust particles on pulmonary diseases. *Experimental & Molecular Medicine, 52*(3), 338-347. doi:10.1038/s12276-019-0367-3

Yang, J. C., Hamins, A., & Kashiwagi, T. (1994). Estimate of the Effect of Scale on Radiative Heat Loss Fraction and Combustion Efficiency. *Combustion Science and Technology, 96*(1-3), 183-188. doi:10.1080/00102209408935354

Yang, L., Li, X., Yan, Y., & Tu, J. (2017). Effects of cough-jet on airflow and contaminant transport in an airliner cabin section. *The Journal of Computational Multiphase Flows, 10*(2), 72-82. doi:10.1177/1757482X17746920

Yeates, D. B. (1990). *Mucus rheology*. New York: Raven Press, Ltd.

Yi, H., Feng, Y., Park, H., & Wang, Q. (2020). Configuration predictions of large liquefied petroleum gas (LPG) pool fires using CFD method. *Journal of Loss Prevention in the Process Industries, 65*, 104099. doi:https://doi.org/10.1016/j.jlp.2020.104099

Yi, H., Feng, Y., & Wang, Q. (2019). Computational fluid dynamics (CFD) study of heat radiation from large liquefied petroleum gas (LPG) pool fires. *Journal of Loss Prevention in the Process Industries, 61*, 262-274. doi:https://doi.org/10.1016/j.jlp.2019.06.015

Yuan, L., Zhou, L., & Smith, A. C. (2016). Modeling carbon monoxide spread in underground mine fires. *Applied Thermal Engineering, 100*, 1319-1326. doi:10.1016/j.applthermaleng.2016.03.007

Zabetakis, M. G., & Burgess, D. S. (1961). *Research on hazards associated with production and handling of liquid hydrogen. [Fire hazards and formation of shock-sensitive condensed mixtures]* (BM-RI-5707 United States 10.2172/5206437 TIC English). Retrieved from https://www.osti.gov/servlets/purl/5206437

Zanin, M., Baviskar, P., Webster, R., & Webby, R. (2016). The Interaction between Respiratory Pathogens and Mucus. *Cell host & microbe, 19*(2), 159-168. doi:10.1016/j.chom.2016.01.001

Zayas, J. G., Man, G. C. W., & King, M. (1990). Tracheal Mucus Rheology in Patients Undergoing Diagnostic Bronchoscopy: Interrelations with Smoking and Cancer. *American Review of Respiratory Disease, 141*(5_pt_1), 1107-1113. doi:10.1164/ajrccm/141.5_Pt_1.1107

Zhang, Z., Kleinstreuer, C., & Hyun, S. (2012). Size-change and deposition of conventional and composite cigarette smoke particles during inhalation in a subject-specific airway model. *Journal of Aerosol Science, 46*, 34-52. doi:10.1016/j.jaerosci.2011.12.002

Zhao, J., Feng, Y., Bezerra, M., Wang, J., & Sperry, T. (2019). Numerical simulation of welding fume lung dosimetry. *Journal of Aerosol Science, 135*, 113-129. doi:https://doi.org/10.1016/j.jaerosci.2019.05.006

Zheng, Y. (2011). *Liquid plug dynamics in pulmonary airways.* UMI Dissertation Publishing.

Zhongchao Zhao, Y. Z., Yanrui Zhang, Yimeng Zhou, Hao Hu. (2018). Numerical Study on the Transient Thermal Performance of a Two-Phase Closed Thermosyphon. *Energies, 11*(6), 1-15.

Żołek-Tryznowska, Z. (2016). 6 - Rheology of Printing Inks. In J. Izdebska & S. Thomas (Eds.), *Printing on Polymers* (pp. 87-99): William Andrew Publishing.

Zukoski, E. E. (1995). *Combustion Fundamentals of Fire*. London: Academic Press.

APPENDICES

APPENDIX A

Overview of Numerical Models

In this work, a non-premixed combustion model and P-1 radiation model were employed to investigate the characteristics of large LPG pool fires, and VOF model was used to study the mucus clearance efficiency and transport behaviors in the idealized upper airway.

A.1 Non-Premixed Combustion Model

The non-premixed combustion model was employed to simulate an LPG pool fire based on the fact that the fuel (LPG) and oxygen enter the computational domain in distinct streams. The mixture mass fraction f, is introduced in a non-premixed combustion model, which is originated from the fuel stream. It is the local mass fraction LPG stream elements (i.e., C and H). The method is acceptable because the elements in chemical are conserved reactions with the Equilibrium model. Since f is a conserved scalar quantity, its governing transport equations exist no source terms. In the simulation, the LPG pool fire is simplified

to a mixing problem, and the difficulties associated with closing nonlinear mean reaction rates are avoided. The chemical reactions can be modeled as being in chemical equilibrium with the Equilibrium model. Thus, non-premixed modeling involves the solution of transport equations for one or two conserved scalars (the mixture fractions). Specifically, rather than solving the equations for individual species, species concentrations are derived from the predicted mixture fraction fields. Interaction of turbulence and chemistry is accounted for with an assumed-shape Probability Density Function (PDF), and the logical dependence of averaged scalars on mean mixture fraction, the mixture fraction variance, mean enthalpy, and the chemistry model (non-adiabatic, single-mixture-fraction systems) is shown in Figure A. 1.

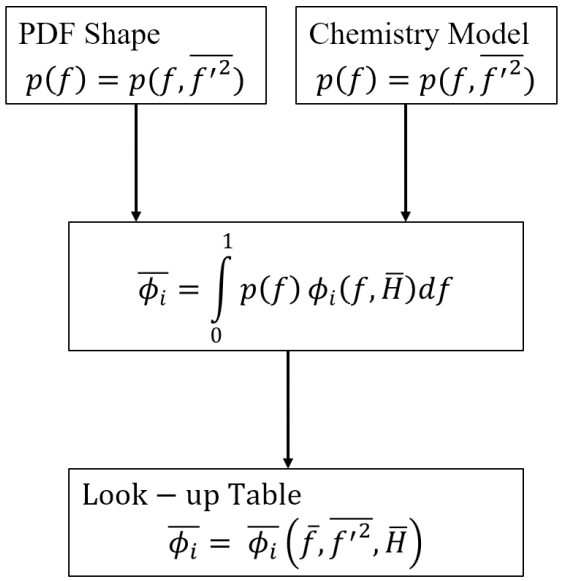

Figure A. 1 Logical dependence of averaged scalars on mean mixture fraction, the mixture fraction variance, mean enthalpy, and the chemistry model.

Mixture Fraction Theory

In the LPG pool fire simulation, the mixture fraction *f* can be expressed in terms of the atomic mass fraction (Sivathanu & Faeth, 1990) by

$$f = \frac{M_i - M_{i,OX}}{M_{i,LPG} - M_{i,OX}} \tag{A.1}$$

where M_i is the elemental mass fraction for element, *i*. $M_{i,OX}$ and $M_{i,LPG}$ are the mass fraction of element *i* in oxidizer and LPG, respectively. It can be found that if the diffusion coefficients for all species are identical in Eq. (A.1), the mixture fraction for all the elements in the combustion system (i.e., C, H, O, and N) are equal. In the non-premixed combustion model, the streams are divided into three streams, i.e., fuel stream, secondary stream, and oxidizer stream. The secondary stream can be another fuel or oxidant, or non-reaction matter. The relationship among the three streams can be expressed by

$$f_{LPG} + f_{sec} + f_{OX} = 1 \tag{A.2}$$

where f_{LPG}, f_{sec}, and f_{OX} are the mass mixture fractions in the combustion system for LPG stream, secondary stream, and air stream, respectively. The relationship among the three streams with mixture fractions is visualized in Figure A. 2, and only the values on the plane ABC are valid in the mixture fraction space.

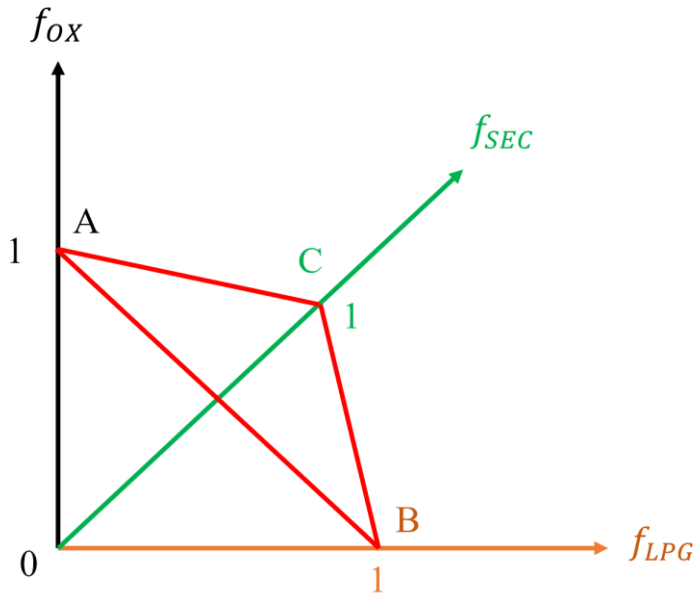

Figure A. 2 Relationship of mixture fractions in the non-premixed combustion system.

Transport Equations for the Mixture Fraction

With the assumption of equal diffusivity coefficient (see Eq. (A.1)), the species equations can be reduced to a single equation for the density-averaged mixture fraction $\overline{f_i}$ is expressed by

$$\frac{\partial}{\partial t}(\rho\overline{f_i}) + \frac{\partial}{\partial x_i}(\rho u_i \overline{f_i}) = \frac{\partial}{\partial x_i}\left(\left(\frac{k}{C_p} + \frac{\mu_t}{\sigma_t}\right)\frac{\partial \overline{f_i}}{\partial x_i}\right) + S_m + S_{user} \tag{A.3}$$

where k is laminar thermal conductivity of the mixture, C_p is the mixture specific heat, σ_t is the Prandtl number, μ_t is the turbulent viscosity. In addition, S_m is the source term due to the transfer of mass into the gas phase from LPG, and S_{user} is a user-defined source term.

In order to solve the density-density average mixture fraction $\overline{f_i}$, another conservation equation for the mixture fraction variance $\overline{f_i'^2}$ (Jones & Whitelaw, 1982) is

$$\frac{\partial}{\partial t}(\rho\overline{f_i'^2}) + \frac{\partial}{\partial x_i}(\rho u_i \overline{f_i'^2}) = \frac{\partial}{\partial x_i}\left(\left(\frac{k}{C_p} + \frac{\mu_t}{\sigma_t}\right)\frac{\partial \overline{f_i'^2}}{\partial x_i}\right) + C_g \mu_t \left(\frac{\partial \overline{f_i}}{\partial x_i}\right)^2 - C_d \rho \frac{\varepsilon}{k}\overline{f_i'^2} + S_{user} \tag{A.4}$$

$$f_i' = f_i - \overline{f_i} \tag{A.5}$$

where C_g and C_d are constants.

Mixture Fraction vs. Equivalence Ratio

Considering the LPG combustion system, the stoichiometric conditions can be represented as:

$$LPG + rO \rightarrow (1 + r)P \tag{A.6}$$

where r is the mass air-to-fuel ratio. In Eq. (A.2), the equivalence ratio ϕ is

$$\phi = \frac{(LPG/air)_{actual}}{(LPG/air)_{stochiometric}} \tag{A.7}$$

Relationship of Mixture Fraction to Species Mass Fraction, Density, and Temperature

Under the assumption of chemical equilibrium, all thermochemical scalars (species fractions, density, and temperature) are uniquely related to the mixture fractions in the non-adiabatic systems can be expressed by

$$\phi_i = \phi_i(f_i, H) \tag{A.8}$$

$$H = \sum_j Y_j H_j \tag{A.9}$$

$$H_j = \int_{T_{ref},j}^{T} C_{p,j}\, dT + h_j^0(T_{ref}, j) \tag{A.10}$$

where H is the total enthalpy, Y_j is the mass fraction of species *j*, H_j is the enthalpy for species *j*. In addition, $C_{p,j}$ and $h_j^0(T_{ref}, j)$ represent the heat capacity and formation enthalpy at T_{ref} for species *j*, respectively.

Turbulence-Chemistry Interaction Model

The instantaneous relationships between mixture fraction and species fractions, density, and temperature under the assumption of chemical equilibrium are concerned with the prediction of the averaged values of these fluctuating scalars, which depends on the turbulence-chemistry interaction model. In this study, probability density function (PDF), $p(f)$ (see Figure C. 3) (*Fluent Theory Guide*, 2019) approach was applied to calculate the values in the non-premixed combustion model and can be expressed by

$$p(f) = \frac{1}{\Delta f} lim_{T\to\infty} \frac{1}{T} \sum_i \tau_i \tag{A.11}$$

where T is time and τ_i is the amount of time that f spends in the Δf band.

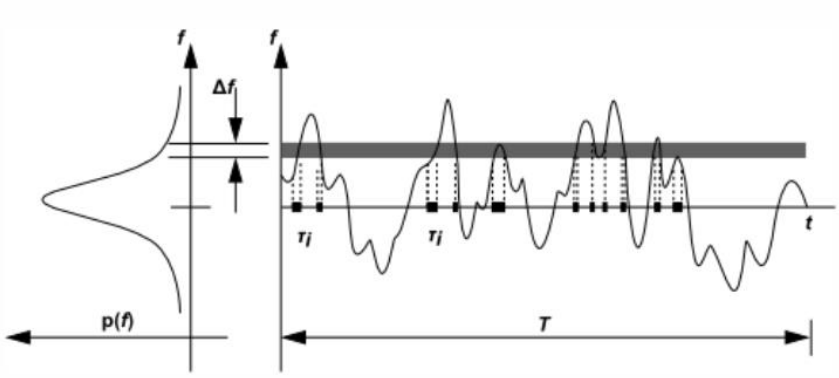

Figure A. 3 Graphical scheme of probability density function (*Fluent Theory Guide*, 2019)

Thus, integrating Eq. (A.11), the density-weighted mean species mass fractions and temperature (Eq. (A.8)) for a single mixture system can be computed by

$$\bar{\phi}_i = \int_0^1 p(f)\, \phi_i(f, \bar{H}) df \tag{A.12}$$

Similarly, the mean time-averaged fluid density $\bar{\rho}$ can be computed as:

$$\bar{\rho} = \frac{1}{\int_0^1 \frac{p(f)}{\rho(f)} df} \tag{A.13}$$

A.2 P-1 Radiative model

As one of the widely accepted methods based on the expansion of the radiation intensity into an orthogonal series of spherical harmonics, P-1 radiation model (P. CHENG, 1964; Ray, 1994) was selected to predict the heat flux intensity from large LPG pool fires to surrounding objectives, and the equation can be expressed by

$$\Gamma = \frac{1}{3(a + \sigma_s) - C\sigma_s} \tag{A.14}$$

$$q_r = \Gamma \nabla G \tag{A.15}$$

where a is the absorption coefficient, σ_s is the scattering coefficient, G is the incident radiation, and C is the linear-anisotropic phase function coefficient. In Eq. (A.15), G can be obtained the energy equation (Eq. (A.16)):

$$\nabla \cdot (\Gamma \nabla G) - aG + 4an^2 \sigma_{S-B} T^4 = S_G \tag{A.16}$$

where n is the refractive index of the medium, σ_{S-B} is the Stefan-Boltzmann constant, and S_G is a user-defined radiation source.

A.3 VOF Model

In this work, the Volume of Fluid (VOF) method was employed to investigate the mucus clearance and transport behaviors in an idealized upper airway. The VOF method was devised by Hirt and Nichols (Hirt & Nichols, 1981) to overcome the low-resolution issues on the interface of multiphases with coarse computational grids by the KRAKEN method (DeBar, 1974) and Simple Line Interface Calculation method (Noh, 1976). Specifically, the VOF method is often employed to investigate the transport behaviors of two or more immiscible fluids by solving a single set of momentum equations and track the volume fraction of each of the fluids throughout the computational domain (Katopodes, 2019), which can be employed for the steady or transient tracking of liquid-gas interface.

In the VOF model, air and mucus are considered as the primary phase and the secondary phase, respectively. In this work, the phases of air and mucus are assumed as non-interpenetrating, and the volume fraction of the mucus phase in the computational cell is introduced when it has been added into the computational model. In each control volume, the total of the volume fractions for both phases are equal to 1.0. Specifically, the mucus volume fraction α_m can be defined as:

$$\alpha_m = \frac{V_m}{V} \tag{A.17}$$

(A.18a)

$$\alpha_m = \begin{cases} 0 \\ (0,1) \\ 1 \end{cases} \tag{A.18b}$$

(A.18c)

where V_m is the mucus volume in a certain mesh cell, and V is the mesh cell volume. Accordingly, the air-mucus mixture properties can be determined by:

$$\rho = \alpha_m \rho_m + \alpha_a \rho_a \tag{A.19}$$

$$\mu = \alpha_m \rho \mu_m + \alpha_a \mu_a \tag{A.20}$$

where ρ and μ are the mixture density and viscosity in the control volume, and α_a is the air volume fraction. In addition, μ_a is the air viscosity, and μ_m is mucus viscosity.

Continuity Equation

Mucus and air are considered as Newtonian and incompressible (Thiriet, 2013). Air-mucus interface tracking can be achieved by solving the continuity equation (Ishii & Hibiki, 2011). For mucus and air, the continuity equation is given by

$$\rho_m \left(\frac{\partial}{\partial t} \alpha_m + \nabla \cdot (\alpha_m \vec{v}_m) \right) = \dot{m}_{am} - \dot{m}_{ma} \tag{A.21}$$

where $\vec{v}_m$ is mucus velocity vector, and $\vec{v}_a$ is air velocity vector. Additionally, $\dot{m}_{am}$ is the mass transfer from the air phase to the mucus phase, and $\dot{m}_{ma}$ is the mass transfer from the mucus phase to the air phase. The air volume fraction is obtained based on the following constraint:

$$\alpha_a = 1 - \alpha_m \tag{A.22}$$

Momentum Balance Equation

Only a single momentum equation needs to be solved throughout the computational domain, and the velocity is shared at the mucus-air interface (Ishii & Hibiki, 2011). Nevertheless, the equation is dependent on both mucus and air volume fractions, which determine the mixture density and viscosity (see Eqs. (A.19) & (A.20)). Specifically, the momentum equation is given by

$$\frac{\partial}{\partial t}(\rho\vec{v}) + \nabla\cdot(\rho\vec{v}\vec{v}) = -\nabla p + \nabla\cdot\left(\mu(\nabla\vec{v} + \nabla\vec{v}^{T})\right) + \rho\vec{g} + \vec{F}_{CSS} \tag{A.23}$$

where $\vec{v}$ is velocity vector, $\vec{g}$ is the gravity vector, p is pressure, $\vec{F}_{CSS}$ is the surface tension force between air and mucus. It should be mentioned that the large error might be produced at the interface when large velocity differences exist between air and mucus phases (Katopodes, 2019).

Energy Balance Equation

The energy equation for the VOF model has the following form (Zhongchao Zhao, 2018):

$$\frac{\partial}{\partial t}(\rho E) + \nabla\cdot\left(\vec{v}(\rho E + p)\right) = \nabla\cdot(k\nabla T) \tag{A.24}$$

$$k = \alpha_m k_m + \alpha_a k_a \tag{A.25}$$

where E is energy, and k is the thermal conductivity. In addition, k_m is the mucus thermal conductivity and k_a is the air thermal conductivity. Energy and temperature are treated as mass-averaged variables showing in the following:

$$\frac{\partial}{\partial t}(\rho E) + \nabla\cdot\left(\vec{v}(\rho E + p)\right) = \nabla\cdot(k\nabla T) \tag{A.26}$$

$$k = \alpha_m k_m + \alpha_a k_a \tag{A.27}$$

where E is energy, and k is the thermal conductivity. In addition, k_m is the mucus thermal conductivity and k_a is the air thermal conductivity. Energy and temperature are treated as mass-averaged variables showing in the following:

$$E = \frac{\alpha_m \rho_m E_m + \alpha_a \rho_a E_a}{\alpha_m \rho_m + \alpha_a \rho_a} \tag{A.28}$$

$$E_m = C_{p,m}\left(T - T_{sat,m}\right) \tag{A.29}$$

$$E_a = C_{p,a}\left(T - T_{sat,a}\right) \tag{A.30}$$

where E_m and E_a the energies from mucus and air, respectively. $C_{p,m}$ is the mucus specific heat capacity, and $C_{p,a}$ is the air specific heat capacity. $T_{sat,m}$ is the mucus saturation temperature, and $T_{sat,a}$ is the air saturation temperature.

APPENDIX B

Mesh Independence Test for the 3D Straight Tube

To validate the developed VOF model employed in this study, a 3D straight tube (200 mm in length × 10 mm in diameter) with mucus thickness 1.5 mm has been reconstructed (see Figure B. 1). The geometric dimensions were selected to duplicate the same setup used in benchmark experiments (C. S. Kim, Greene, et al., 1986; C. S. Kim et al., 1987; C. S. Kim, Rodriguez, et al., 1986). Using ANSYS Fluent Meshing (ANSYS Inc., Canonsburg, PA), the poly-hexcore mesh is generated and consisted of unstructured polyhedral and hexahedral elements with 5 prism layers generated at the air-mucus interface and wall. Employing ANSYS Fluent 2020 R1 (ANSYS Inc., Canonsburg, PA), the mesh independence test has been performed to determine the final mesh with the optimized balance between computational accuracy and efficiency by steady-state simulations. As shown in Figure B. 1, the mucus properties and boundary conditions were assigned, i.e., the mucus feeding rate $q_m = 1\ ml/min$, the mucus viscosity $\mu_m = 7.9\ Pa \cdot s$, and the air flow rate $q_a = 19.5\ ml/min$, which are consistent with the experimental setup (C. S. Kim, Greene, et al., 1986; C. S. Kim et al., 1987; C. S. Kim, Rodriguez, et al., 1986). The mesh specifications and simulation results are shown in Table B. 1 and Figure B. 2, respectively. Specifically, the mucus volume fraction α_m in the computational domain obtained by the simulations were compared with the average mucus volume fraction in experimental tests. The relative errors between simulations and experiments are 37.1%, 2.5%, 1.8 %, and 0.6% when using Mesh 1, Mesh 2,

Mesh 3, and Mesh 4, respectively. As shown in Table B. 1, the final mesh (Mesh3) contains 500,488 elements, with the volumetric maximum skewness equal to 0.52. Specifically, 2 peel layers, 4 buffer layers, and 5 prism layers are generated to guarantee the smooth transition and the thickness of the first prism layer for satisfying y+ < 1 to capture the laminar-to-turbulence transition using the Transition Shear Stress Transport (SST) Model (Menter, 1994; Menter, Langtry, & Völker, 2006).

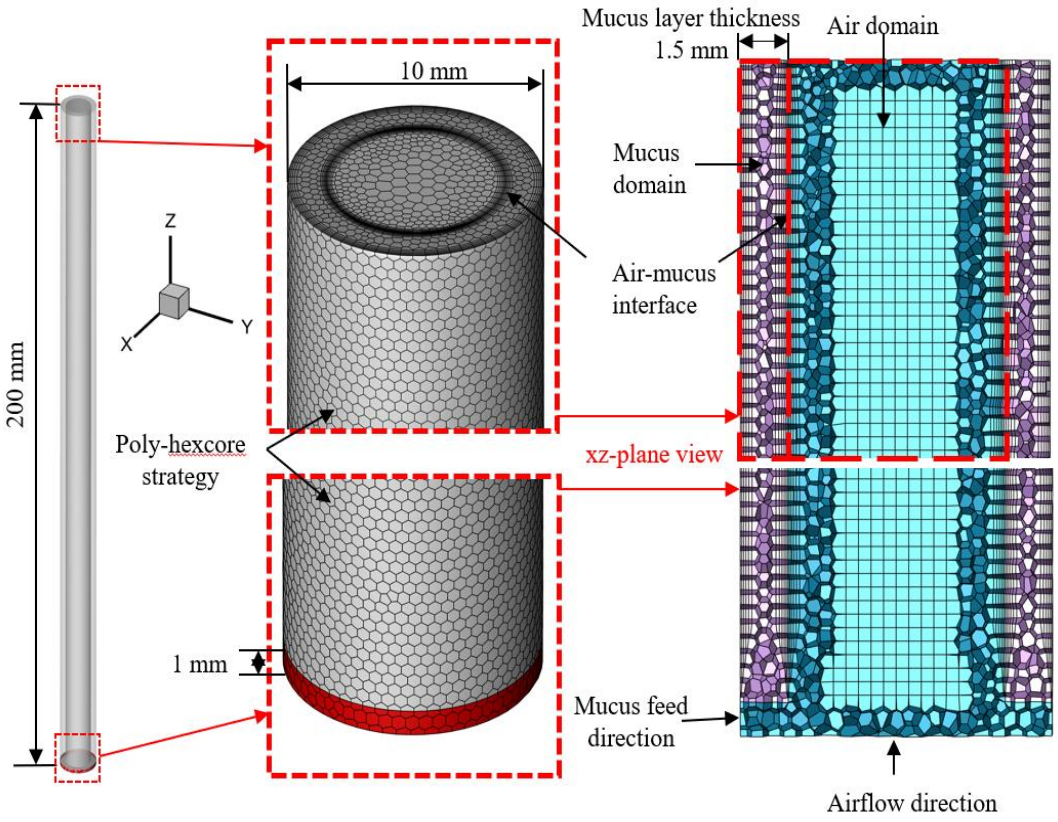

Figure B. 1 Schematic of the computational domain with the poly-hexcore mesh details in the straight tube.

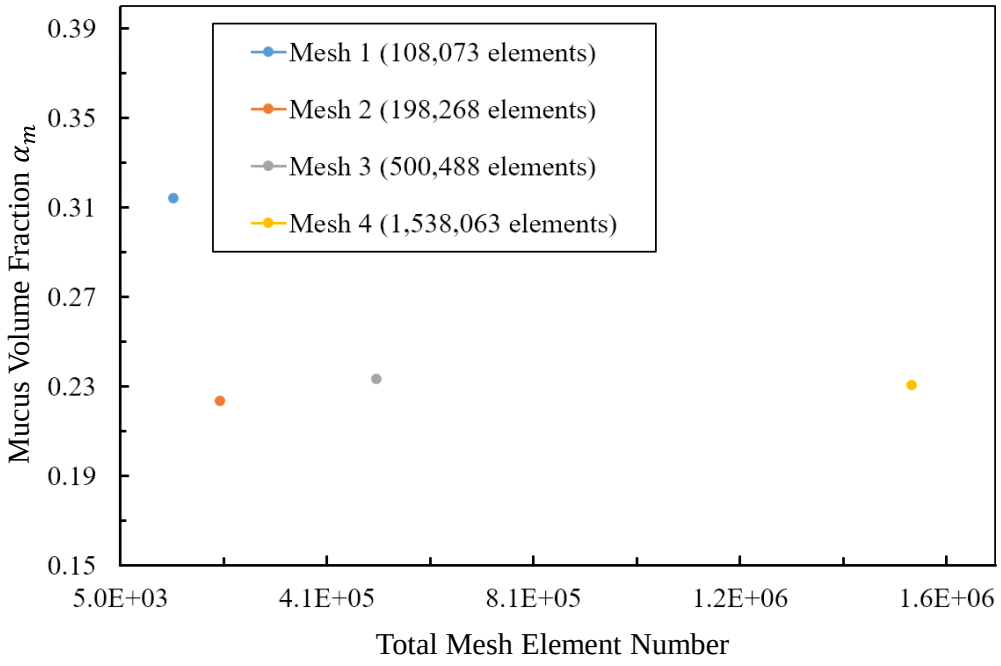

Figure B. 2 Mesh independence test in the straight tube.

Table B. 1 Details of the meshes generated for the mesh independence test of the straight tube.

Mesh	Number of Prism Layers	Minimum Element Size (mm)	Maximum Skewness	Total Element Number
Mesh 1	5	0.05	0.61	108,073
Mesh 2		0.05	0.57	198,268
Mesh 3		0.03	0.52	500,488
Mesh 4		0.027	0.54	1,538,063

APPENDIX C

In-house UDFs for Cough Waveforms

C.1 Cough Intensity I (CS-I)

```
/************************************************************************/
/*                          Copyright (C) 2020, CBBL                    */
/*                    School of Chemical Engineering                    */
/*                  Oklahoma State University, Stillwater, OK, USA      */
/************************************************************************/

#include "udf.h"

DEFINE_PROFILE(unsteady_inlet_velocity, thread, position)
{
  real x[ND_ND];            /* this will hold the position vector */
  real r, q1,um;
  face_t f;
  real t=CURRENT_TIME;
  real radius=0.008;   /* Radius in m*/
  real xc=0.0;   /*coordinates of inlet circle center */
  real yc=0.0;

  if (t <= 0.5126)
  {
        q1 = -2.487-
1.506*cos(6.923*t)+6.944*sin(6.923*t)+2.51*cos(2*6.923*t)+3.536*sin(2*6.923*t)+1.2
79*cos(3*6.923*t)+0.002213*sin(3*6.923*t); /*flow rate L/s*/
          }
  else
  {
        q1 = 0;
  }

  um=q1/(3.14159265*radius*radius)/1000.;
```

```
begin_f_loop(f, thread)
    {
      F_PROFILE(f, thread, position) = um;
    }
  end_f_loop(f, thread)
}
```

C.2 Cough Intensity II (CS-II)

```
/************************************************************************/
/*                          Copyright (C) 2020, CBBL                    */
/*                     School of Chemical Engineering                   */
/*                   Oklahoma State University, Stillwater, OK, USA     */
/************************************************************************/

#include "udf.h"

DEFINE_PROFILE(unsteady_inlet_velocity2, thread, position)
{
  real x[ND_ND];            /* this will hold the position vector */
  real r, q1,um;
  face_t f;
  real t=CURRENT_TIME;
  real radius=0.008;   /* Radius in m*/
  real xc=0.0;   /*coordinates of inlet circle center */
  real yc=0.0;

  if (t <= 0.5126)
  {
         q1 = -4.974-
3.012*cos(6.923*t)+13.888*sin(6.923*t)+5.02*cos(2*6.923*t)+7.072*sin(2*6.923*t)+2.
558*cos(3*6.923*t)+0.004426*sin(3*6.923*t); /*flow rate L/s*/
           }
  else
  {
         q1 = 0;
  }

  um=q1/(3.14159265*radius*radius)/1000.;

  begin_f_loop(f, thread)
    {
      F_PROFILE(f, thread, position) = um;
    }
  end_f_loop(f, thread)
```

VITA

Hang Yi

Candidate for the Degree of

Doctor of Philosophy

Dissertation: CHARACTERIZATION OF LARGE LPG POOL FIRES AND MUCUS CLEARANCE DYNAMICS IN UPPER AIRWAY USING CFD METHOD

Major Field: Chemical Engineering

Biographical:

Education:

Completed the requirements for the Doctor of Philosophy in Chemical Engineering at Oklahoma State University, Stillwater, Oklahoma in December, 2020.

Completed the requirements for the Master of Science in Safety Science and Engineering at Northeastern University, Shenyang, China in July, 2015.

Completed the requirements for the Bachelor of Engineering in Safety Engineering at Northeastern University, Shenyang, China in June, 2013.

Experience:

Graduate Research Assistant, School of Chemical Enginnering, Oklahoma State University 2019-2020
Gradaute Research Assistant, Department of Fire Protection and Safety Engineering, Oklahoma State University 2016-2018
Graduate Teaching Assistant, Department of Fire Protection and Safety Engineering, Oklahoma State University 2016-2018

Professional Memberships:

International Association for Fire Safety Science